# **NOTE TO USERS**

This reproduction is the best copy available.



# DESIGN AND DEVELOPMENT OF AN IMPACT WEAR TESTING DEVICE FOR THE MINERALS INDUSTRY

Lokesh K. Thakur

Department of Mechanical Engineering
McGill University, Montréal

February 2004

A Thesis submitted to the Faculty of Graduate Studies and Research in partial fulfilment of the requirements for the degree of Master of Engineering

© Lokesh K. Thakur, 2004



Library and Archives Canada

Published Heritage Branch

395 Wellington Street Ottawa ON K1A 0N4 Canada Bibliothèque et Archives Canada

Direction du Patrimoine de l'édition

395, rue Wellington Ottawa ON K1A 0N4 Canada

> Your file Votre référence ISBN: 0-612-98569-5 Our file Notre référence ISBN: 0-612-98569-5

#### NOTICE:

The author has granted a non-exclusive license allowing Library and Archives Canada to reproduce, publish, archive, preserve, conserve, communicate to the public by telecommunication or on the Internet, loan, distribute and sell theses worldwide, for commercial or non-commercial purposes, in microform, paper, electronic and/or any other formats.

#### AVIS:

L'auteur a accordé une licence non exclusive permettant à la Bibliothèque et Archives Canada de reproduire, publier, archiver, sauvegarder, conserver, transmettre au public par télécommunication ou par l'Internet, prêter, distribuer et vendre des thèses partout dans le monde, à des fins commerciales ou autres, sur support microforme, papier, électronique et/ou autres formats.

The author retains copyright ownership and moral rights in this thesis. Neither the thesis nor substantial extracts from it may be printed or otherwise reproduced without the author's permission.

L'auteur conserve la propriété du droit d'auteur et des droits moraux qui protège cette thèse. Ni la thèse ni des extraits substantiels de celle-ci ne doivent être imprimés ou autrement reproduits sans son autorisation.

In compliance with the Canadian Privacy Act some supporting forms may have been removed from this thesis.

While these forms may be included in the document page count, their removal does not represent any loss of content from the thesis.

Conformément à la loi canadienne sur la protection de la vie privée, quelques formulaires secondaires ont été enlevés de cette thèse.

Bien que ces formulaires aient inclus dans la pagination, il n'y aura aucun contenu manquant.



#### ABSTRACT

World wide steel consumption as grinding media is estimated at over 600,000 tons per annum. Total steel media wear in a given mill (ball or SAG) grinding process is a product of three recognized wear mechanisms–impact, abrasion, and corrosion of which the contribution of each wear mechanism to total media wear has not been well established.

A total media wear model can be defined on the assumption that the effect of each wear mechanism can be independently determined and this effect can be tied to mill charge motion as determined or estimated using a charge motion simulator, which allows for a total media wear model to be defined as the summation of the wear results of each mechanism. This necessitates the need for developing impact, abrasion and corrosion wear testers that will allow the study of media wear over a wide range of energy levels. Refinement of the impact test will allow studying how impact media wear at high energies behaves as a function of those energies.

This thesis research project work is focused on design and development of a highenergy impact wear tester. A comprehensive illustration on designing the newest version of the impact wear tester is explained in detail in order to exhibit how theoretical, virtual and experimental analyses could be integrated while designing a mechanical system.

# RÉSUMÉ

La consommation mondial d'acier en forme de corps broyant est estimée à au dessus de 600,000 tons par annum. L'usure totale d'acier dans un moulin donné (aux boulets ou semi-autogène) est un produit de trois mécanismes d'usure reconnus-l'impact, l'abrasion, et la corrosion dont la contribution de chaque mécanisme d'usure au total usé pour totaliser l'usure de presse n'a pas été bien établie.

Un modèle total d'usure des corps broyant peut être défini en supposant que l'effet de chaque mécanisme d'usure est indépendante et peut être déterminé et lié au mouvement de la charge d'un broyeur déterminé ou estimé par un simulateur de mouvement de charge. La contribution de chaque mécanisme ainsi déterminé peut par la suite être additionnée ensemble pour en estimée l'usure totale. Cela nécessite le développement de dispositif expérimental pour déterminer l'usure d'impact, d'abrasion et de corrosion qui permettra l'étude d'usure des corps broyant en fonction de l'énergie. L'amélioration du dispositif d'usure d'impact permettra d'étudier comment l'usure des corps broyant par impact se comporte en fonction de l'énergie d'impact.

Ce travail de projet de recherche de thèse est concentré sur la conception et le développement d'un test d'usure d'impact d'haut énergie. Une illustration complète du procédé de conception de la dernière version du test d'usure d'impact est expliquée en détail afin d'exposer comment l'analyse théorique, virtuelle et expérimental pourrait être intégré dans la conception de ce système mécanique.

#### **ACKNOWLEDGEMENTS**

I am indebted to Professor Peter Radziszewski for his continued supervision, guidance, and invaluable support throughout the course of my thesis research. His patience and encouragement made this thesis research possible.

Financial support of the Natural Science and Engineering Research Council of Canada-CRD project with the steel media wear component of the AMIRA-JKMRC P9M project is duly acknowledged.

I would like to express my gratitude to Mr. Tony Micozzi and Mr. Nick De Palma from the machine tool lab, Mr. Georges Tewfik and Mr. Mario Iacobaccio from the instrumentation lab, and Mr. Raymond Lemay, Mr. Garry Savard and Mr. John Boisvert from the undergraduate workshop for helping me time to time for my thesis project work.

Special thanks are due to Mr. Peter Chau for helping me with my computer problems and to Mr. Waseem Khan for helping me with IATEX.

I am also thankful to my friends Li Jie, Himanshu Sikka, Amy Cox, Neil Fleming, Jose Candanedo, Nima Atabaki, Ryan Tomicic, Dave Scott and Vijay Rana for standing beside me during my thesis research progression.

I would like to express my deepest gratitude to Mr. Rajendra B. Panwar, who has been inspiration to my entire life since he became my brother-in-law.

Finally, I am thankful to my family for their never-ending encouragement and support.

# TABLE OF CONTENTS

ABSTRACT	i
RÉSUMÉ	ii
ACKNOWLEDGEMENTS	iii
SYMBOLS AND ABBREVIATIONS	vii
CHAPTER 1. Introduction	1
1.1. Research in Steel Media Wear Prediction	4
1.2. Exploring Impact Media Wear: Semi-empirical Approach	7
1.3. Project Objectives	9
1.3.1. Design and Development	10
1.4. Organization of the Thesis	10
CHAPTER 2. Impact Wear Tester Developments	12
2.1. Version I of the Impact Wear Tester	12
2.1.1. Verification by Industrial Mill Data	14
2.1.2. Discussions	16
2.2. Version II of the Impact Wear Tester	17
2.2.1. Description with some Design Improvements	17
2.2.2. Initial Test Results	21
2.2.3. Discussions	25
CHAPTER 3. Theoretical and Virtual Dynamics of the Impactor Mechanism	26
3.1. Description of the Impactor Mechanism	26

#### TABLE OF CONTENTS

3.2. Th	eoretical Dynamics of the System	29
3.2.1.	Derivation for Calculating Dynamic Parameters	29
3.3. Vir	tual Dynamics of the System	34
3.3.1.	Benefits of Functional Virtual Prototyping	34
3.3.2.	Impact Tester Virtual Modelling	35
3.3.3.	Simulation Results	38
3.3.4.	Discussions	42
CHAPTER	4. Lever Arm Assembly Design Stages	43
4.1. Des	sign of the Lever Arm Assembly	43
4.1.1.	Design Stages	44
4.2. Fir	st Design Stage: Evolutionary Design Ideas	44
4.3. Sec	cond Design Stage: Material Selection and Design Stress	46
4.3.1.	Material Selection	47
4.3.2.	Design Stress	48
CHAPTER	5. Third Design Stage: Theoretical Analysis of the Lever Arm .	55
5.1. Pla	astic Design	55
5.2. An	alysis of Beams	57
5.2.1.	Theory of Flexure	58
5.2.2.	Internal Moment beyond the Elastic Limit	60
5.2.3.	Deflection of Beams	61
5.2.4.	Relation between Deflection and Stress	63
5.2.5.	Resilience of Beams	65
CHAPTER	6. Design of the Lever Arm Assembly Components by FEA	66
6.1. Fin	tite Element Analysis	66
6.1.1.	Structural Analysis	66
6.2. For	urth Design Stage: Lever Arm Design	67
6.2.1.	A Model of the Problem	67
622	Design Ontimization: Lever Arm	69

#### TABLE OF CONTENTS

6.2.3. Final I Cross Section	73
6.2.4. Validation of Simulation Results with the Theoretical Analysis	74
6.3. Fifth Design Stage: Coupling Assembly Design	76
6.3.1. Design of the Front Part	76
6.3.2. Design of the Side Brackets	80
6.4. Final Design Stage: Follower Assembly Design	82
6.4.1. Determination of the Dimensions by Space Planning	82
CHAPTER 7. Development and Setup of Version III of the Impact Wear Tester	
Prototype	87
7.1. Development of the Impact Tester Prototype	87
7.2. Setup of the Impact Tester Prototype	89
7.3. Speed at Impact by Theoretical Analysis	91
CHAPTER 8. Conclusions and Recommendations for Future Work	93
8.1. Conclusions	93
8.2. Recommendations for Future Work	95
BIBLIOGRAPHY	96
APPENDIX A. Engineering Drawings of the Lever Arm Assembly and its	
Components	102
A 1 Drawings of the Lever Arm Assembly and Components	102

#### SYMBOLS AND ABBREVIATIONS

# Latin Symbols

- A: Area.
- c: Distance from neutral axis to outer fiber associated with beam analysis.
- d: Unit, angular.
- D: Spring displacement.
- e: Gross longitudinal.
- E: Energy.
- $E_y$ : Young's modulus.
- f: Deflection.
- F: Force.
- i: Slope.
- I: Rectangular moment of inertia.
- $I_p$  or J: Polar moment of inertia.
- l: Length.
- L: Distance between beam supports.
- m: Mass lost associated with the wear mechanisms.
- $M_b$ : Bending moment.
- $M_o$ : Moment about fulcrum.
- $M_t$ : Torsion.
- N: Factor of safety.
- P: Concentrated load.
- $P_a$ : Pressure.
- $P_c$ : Probabilistic constant.
- r: Radius.
- s: Unit, longitudinal.
- s': Unit, lateral.
- S: Unit normal apparent stress.
- $S_s$  or  $S_v$ : Transverse shearing unit stress.

- t: Time.
- T: Torque.
- v: Velocity.
- V: Shear stress.
- w: Distributed load per longitudinal unit.
- W: Total distributed load.
- W': Weight of the body.
- x: Displacement.
- Z: Horizontal shearing stress.

# Greek Symbols

- $\alpha$ : Unit, angular.
- $\gamma_S$ : Coefficient of variation.
- $\theta$ : Angle.
- $\kappa$ : Spring constant.
- $\mu$ : Coefficient of friction.
- $\mu_p$ : Poisson's ratio.
- $\rho$ : Metal density.
- $\phi$ : Angular displacement.

# Introduction

In mineral processing industries, grinding processes can be defined as pulverization or comminution of big particles in order to reduce them to minute particles. Depending upon the mining operation, half of the overall operating cost of comminution processes can be found in the cost of steel media wear.

Metal wear is primarily associated with these processes, which in Canada and the United States represents an annual consumption of some 300,000 tons of iron and steel (Nass, 1974). Grinding performance and quality can also be affected by wear, which consists of three recognized wear mechanisms—abrasion, corrosion and impact.

In such a context, predictive wear models have become a necessity to determine most optimum grinding conditions that can reduce process wear while maintaining grinding performance and quality (Radziszewski, 1997b). These impact and abrasion energy spectra provide an opportunity to study media wear as a function of the operating parameters of a given mill (Radziszewski and Tarasiewicz, 1993a,b).

A tumbling mill, whether it is autogenous, semi-autogenous, ball or rod, is a system comprises of a number of interrelated and interactive elements that work together in order to grind a given ore. This comminution process is achieved by individual balls that compose actual ball mill elements, which bring about ore breakage (Radziszewski, 2001). Jointly, these balls form the mill ball charge which, during ball mill operation, typically has a charge profile as can be found in the figures 1.1.

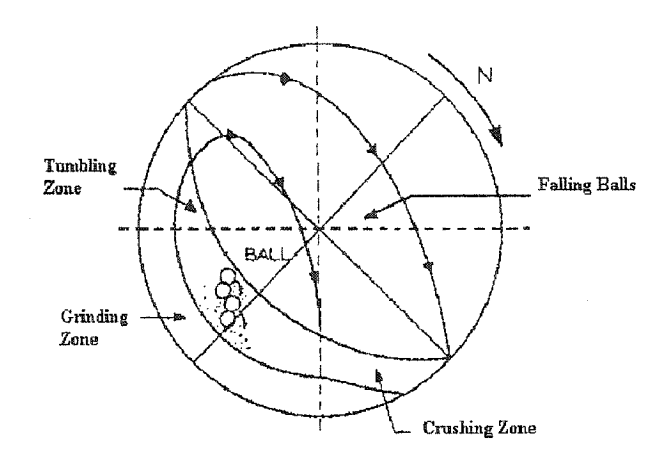


Figure 1.1: Typical ball charge motion profile.

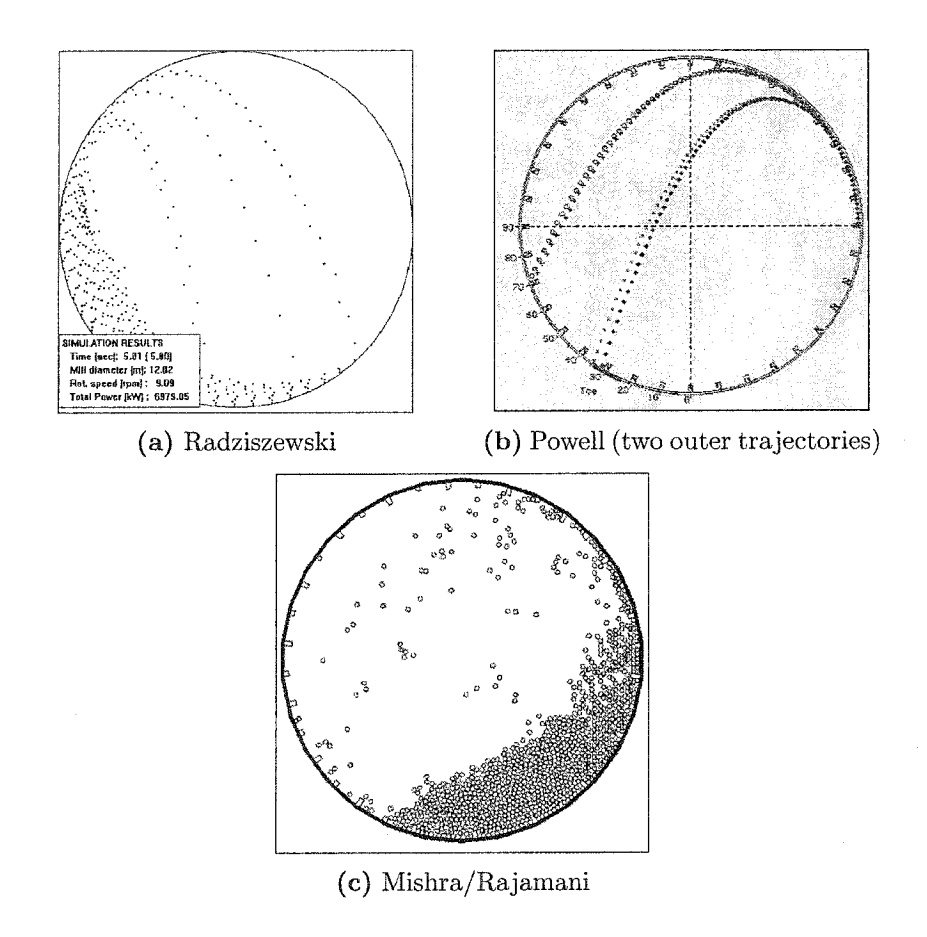


Figure 1.2: Cadia 12 m SAG mill: 75% critical speed, 20 % charge volume, and rectangular hi-lo lifters (Radziszewski, 1999a; Radziszewski and Valery, 1999).

With the help of mill charge motion simulation using the discrete element method (DEM) (Mishra and Rajamani, 1994; Radziszewski and Morrell, 1998), frequency of impact and abrasion events as well as the energy engaged in these processes can be easily determined.

At present, latest trends have been made to describe internal dynamics of mills using the discrete element method (DEM) in comminution research. The figure 1.2 shows typical profiles for three of these efforts.

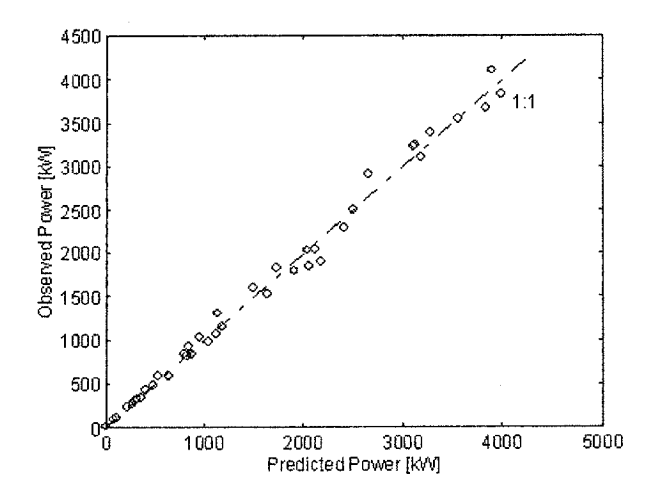


Figure 1.3: Observed vs predicted power (41 ball mills) (Radziszewski and Morrell, 1998).

After successfully simulating mill charge motion, it has become possible to estimate power consumption (figure 1.3) along with the energies dissipated in impact and abrasion as shown in the figures 1.4(a) and 1.4(b). These energies can be used to determine ore breakage and mill liner and media wear.

Primarily, total media wear in a given ball mill grinding process is a product of three wear mechanisms—impact, abrasion, and corrosion (Rajagopal and Iwasaki, 1992). Now it has become possible to define a total media wear model by tying an impact and an abrasion wear model with the energies dissipated in impact and abrasion, as well as incorporating a media corrosion wear model.

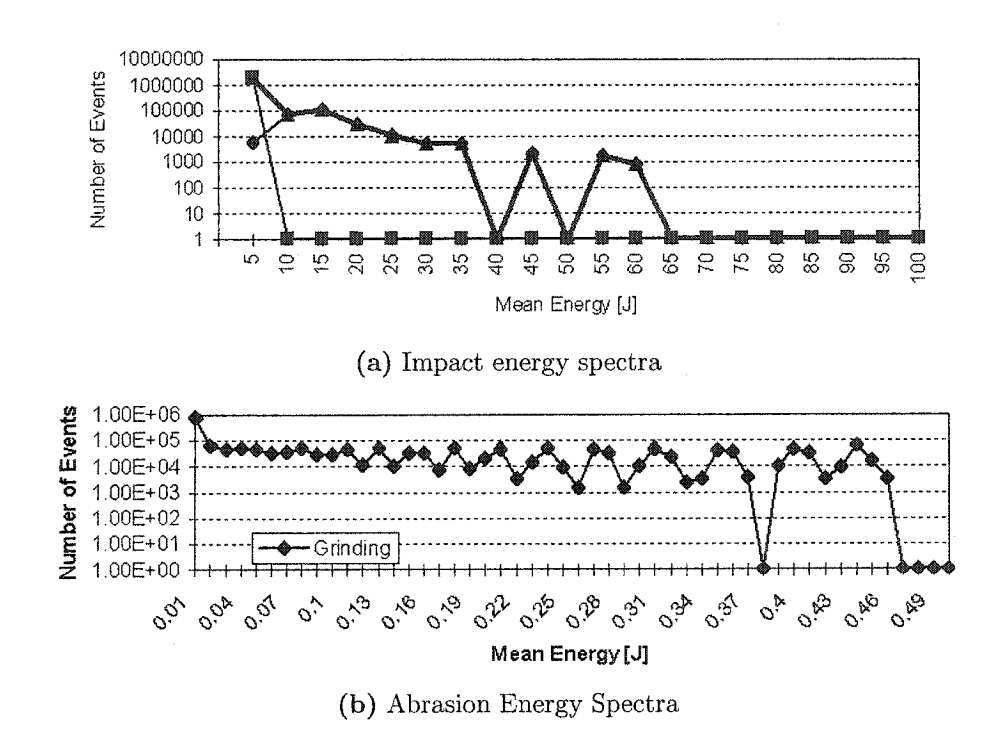


Figure 1.4: Energy spectra for 4.75 m diameter mill (45% filling, 12.5 cm top size ball, unit length) (Radziszewski, 1999b).

#### 1.1. Research in Steel Media Wear Prediction

A ball charge motion profile shows three comminution zones (figure 1.1) that can be distinguished by (i) ball layers sliding over one another grinding material trapped between them, the grinding zone, (ii) balls rolling over one another breaking material in low energy impact, the tumbling zone and by (iii) ball in flight re-entering into the ball charge crushing material in high energy impact, the crushing zone.

It can be assumed that the abrasive wear mechanism, which is defined as the removal of surface material by rubbing or grinding down surfaces (Rao and Nararajan, 1991), is associated with the energy dissipated in the grinding zone. The impact wear mechanism is associated with the energy dissipated in impact in the tumbling and crushing zones, which leaves presence of corrosive wear in the mill (Radziszewski, 1997a).

A total media wear model can be defined on the assumption that the effect of each wear mechanisms can be independently determined and this effect can be tied to mill charge motion as determined or estimated using a charge motion simulator which allows for a total media wear model to be defined as the summation of the wear result of the wear each mechanism (Radziszewski, 1997a).

$$\dot{m}_{total} = \sum_{i=1}^{3} \dot{m}_i \tag{1.1}$$

where i=1,2,3 represents the abrasion, corrosion and impact wear mechanisms respectively.

It is assumed that the contribution of each wear mechanism in eq. 1.1 can be determined using the impact/abrasion energy spectra in the figure 1.4 along with the lab test results. These lab tests were developed from some existing tests.

Abrasive Wear: The abrasive wear characteristics, as a function of applied abrasion force, were determined using steel-on-steel abrasion wheel test where the abrasive was a ground ore. The standard abrasion wheel (Mishra and Finnie, 1980) was used to develop a media abrasion wear test. The test was run dry with abrasion forces ranging up to 100 N and has generated some promising results, in these tests the abrasion angle used in the abrasion wear model decreases exponentially. These results have led to the recommendation that a ball on ball abrasion test should be developed that could generate abrasion forces comparable to that experienced in a real mill. The test should be carried out at slippage speed similar to ones also expected in a real mill. This has led to the design and construction of a new apparatus that could achieve this (Radziszewski, 2001).

Corrosive Wear: The raw corrosion wear characteristics were determined from a batch test using the same ground ore and mill water in order to replicate a similar corrosion environment. A gross corrosion wear rate was determined from this raw data by subtracting an abrasion wear component that was determined using the previous abrasion test results along with the abrasion energy spectrum estimate by a DEM charge motion simulation (Radziszewski, 1997b).

Media corrosion wear has been studied using a small batch mill test and the procedure has been outlined by Gundewar et al. (1990) and Natarajan (1992). In using this test procedure, an abrasion component is determined and subtracted in order to obtain an estimate of batch mill media corrosion. The results generated emphasized the need for temperature control. A lab test with temperature control has been recommended for future development of this test (Radziszewski, 2001).

Impact Wear: Tumbling and free falling grinding media explain the phenomena of impact associated with the energies dissipated in tumbling and crushing zones of the ball charge motion profile (figure 1.1). Most of the studies concerning impact wear have been limited to laboratory scale mill testing methods where impact does not play a significant role (Rao and Nararajan, 1991); however, a couple of studies (Gangopadhyay and Moore, 1987; Xu et al., 1991; Radziszewski and Tarasiewicz, 1993a,b; Scieszka and Dutkiewicz, 1991) have addressed this subject.

In addition to this, three impact testers found in the literature (Blickensderfer and Tylczak, 1989; Xu et al., 1991; Scieszka and Dutkiewicz, 1991) present promising aspect for determining grinding media impact wear. The impact chamber principle shown by the Scieszka and Dutkiewicz (1991) tester presented the most flexible impact wear/impact energy results for different ore-metal-environment combinations.

Initial tests using a modified impact chamber could only generate impact energies equivalent to a 4 cm of drop. Although this could be sufficient for a ball mill where most impact occurs through a tumbling action, this is quite insufficient to study the effect of high energy impact. As a result, it was recommended that a more aggressive test should be designed and fabricated.

Based on these analyses, it is possible to reformulate the eq. 1.1 for a similar ore-metalenvironment industrial context to,

$$m_{total} = \sum_{i=1}^{n_{abr\ int}} m_{abr\ i} (E_{abr\ i}) n_{abr\ i} + \frac{m_2}{A_{l\ ball}} A_{r\ ball} + \sum_{j=1}^{n_{imp\ int}} m_{imp\ j} (E_{imp\ j}) n_{imp\ j}$$
(1.2)

In scaling from laboratory scale data to industrial scale for a specific ore-metal-environment condition experimented, the proportion that each mechanism plays in total wear product depends upon the importance of the energies involved in impact and abrasion as corrosive wear, for similar environment conditions, will be assumed to be the same. As such total wear for a given ball mill environment as shown by the equation 1.2 can be expected to give a wear-time behavior as shown in the figure 1.5 (Radziszewski, 1997a).

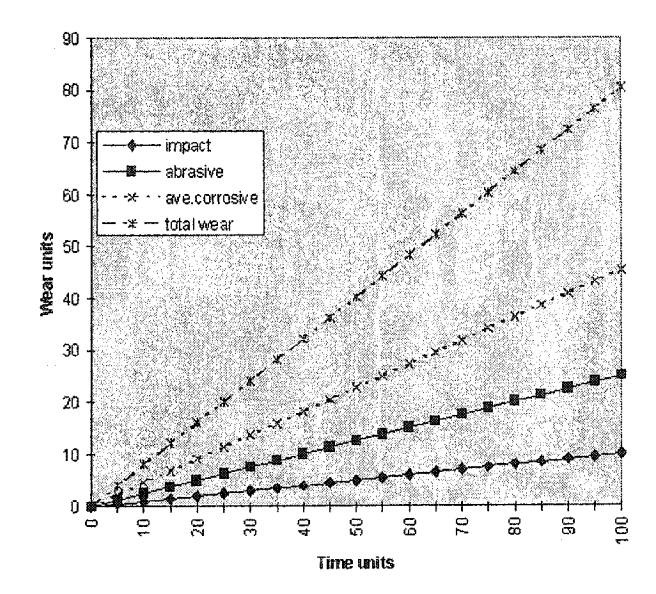


Figure 1.5: Possible total wear as a function of abrasive, corrosive and impact wear.

# 1.2. Exploring Impact Media Wear: Semi-empirical Approach

The basic objective of the impact tester is to determine impact wear for different media types as a function of the energies involved in impact. From a materials science point of view, 3-body opened high stress wear was considered as abrasive and associated with the tumbling and free falling grinding media (Rao and Nararajan, 1991). Impact wear can be characterized as shown in figure 1.6.

Most of the studies concerning impact wear have been limited to laboratory scale mill testing methods where impact does not play a significant role (Rao and Nararajan, 1991); however, a couple of studies (Gangopadhyay and Moore, 1987; Xu et al., 1991; Radziszewski and Tarasiewicz, 1993a; Scieszka and Dutkiewicz, 1991) have addressed this subject. Impact wear per ball  $m_3$  can be described using the adhesion model for wear as a function of energy dissipated in impact  $E_3$ , metal hardness  $H_r$ , metal density  $\rho$  and a wear probability constant  $P_c$  (Radziszewski and Tarasiewicz, 1993a,b; Scieszka and Dutkiewicz, 1991; Dorlot et al., 1986):

$$m_{impact} = \rho \frac{P_c}{3H_r} E_{impact} \tag{1.3}$$

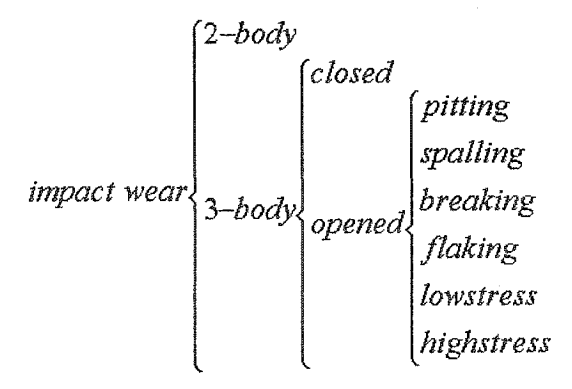


Figure 1.6: Classification of impact wear (Rajagopal and Iwasaki, 1992; Rao and Nararajan, 1991; Blickensderfer and Tylczak, 1989).

As mentioned in the P9L study on exploring total media wear (Radziszewski, 1999b), it has been observed that the laboratory set-up (figure 1.7) although allowing impact variation, did not attain the desired impact energy levels.

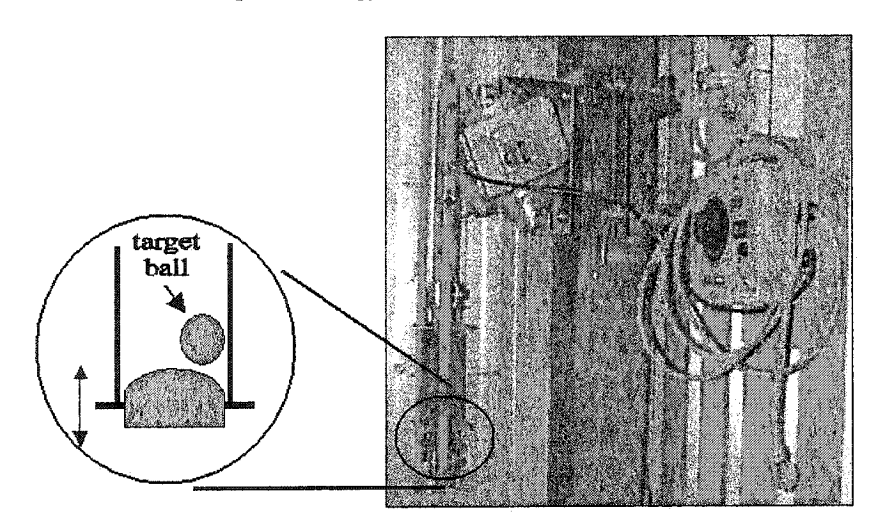


Figure 1.7: Impact chamber test installation (Radziszewski, 2000).

As the impact chamber cannot generate impact energies greater than that equal to a 4 cm drop, a more aggressive test must be developed. An alternative impact test found in the literature is that developed by the BSBM (Blickensderfer and Tylczak, 1989). However, in the USBM (Radziszewski, 2000) impact drop test only one energy level can be determined as drop height is fixed. Drop height of course determines impact velocity.

A new impact tester has been developed that would generate impacts in the order of those found in the USBM media drop test. The design criteria for the newer test is flexibility in impact energies and impact velocities. This has led to the development of a pre-compressed spring cam assembly that can be schematized as in the figure 1.8.

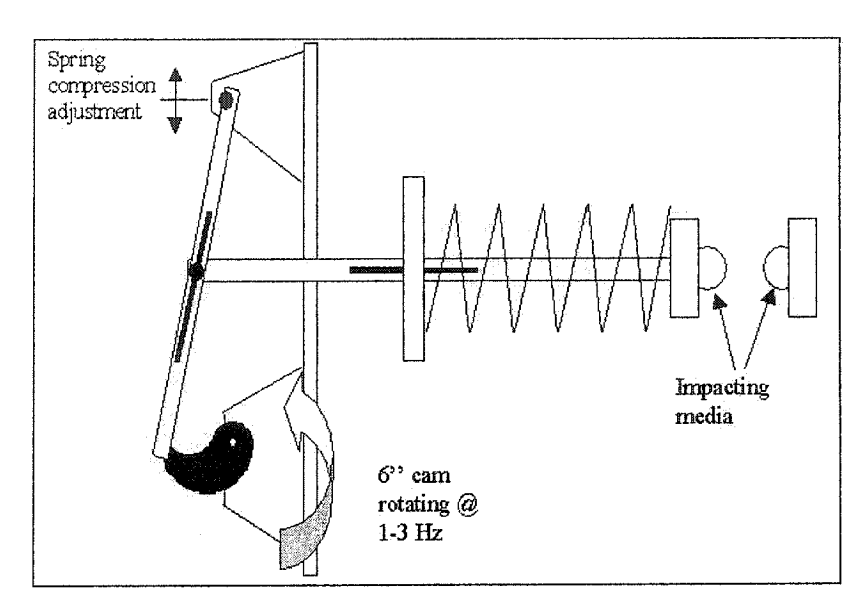


Figure 1.8: Impact test mechanism schematic (Radziszewski, 2000).

In the apparatus, as shown in the figure 1.8, spring pre-tensioning can be adjusted as well as the amplitude of spring compression. The latter is adjusted by raising or lowering the section to which the lever arm, cam, and motor is attached. Compression amplitude can be increased by raising this assembly or decreased by lowering this assembly giving a maximum degree of flexibility in impact testing.

# 1.3. Project Objectives

As stated previously, a new impact wear test assembly needs to be developed that will allow the study of media impact wear over a greater range of energies. Developing this refinement to the impact test allows us to study how impact wear at high energies behaves as a function of those energies. The objective of this research project is to design and develop an impact wear test apparatus that would allow the development of an impact wear model as a function of impact at different high energy levels.

1.3.1. Design and Development. In the first step of this thesis research project, those variables will be determined, which have profound effect on the design of the high energy impact wear tester. Subsequently, a high energy impact tester prototype will be designed using theoretical and computation finite element analyses.

Design changes will be made in order to design an impact wear tester, which will allow to measure the contribution of impact wear to the total media wear at different high levels of energy and to provide adequate media attachments. In the last step of this research project, the high energy impact tester will be developed on the basis of designs produced. Theoretical dynamic calculations for determining speed at impact will also be done.

## 1.4. Organization of the Thesis

This thesis is divided into four distinct parts. The first part involves rigorous formulation of the equations associated with the impact, abrasion, corrosion and total media wear energies. This has been described in the **chapter 1**. The chapter starts with an overview of comminution processes in the mineral industry, followed by formulation of equations associated with the wear energies involved in comminution processes, which forms the basis of decoupled wear mechanism. The second part involves chapters 2 and 3. The **2nd chapter** describes development of **version I** of the impact tester, followed by a brief rationale on the need for developing version II of the impact tester as a consequence of limited applications of the version I impact tester.

The 2nd chapter also gives information about **version II** of the impact tester followed by concept and design of specimen (impactor ball) and target ball holders and fixtures and some test results. This lays the foundation of **theoretical** and **virtual** dynamic analyses of the impact tester mechanism on maximizing speed at impact. This have been explained in the **chapter 3**.

The third part is about the rigorous research work done on **design improvement**, material selection, theoretical and finite element analyses of the impact tester's mobile assembly components for optimizing the version II of the impact tester in order to achieve maximum possible impact speed and better maneuverability to carry out testing. This has been explained in the chapters 4, 5 & 6 in a great detail.

The last part viz. **chapter 7**, mainly involves development, fabrication and setup of **version III** of the impact wear tester prototype. This chapter also includes theoretically calculated speed at the impact.

Finally in the conclusion of the thesis, i.e., **chapter 8**, a summary of the research work is presented and recommendations for the future work are summarized.

# Impact Wear Tester Developments

In this chapter, previous laboratory attempts for determining contribution of impact wear to the total media wear have been outlined. Rationales on the need of developing newer versions have been discussed in the *discussion* sections.

#### 2.1. Version I of the Impact Wear Tester

Three impact testers can be found in the literature (Radziszewski, 1997a) showing promising aspects for determining grinding media impact principle shown by the Scieszka and Dutkiewicz (1991) testers gives the most flexibility for obtaining impact wear/impact energy results for different ore-metals-environment. As presented by these authors: "the proposed method, which simulates the impact action in the tube mill, involves the use of an electromagnetic vibrator (EMV) and a chamber with two balls inside (figure 2.1)".

Using this orientation, an Eriez 40A magnetic drive and controller were modified appropriately in a vertical position and an impact chamber attached as shown in the figure 1.7. The impact chamber was assembled with top and bottom halves being formed of a cut steel ball. Thus it is possible to test ball on ball impact using balls of the same composition and hardness.

Preliminary tests were completed with four media types A, B, C, and D from three mines sites, I, II, and III. It should be noted that media type B contained 12% chrome. The tests at 50 Hz frequency ran for 2.75 hr each with four balls per media type and 2 tests per

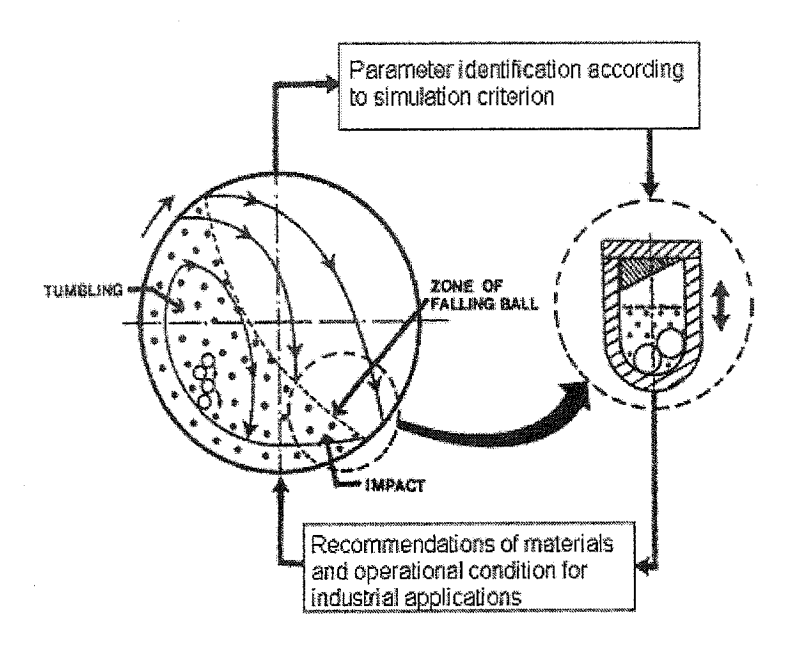


Figure 2.1: Simulative tribo-testing of phenomena inside the tumbling mill.

ball. As for the 225 Hz and 400 Hz frequency tests, they were run for 6 hours each with one ball per media type and 2 tests per ball.

The impact chamber test provides, for a given ball type, a wear product as a function of the energy used in impact. Even though the impact chamber was designed with flexibility in mind, it is necessary to determine the energies involved in impact as both a validation of the starting hypothesis (Radziszewski, 1998) and as a step to translate chamber agitation frequencies with actual ball impact energies.

WorkingModel software was used to determine the impact energies and impact frequencies in the chamber which allows the presentation of the experimental results as a function of these energies as shown in the figure 2.2.

Based on these results, one can propose an exponential function of the form found in the equation 2.1 where impact wear  $m_{imp}$  is expressed as a function of impact energy  $E_{imp}$ . Media B:

$$m_{imp} = 0.0479e^{-8.8387E_{imp}} (2.1)$$

At this point we have from laboratory experimentation a relationship for abrasive wear as a function of abrasive forces in a mill, for corrosive wear as a function of the media surface area present in the same mill and a media impact wear relationship as a function of the

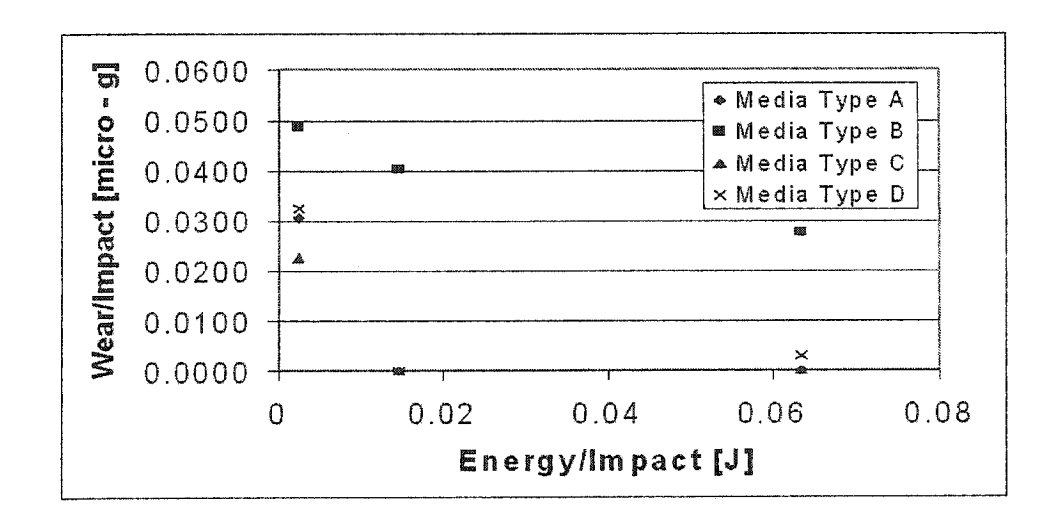


Figure 2.2: Impact wear as a function of impact energy.

energies involved in impact. The impact and abrasion energies and forces are determined from DEM charge motion simulation (Radziszewski, 2002). The resulting contribution has been summed to give an estimate of steel media wear for the cases studied. The resulting wear rates and the contribution of each wear mechanism were determined for 11 mills and 15 operating conditions of which 6 can be found in the figure 2.3.

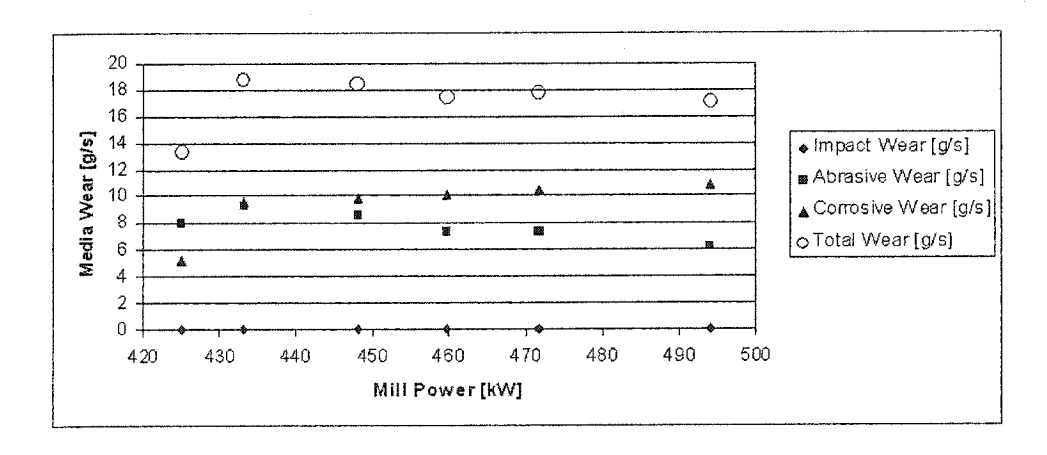


Figure 2.3: Contribution to total media wear.

2.1.1. Verification by Industrial Mill Data. At a particular instant, only total steel media wear can be compared with the estimate determined from the lab. The total

media wear equation can be rewritten as (Radziszewski and Thakur, 2003),

$$m_{media} = k_1 A_{media} + k_2 E_{abr} + k_3 E_{imp} \tag{2.2}$$

where  $m_{media}$  and  $A_{media}$  are determined for a given mill. The abrasion and impact energies  $E_{abr}$ , and  $E_{imp}$  are estimated using charge motion simulation and the constants  $k_1$ ,  $k_2$ , and  $k_3$  are unknown.

As this is a linear equation and one has, for the same mill, media wear and operating cases, one obtains three equations with three unknowns. This defines a simple matrix manipulation to determine the constants  $k_1$ ,  $k_2$ , and  $k_3$ . Having defined the constants, it becomes possible to estimate the impact, abrasion and corrosion contribution to total media wear for the given mill.

From the previous data set, we had 6 mills grinding the same ore (Pb/Zn). These mills were identical except for liner wear in each charge volume. These 6 cases provided the opportunity to average out the  $k_i$  values over 20 combinations of 3 cases. With the calculated  $k_i$  values, it was possible to determine a second estimate of the contributions of impact, abrasion and corrosion to total media as shown in the figure 2.4. (Radziszewski and Thakur, 2003).

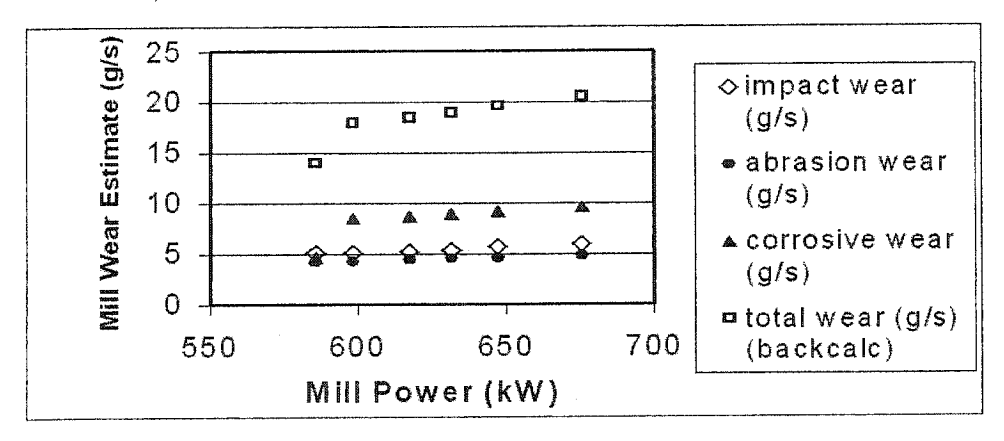


Figure 2.4: Wear results for the six back calculated cases (Pb/Zn ore, 3×4.1 m mill).

Comparing the results found in the figure 2.4 with those found in the figure 2.3, we can see that the estimate for corrosive and abrasive wear are close to those determined from industrial data. However, the impact contribution determined from the laboratory test is almost negligible while that determined from the mill data is far from insignificant. After

making this observation, we can now use the results from the figure 2.4 to correlate with the estimates from the lab experimentation. Figure 2.5 shows a correlation for the impact wear. The resulting correlation factors are applied to all the tested cases (Radziszewski and Thakur, 2003).

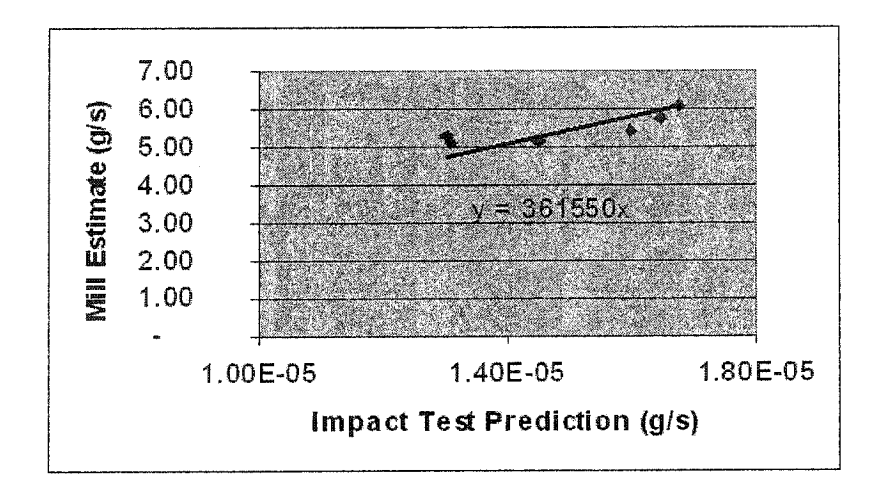


Figure 2.5: Impact wear correlation.

2.1.2. Discussions. Using a simplified wear model and lumped energies in abrasion and impact from DEM simulation, it was possible to estimate from mill data the contribution of impact, abrasion and corrosion. These estimates were used to correlate the individual wear components of the wear model and again compare these results with those from industry giving an overall error of 0% and a standard deviation of 56%. Although this allows yet another improvement in the wear model confidence level, it also outlines that impact wear is not negligible and with a needed correction factor of 366,150 the proposed impact test is not adequate. From WorkingModel simulation, it was found out that the maximum impact velocities were equivalent to a 4 cm drop.

This research aims to design, build, optimize and test a spring loaded reciprocating assembly that would allow prolonged impact testing over a wider range of the impact speeds or drop energies.

## 2.2. Version II of the Impact Wear Tester

As mentioned before version I of the impact tester could only produce 4 cm of drop, a new version of the impact tester was needed to be developed in order to achieve minimum 1 m or 100 cm of drop (Radziszewski, 2000).

Furthermore, the USBM (Blickensderfer and Tylczak, 1989) media drop impact test is limited to one impact energy or rather one drop height. Drop height of course determines impact velocity. The design criteria for our test is flexibility in impact energies and impact velocities. This has led to develop a pre-compressed spring cam assembly that can be schematized as in the figure 1.8.

In this apparatus, spring pre-tensioning can be adjusted as well as the amplitude of spring compression. This latter is adjusted by lowering the section to which the lever arm, cam, and motor is attached. Compression amplitude can be increased by raising this assembly or decreased by lowering this assembly giving a maximum degree of flexibility in impact testing.

2.2.1. Description with some Design Improvements. The impact test apparatus version II (in the process of assembly) can be found in the figures 2.6 and 2.7.

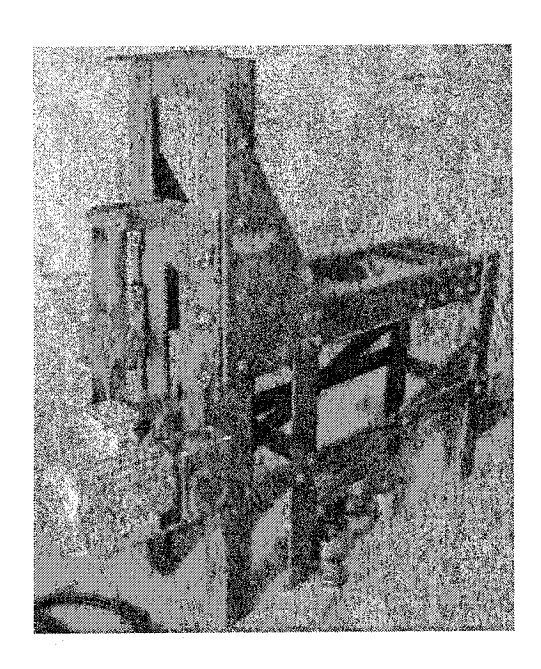


Figure 2.6: The high energy impact wear tester.

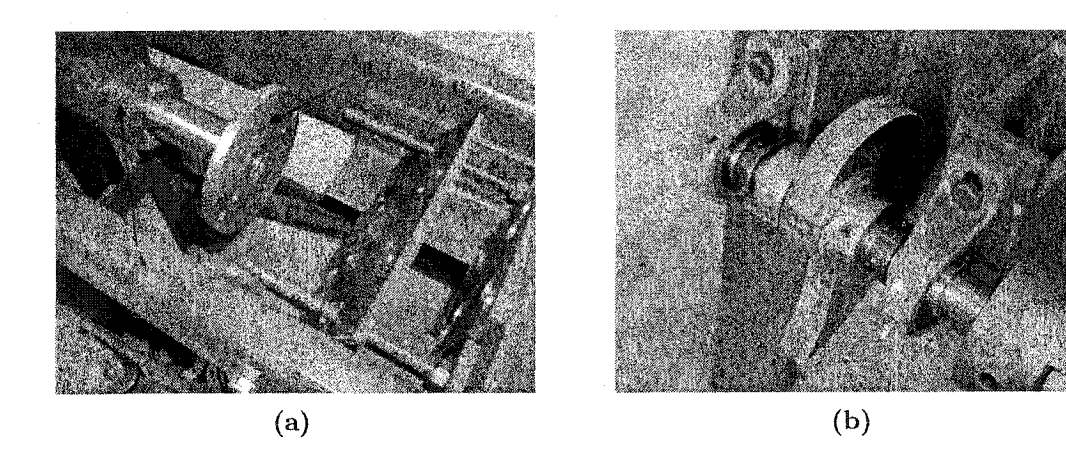


Figure 2.7: High energy impact tester under development: (a) the working end; (b) the cam assembly.

As shown in the figure 2.7(a), A is the spring assembly and housing, B is the impactor end (where an impacting ball will be attached), and C is the target impacting end (where a target ball will be attached). The B and C ends were still underdevelopment.

- 2.2.1.1. Design of the Specimen Holder. Design of the impactor ball (specimen) holder was based on the following requirement:
  - (i) Impactor ball should only have one degree of freedom in the positive x-axis direction with respect to the target ball, in the global coordinate system.
  - (ii) Design should permit easy replacement of the impactor ball.
  - (iii) Impactor ball should not disassemble automatically in the presence of high amplitude of vibrations generated during testing of the prototype.
  - (iv) Holder assembly should be light in weight with a small number of parts.
  - (v) Design should allow low cost and easy manufacturing and assembly of the components.

Based on the above requirement the impactor ball holder assembly was redesigned. Figure 2.8 shows a 3-D solid model of it.

Description of the Ball Holder Assembly. As shown in the figure 2.8, a bullet shape caret was cut from a solid spherical ball with the help of wire EDM (electrical discharge machining) (Fernandes, 2003). This caret is 64.0 mm in length and 38.0 mm in diameter. It is circumferentially surrounded by a cylindrical sheet of high density rubber. When the

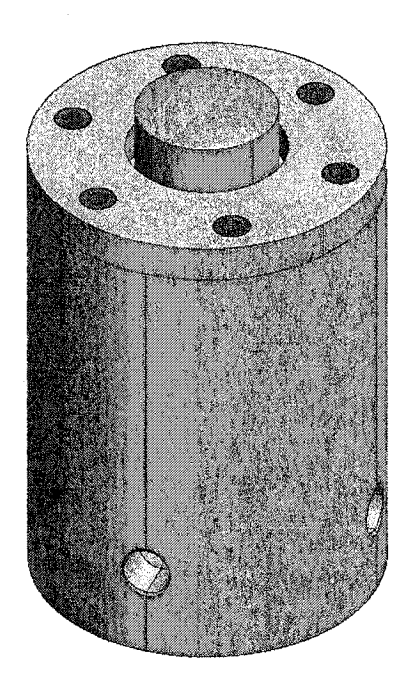


Figure 2.8: Impactor ball holder assembly.

caret holder assembly and the double threaded cylinder are assembled together (figure 2.9), the cylindrical rubber pad exerts a circumferential pressure on the caret due to its buckling, which helps to keep the caret in place and removes unwanted degree of freedoms.

The impactor ball holder has four holes drilled circumferentially on its outer cylindrical surface as shown in the figure 2.8 for turning it efficiently on the outer threads of the double threaded cylinder (figure 2.9).

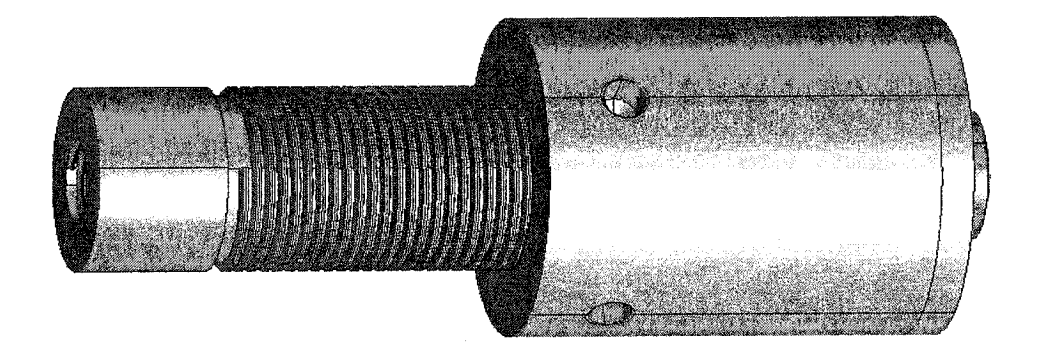


Figure 2.9: Caret holder assembled with double threaded cylinder.

- 2.2.1.2. Design of the Target Ball Holder. With almost similar requirements as of the specimen holder design, design of the target ball holder was based on the following requirements,
  - (i) Target ball should have zero degree of freedoms.
  - (ii) Design should permit easy replacement of the target ball.
  - (iii) Target ball should not disassemble automatically in the presence of high amplitude of vibrations generated during testing of the prototype.
  - (iv) Holder should have a small number of parts.
  - (v) Design should allow low cost and easy manufacturing and assembly of the components.

Based on the above requirements the target ball assembly was redesigned. Figure 2.10(a) shows a 3-D solid model of it.

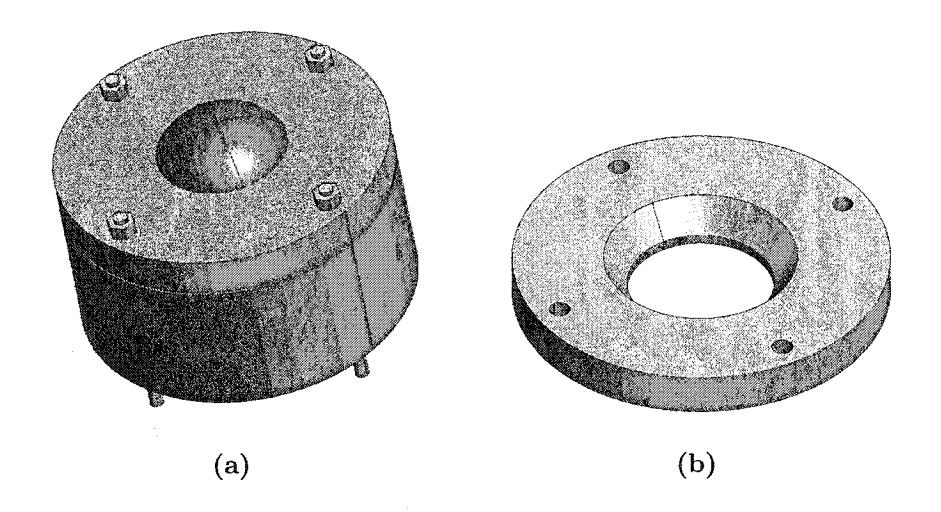


Figure 2.10: Target ball holder assembly: (a) 3-D solid model of the assembly; (b) cylindrical tapered plate.

Description of the Target Ball Holder Assembly. As shown in the figure 2.10(a), a cast steel ball (85mm in diameter) is sandwiched between a tapered upper plate (figure 2.10(b)) and a thick shell cylindrical base (figure 2.10(a)). When all the four pairs of bolts and nuts are fastened together, the cylindrical tapered upper plate exerts a pressure on the cast steel ball thus making it immovable at its place.

The figure 2.11 shows a 3-D model of the version II of the impact tester prototype. As shown in this figure, the caret holder is assembled to the double threaded cylinder and this cylinder is assemble to the spring shaft assembly while this spring shaft assembly is connected to the Lever arm assembly. The spring is inside the stationary spring housing with one end sitting against the stationary plate and the other end in contact with the reciprocating double threaded cylinder.

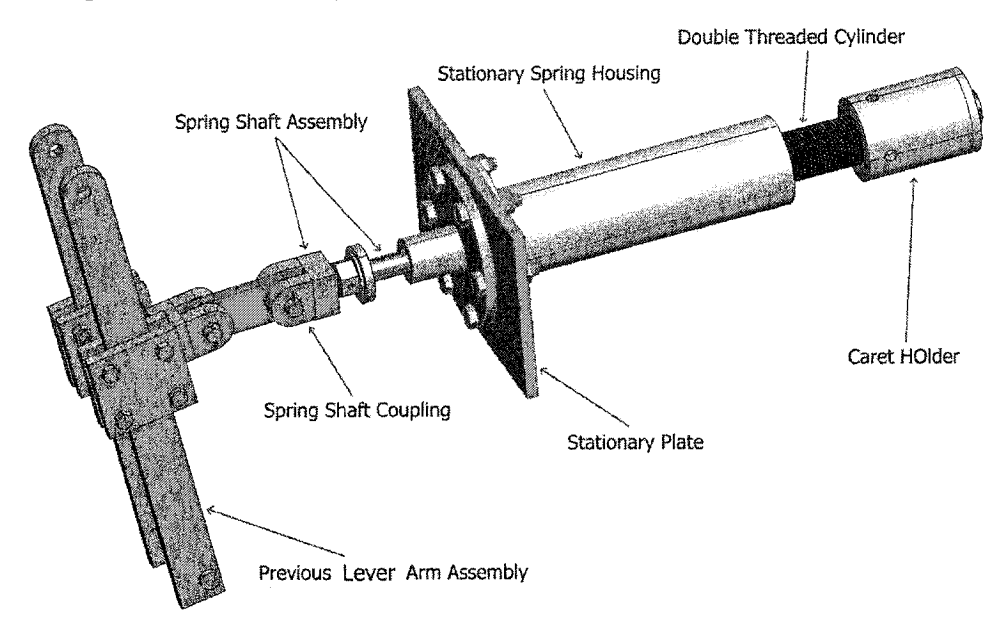


Figure 2.11: A 3-D model of version II of the impact tester assembly.

2.2.2. Initial Test Results. Some tests were carried out on version II of the high energy impact tester in order to validate its performance against a predefined set of goals, which were exclusively focused on achieving maximum speed at impact.

High resolution slotted optical switches were used for measuring speed at impact. The figure 2.12 shows a circuit diagram for the high resolution slotted optical switches (TRW, 1985).

2.2.2.1. Description of the Optical Switches. The OPB813S3 consists of an infrared emitting diode and an NPN silicon phototransistor mounted on opposite sides of a 0.125" (3.18 mm) wide slots. Phototransistor switching takes place whenever an opaque object passes through the slot. The low cost polysulfone housing reduces possible interference from ambient light and provides dirt and dust protection. High resolution position sensing

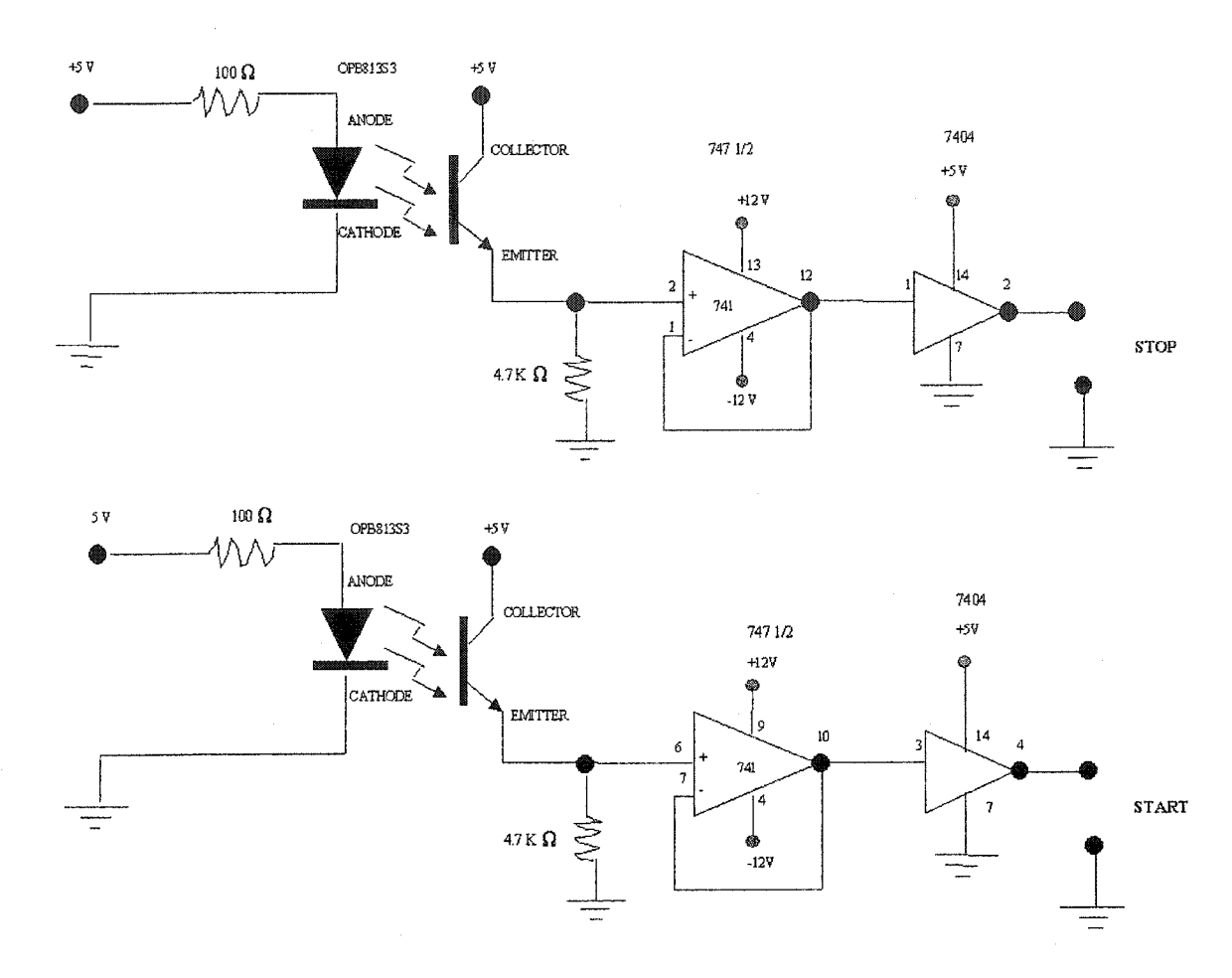


Figure 2.12: Circuit diagram for the high resolution slotted optical switches (type OPB813S3).

is achieved by using standard aperture size of 0.003"×0.040" (0.08mm×1.02mm). The OPB813S3 utilizes an OP140 or OP240 LED and OP550 family sensors (TRW, 1985).

2.2.2.2. Description of the Circuit Diagram. As shown in the figure 2.12, two optical switches were used to trigger (start and stop) the electronic counter with at least a millisecond count. In this circuit, operational amplifiers (OPB813S3) work as a non inverting voltage follower, which have a high impedance at the input and a low impedance at the output. The main purpose of the OPAMs was to match the impedance of the circuit to the impedance of the electronic counter. Invertors were used to invert the signals because the electronic counter can only be triggered by rising pulse in the output voltage waveforms.

Figure 2.12 shows a commonly used circuit for using this slotted optical switch. Use a resistor  $R_1$ =100 $\Omega$  in series with the LED to provide a current of about 50mA using the 5 V power supply from the workbench. Resistor  $R_2$ =14.7K $\Omega$  acts as a pull-down resistor when the phototransistor is OFF and creates the desired voltage drop when the phototransistor is turned ON. For initial testing purposes an oscilloscope was used to measure and note the output voltage waveforms as an opaque object is moved in and out of the slot of the emitter/detector pair.

The circuit gets broken, when an opaque object passes through the slot of the first optical switch, during this transition the potential difference between emitter and the circuit until invertor is 0.0 V. Invertor inverts this signal to 5.0 V signal. Afterwards this signal is send to the electronic counter, which thus works as a start signal. The electronic counter counts the number of pulses until it gets a stop signal from the  $2^{nd}$  optical switch, which works in a similar manner and is generally placed at a predefined fixed distance from the  $1^{st}$  optical switch.

The time measured by the electronic counter between successive start and stop signals is the time taken by an object to travel through the predefined fixed distance. With the help of velocity = distance/time relation, velocity can easily be calculated.

Assumptions taken during Observations,

- (i) The system was assumed to be a frictionless system.
- (ii) Acceleration gradient was assumed to be equal to zero.
- 2.2.2.3. Test Setup and Results. As described above, two optical switches were installed near the physical prototype at a predefined fixed distance of 7.00 mm in order to measure speed at impact. A silver plastic strip (reflector) was attached to a moving component of the reciprocating mechanism, which acted as an opaque object.

A medium pressure die spring (color coded blue) with a spring constant ( $\kappa$ ) = 29.427 N/mm (Producto, 1996) was used. The coupling was positioned on the vertical arm in such way that the spring compression within the efficient operating range (25 %-35% of free length) could be achieved (Producto, 1996). The spring was compressed for approximately 4" or 101 mm, which is 33.33% of its free length (12" or 304.8 mm). The observations are summarized in the table 2.1.

S. No.	Time (milliseconds)	$oxed{ ext{Velocity, } \dot{\mathbf{x}_f} \ ( ext{m/sec})}$
1	4.433	1.579
2	4.689	1.492
3	4.474	1.564
4	4.471	1.565
5	4.837	1.447
6	4.864	1.438
7	4.807	1.456
8	5.035	1.390
9	5.348	1.308
10	4.526	1.546
11	5.244	1.334
12	5.364	1.304
13	5.380	1.301
14	5.648	1.239
15	5.101	1.372
16	5.474	1.278
17	5.415	1.292
18	5.719	1.224
19	4.353	1.607
20	5.729	1.222
Average =	5.046	1.387

Table 2.1: Observations from the optical switches for measuring speed at impact.

From Newton's first law of motion,

$$\dot{x}_f = \dot{x}_i + \ddot{x}t \tag{2.3}$$

initial velocity is zero, therefore  $\dot{x}_i = 0$ . Acceleration can be expressed in terms of gravitation acceleration (9.81 m/sec<sup>2</sup>), because here we are interested in calculating velocity at impact equivalent to the height of drop, i.e., h (m or cm). Here  $\dot{x}_f$  is the final velocity of a moving object.

Therefore the eq. (3.3) can be rewritten as,

$$\dot{x}_f = gt \tag{2.4}$$

Thus, t can be calculated as,  $t = \dot{x}_f/g \Longrightarrow t = 1.387/9.81 = 0.141~sec$ 

From the Newton's third law of motion,

$$x = \dot{x}_i t + \frac{1}{2} g t^2 = \frac{1}{2} \dot{x}_f t = \frac{1}{2} \times 1.387 \times 0.141 = 0.098 \ m = 9.8 \ cm \tag{2.5}$$

Therefore from the above equation, the equivalent drop of height comes out to be equal to 9.8 cm.

- 2.2.2.4. Errors in the Results. Following errors were found in the results,
  - (i) optical switches were very sensitive to high amplitude of vibrations produced by the mechanical system during its operation and
  - (ii) electronic counter couldn't be calibrated properly, which is why its readings could have had a moderate degree of error.
- 2.2.3. Discussions. Because of above mentioned errors in the observation, optical switches couldn't be used for further measurements. These errors led to the conclusion that optical switches are only useful for measuring speeds when prototypes do not produce high amplitude vibrations. This is why use of a high-speed camera has been recommended for measuring speed at the impact while running tests on the modified version (version III) of the impact wear tester.

# Theoretical and Virtual Dynamics of the Impactor Mechanism

As stated in the previous chapter, when the version II of the impact device was tested with a medium pressure die spring ( $\kappa = 29.427 \text{ N/mm}$ ) (Producto, 1996), maximum speed at impact was found to be equivalent to 9.8 cm of drop. This speed at impact was not sufficient to validate the impact tester's performance and impact wear as a function of impact energy.

The dynamics of the impactor mechanism was defined in order to achieve the following objectives,

- (i) more aggressive impact tester needed to be developed, which can produce at least 1 m (100 cm) of equivalent of drop, when the strongest spring ( $\kappa = 124.717$  N/mm) (Producto, 1996) is used with different compression amplitudes,
- (ii) which can easily be adjusted and operated according to the requirements, and
- (iii) safer for the operator to operate.

#### 3.1. Description of the Impactor Mechanism

As shown in the figures 1.8 and 3.1, a 6" or 152.4 mm cam rotates at the speed of 1 to 3 hertz in counter clockwise direction and drives a follower attached to the Lever arm.

In this impactor device, compression or displacement of the spring can be adjusted according to the following principle,

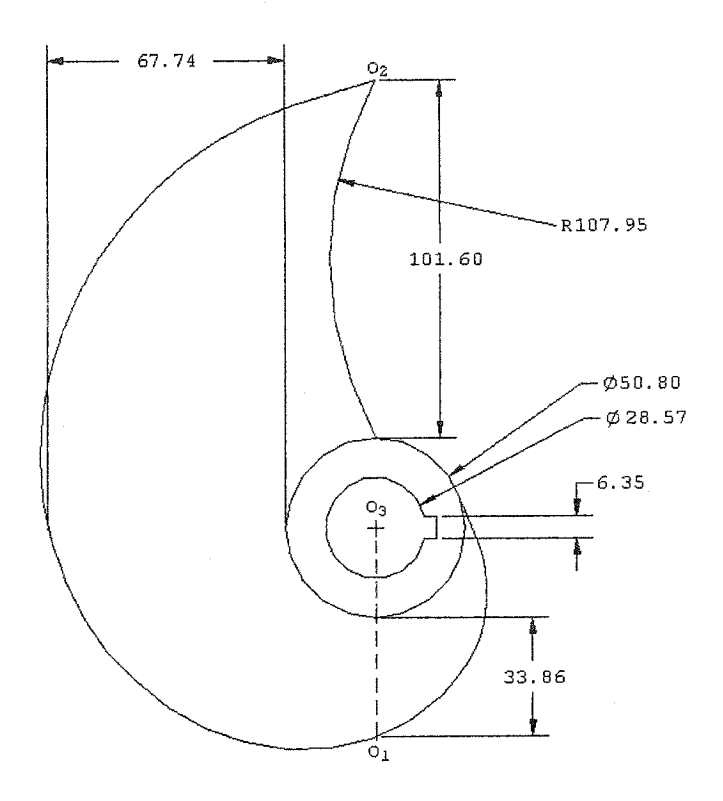


Figure 3.1: Cam profile in mm (Girard, 2000).

in the arc, angle and radius relationship, for a given angle  $\theta$ , length of arc l is directly proportional to the radius r. It can be expressed in the following way (Greenspan and Benney, 1973),

$$\theta = l_{arc}/r \implies l_{arc} = \theta r$$
 (3.1)

For a constant value of angle  $\theta$ , eq 3.1 can be modified as,

$$l_{arc} \propto r$$
 (3.2)

Based on the above explained principle, amplitude of compression or displacement of the spring can be adjusted by raising or lowering the section to which the Lever arm, cam, and motor is attached (figure 1.8). Compression amplitude can be increased by raising this assembly or decreased by lowering it giving a maximum degree of flexibility in the impact testing.

Since maximum radius of the cam is 6" (152.4 mm), therefore compression amplitude of the spring cannot exceed this value.

The rotating cam leaves the follower when both attain the highest point of contact, as shown in the following figure.

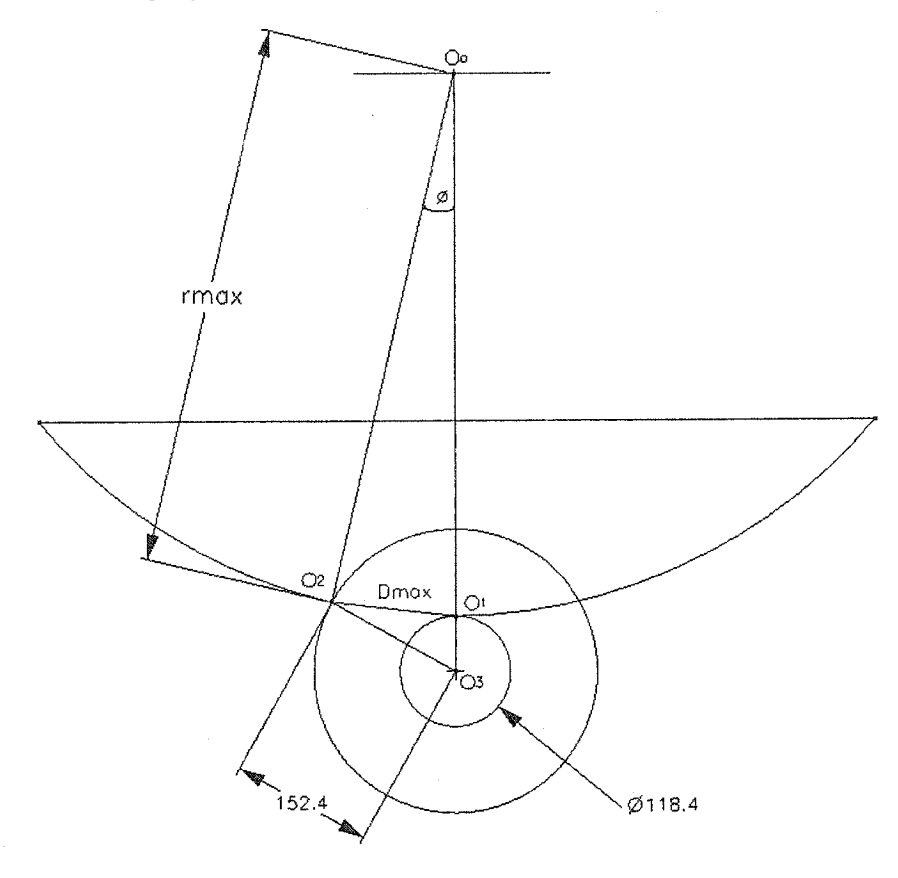


Figure 3.2: Path traced by the cam-follower contact point (all dimension are in mm).

As shown in the figures 3.1 and 3.2, the contact point at the follower (location  $O_1$ ) rotates at a radius of  $r_{max}$  from the pivot point O. The contact point at the cam (location  $O_1$ ), which is situated at a distance of  $r_{max}$  from the pivot point  $O_o$ , rotates from the initial value of radius (59.20 mm) to the maximum value of radius (6" or 152.40 mm). After leaving the cam (location  $O_2$ ), the follower moves rapidly in the forward direction along with the Lever arm assembly under the influence of potential energy delivered by the compressed spring. This assembly moves until the caret, which is assembled at the forefront of mobile assembly, collides with the stationary target ball.

As shown in the figure 3.2, the cam-follower contact point moves back and forth between locations  $O_1$  and  $O_2$ .

Derivations for calculating spring displacement generated by cam rotation, torque, and velocity at the impact can be found in the following sections along with force and moment diagrams.

#### 3.2. Theoretical Dynamics of the System

Generally dynamics of any mechanical system comprises of displacement, force, moment, torque, and velocity associated with it. In this section, the impact tester mechanism has been defined on the basis of above mentioned physical properties.

3.2.1. Derivation for Calculating Dynamic Parameters. The impactor mechanism is mainly comprised of spring displacement as a result of cam rotation, moment about the pivot point  $O_o$ , torque delivered by cam for generating desired spring displacement and speed at impact.

3.2.1.1. Derivation for Calculating Spring Displacement. In the triangle  $O_0$ ,  $O_3$  and  $O_2$  (figure 3.2)  $\angle \phi$  ( $\angle O_2 O_0 O_3$ ) can be calculated as (Greenspan and Benney, 1973),

$$(O_3O_2)^2 = (O_2O_0)^2 + (O_0O_3)^2 - 2(O_2O_0)(O_0O_3)\cos\phi$$
(3.3)

For a small angular displacement, in the triangle  $O_0$ ,  $O_1$  and  $O_2$ ,  $D_{max}$  or maximum displacement of the spring for a radius  $r_{max}$  (figure 3.2) can be calculated as (Greenspan and Benney, 1973),

$$D_{max} = 2\sin(\phi/2)r_{max} \tag{3.4}$$

Since the value of  $\angle \phi$  is constant for a given set of lengths therefore a formula can be derived as,

$$D_i = kr_i i = 1, 2, 3, \dots (3.5)$$

where  $r_i$  is a variable radius defined as the distance between coupling axis and the axis of rotation, which passes through the pivot point  $O_0$  and k is a constant, which depends on the dimensions of the Lever arm and the cam.

With the help of equation 3.5, displacement or compression amplitude of the spring can be easily calculated for the different positions of coupling on the Lever arm with respect the pivot point  $O_0$ .

3.2.1.2. Derivation for Calculating Moment and Force. For the impact tester mechanism, force and moment can be derived by taking the moment about the pivot point  $O_0$  as shown in the figure 3.3. The relation between amplitude of spring compression (refer

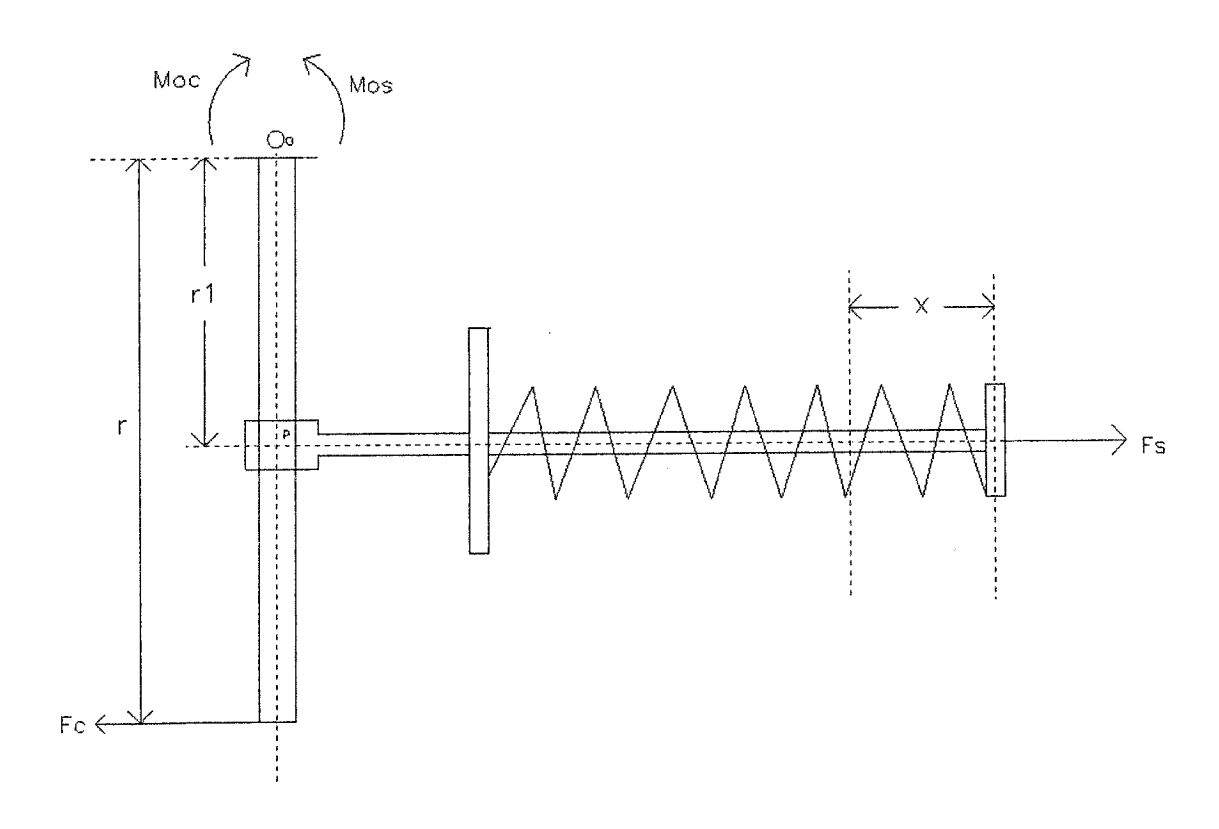


Figure 3.3: Force-moment diagram for the impactor mechanism.

figures 1.8, 3.25 and 3.3) and the force needed to compress it can be expressed as,

$$F_s = \kappa x \tag{3.6}$$

where,  $\kappa$  is a force constant in N/mm, x is the compression amplitude in mm and  $F_s$  is the magnitude of the force needed to compress the spring for a compression amplitude of x mm in N.

Since the line of action of the spring force is at a vertical distance of  $r_1$  from the pivot point  $O_0$ , therefore a counter-clockwise moment about this point can be expressed in the following way,

$$M_{os} = F_s r_1 = \kappa x r_1 \tag{3.7}$$

where,  $M_{os}$  is a moment about the pivot point  $O_0$  in Nmm.

If the magnitude of cam force needed to compress the spring by an amplitude of x on the follower is  $F_c$  in N then an expression can be derived by taking moments about a common pivot point  $O_0$  in order to relate  $F_c$  and  $F_s$ .

Since line of action of cam force is at a vertical distance of r from the pivot point  $O_0$ , therefore a clockwise moment  $(M_{oc})$  about this point can be expressed in the following way,

$$M_{oc} = F_c r \tag{3.8}$$

According to the Lever principle, in equilibrium net moment about the pivot point  $O_0$  will be equal to zero. Therefore,

$$M_{oc} - M_{oc} = 0 \Longrightarrow M_{oc} = M_{os} \tag{3.9}$$

From the equations 3.7, 3.8, and 3.9, an expression for calculating cam force needed to compress the spring for an amplitude of x mm can be derived as,

$$F_c = F_s r_1 / r \quad Newton \tag{3.10}$$

3.2.1.3. Derivation for Calculating Torque. Torque is the cross product between a force and the distance of the force from a fulcrum (the central point about which the system turns). The cross product takes only the component of the force acting perpendicular to the distance. Using trigonometry the torque is defined as (Jennings and Obert, 1950),

$$Torque = Force \times Distance \ to \ fulcrum \times sin(\theta) \tag{3.11}$$

In this laboratory the force will be perpendicular (90) to the distance. The sine of 90 is one, therefore the torque will be,

$$Torque = Force \times Distance \ to \ fulcrum \tag{3.12}$$

If the maximum radius of the cam is  $R_{cam}$ , therefore by using the relationship established in the eq. 3.12, an expression for calculating maximum torque  $(T_{max})$  delivered by the cam under equilibrium condition can be written as,

$$T_{max} = F_c \times R_{cam} = F_s r_1 / r \times R_{cam} \tag{3.13}$$

or

$$T_{max} = \frac{r_1}{r}(\kappa x) \times R_{cam} \tag{3.14}$$

where  $R_{cam}$  is the maximum radius of the cam, which is equal to 6" or 152.40mm.

3.2.1.4. Derivation for Calculating Speed at the Impact. Equation for calculating speed at the impact can be derived from the law of conservation of energy; in other words, the amount of input energy is equal to amount of output energy.

In case of reciprocating impact mechanism potential energy stored in the spring media will be delivered to the reciprocating mass and Lever arm, out of which some amount of energy will be lost in overcoming the friction. Since all the moving parts are very well lubricated therefore we can assume that the frictional energy loss would be minimal but measurable.

As stated earlier potential energy stored in the spring can be expressed as,

$$E_{ps} = \frac{1}{2}\kappa x^2 \tag{3.15}$$

where  $E_{ps}$  is the potential energy stored in the spring in Nmm or Nm. This energy will be converted into momentum energy and some part of it will be lost in overcoming the friction.

Momentum energy  $(E_{mrc})$  for the reciprocating components can be expressed as,

$$E_{mrc} = \frac{1}{2} (W'_{rc}) v_{imp}^2 \tag{3.16}$$

where,

 $v_{imp}$  = Speed at the impact in m/sec.

 $W'_{rc}$  = Total weight of the reciprocating components in kg.

Momentum energy  $(E_{mvc})$  for the rotating components (Lever arm assembly) can be expressed as,

$$E_{mvc} = \frac{1}{2} (W'_{la} \cos \phi) v_{imp}^2$$
 (3.17)

where,

 $W'_{la}$  = Weight of the Lever arm assembly in kg.

 $\phi$ = Angular displacement of the Lever arm in radians.

As we can see from the equation 3.17, only vertical component  $(W'_{la}\cos\phi)$  of the Lever arm assembly is considered due to the fact that only this component would oppose the motion.

Horizontal inertial component of the Lever arm assembly will help the spring to restore its original length, therefore momentum energy  $(E_{mhc})$  associated with this component will be added to the input energy to the system, it can be expressed as,

$$E_{mhc} = \frac{1}{2} (W'_{la} \sin \phi) v_{imp}^2$$
 (3.18)

Part of the input energy lost in overcoming the friction  $(E_{fva})$  for the Lever arm assembly can be expressed as,

$$E_{fva} = \mu_{dr} W_{la}' \cos \phi(\phi r_p) \tag{3.19}$$

where,

 $\mu_{dr}$ = coefficient of dynamic rolling friction for the rotating mass (Lever arm), and  $r_p$ = radius of the pivot pin about which the Lever arm is hung in mm, which is equal to 5/16" or 7.94mm.

Part of the input energy lost in overcoming the friction  $(E_{frc})$  for the reciprocating components assembly can be expressed as,

$$E_{frc} = \mu_{ds} W_{rc}' D_i \tag{3.20}$$

where,

 $\mu_{ds}$  = coefficient of dynamic sliding friction for the reciprocating components assembly, and  $D_i$  = displacement or compression amplitude of the spring in mm.

Now, an expression for calculating speed at the impact can be written as,

$$E_{ps} + E_{mhc} = E_{mrc} + E_{mvc} + E_{fva} + E_{frc} + E_{abs}$$
 (3.21)

where  $E_{abs}$  is the maximum energy absorbed by the Lever arm during loading conditions, which is equal to  $1/2Ff_{max}$ . Where F is the load on the Lever arm in N and  $f_{max}$  is the maximum deflection of it under the influence of force F in mm. The equation 3.21 can be

rewritten as,

$$E_{ps} + \frac{1000}{2} (W'_{la} \sin \phi) v_{imp}^2 = \frac{1000}{2} (W'_{rc} + W'_{la} \cos \phi) v_{imp}^2 + \mu_{dr} W'_{la} \cos \phi (\phi r_p) + \mu_{ds} W'_{rc} D_i + E_{abs}$$
(3.22)

or

$$v_{imp} = \sqrt{\frac{\kappa x^2 - 2[\mu_{dr} W'_{la} \cos \phi(\phi r_p) + \mu_{ds} W'_{rc} D_i] - F f_{max}}{1000[W'_{rc} + W'_{la} \cos \phi - W'_{la} \sin \phi]}}$$
(3.23)

For a particular set of conditions i.e., spring constant, spring displacement etc. x and  $D_i$  would be equal, therefore equation 3.23 can be rewritten as,

$$v_{imp} = \sqrt{\frac{\kappa D_i^2 - 2[\mu_{dr}W'_{la}(\phi r_p)\cos\phi + \mu_{ds}W'_{rc}D_i] - Ff_{max}}{1000[W'_{rc} + W'_{la}\cos\phi - W'_{la}\sin\phi]}}$$
(3.24)

with help of above equation 3.24, speed at the impact can be easily calculated in m/sec.

In the expression 3.24, static coefficients of friction were not taken into account due to the fact that torque delivered by the prime mover, which is coupled with the cam is very high, which makes static coefficients of friction insignificant.

#### 3.3. Virtual Dynamics of the System

As mentioned in the beginning of this chapter, dynamics of the impactor mechanism was defined in order to maximize its performance. The basic objective was to achieve maximum speed at the impact.

In order to verify theoretical dynamics and to determine the effect of different variables of the dynamic system like weight of the moving components, spring constant, etc. on the speed at impact, a virtual prototype was built using a very powerful virtual prototyping simulation software.

3.3.1. Benefits of Functional Virtual Prototyping. ADAMS (Automatic Dynamic Analysis of Mechanical Systems) was used for aforementioned purpose in order to simulate, understand and quantify the performance of the mechanical systems before committing to expensive hardware prototypes or conduct numerous physical tests and to develop consistent virtual prototypes that guide in making critical design decisions.

With ADAMS/View, a virtual prototype of the mechanical system was built just as the physical prototype can be built by creating parts, connecting them with joints, assembling the system, and driving it with physically accurate forces and motions. Springs, dampers, contacts, and friction were applied in order to improve the fidelity of the simulation. Following are the benefits of using ADAMS/View software package (ADAMS/View 12.0, 2001).

- Quickly build and review models for simulation.
- Improve efficiency by automating process through customization.
- Manually change design parameters and compare iterations to answer what-if questions about the design.
- Visually share design ideas with the product development teammates.

3.3.2. Impact Tester Virtual Modelling. The steps that were used in ADAMS/View to create a model mirror the same steps that were used to build the physical prototype. The figure 3.4 shows a sequence of the design process, which was followed according to the requirements.

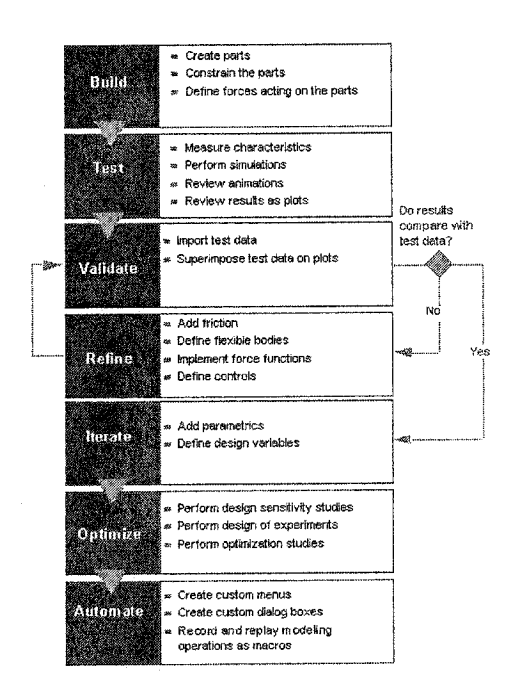


Figure 3.4: Design process steps (ADAMS/View 12.0, 2001).

ADAMS/View's built-in CAD package was used for 3-D solid modelling of the physical prototype. Distances and component dimensions were taken from the physical prototype. All the motion constraints were defined in the forms of joints and contacts between two moving components.

Strongest spring with the spring constant equal to 124.717N/mm (Producto, 1996) was modelled in the virtual prototype for the maximum possible compression amplitude in order to determine the following parameters critical for the design,

- maximum possible speed at the impact,
- maximum torque needed to compress the spring,
- magnitude of force or load on the Lever arm and on the other components,
- effect of weight of the moving components on the impact speed,
- effect of friction on the impact speed, and
- position of the target ball for transmitting maximum impact force during collision.

3.3.2.1. The Virtual Dynamic Modelling. Virtual prototype was built on the steps shown in the figure 3.4 i.e., in the first phase parts were created, constraints were applied and forces were defined using ADAMS/View's libraries.

A dynamic simulation provides a time-history solution for displacements, velocities, accelerations, and internal reaction forces in a model driven by a set of external forces and excitations (ADAMS/Solver, 2001).

Dynamic simulations are transient or time-varying simulations used to investigate the movements of parts over time; these movements result from the combined effects of forces and constraint relationships.

Dynamic simulations can be performed on models that have any number of degree of freedoms (DOFs). Important Solver Settings (category: dynamics) were set as shown in the figure 3.5 for running simulation for the virtual model.

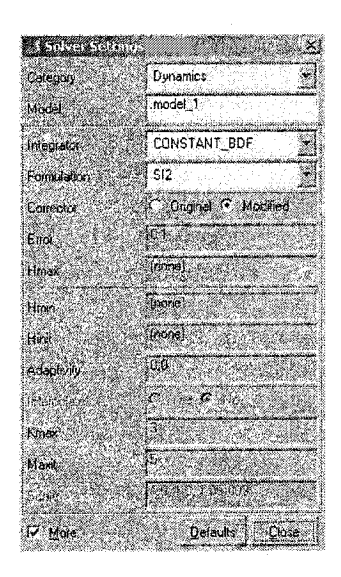


Figure 3.5: Solver settings: dynamics.

After comparing all the available *integrators* in the solver setting library, the CON-STANT\_BDF (Constant Backward Differentiation Formulation) integrator was chosen along with the SI2 (Stabilized-Index Two) (ADAMS/Solver, 2001) formulation because of the following reasons,

- CONSTANT\_BDF is a modification of the DIFSUB (Differential Substitutions) integrator, to make it behave like a stable, fixed-step integrator. It is a variable-order, predominantly fixed-step, multi-step integrator, with a maximum order of six. Because it is a BDF (Backward Differentiation Formulation) method, it is stiffly stable, that is, it can solve stiff problems efficiently without becoming unstable.
- If the corrector fails to converge, CONSTANT\_BDF reduces the step size until the corrector converges and it is very robust and stable at small step sizes when used with the Stabilized Index-2 (SI2) formulation.
- CONSTANT\_BDF tends to run at the maximum allowable KMAX, where KMAX
  specifies the maximum order that the integrator can use. A high integration order implies greater accuracy. Coupled with explicit step size control, the use of
  a high integrator order normally results in quite accurate solutions.

3.3.3. Simulation Results. Several simulation runs were executed for refining and updating the virtual prototype. But here only the three most important simulation runs have been summarized, which had the greatest impact on the new design of the impactor mechanism. While using ADAMS for the simulation purposes, it was assumed that the Lever arm would not absorb any portion of the input energy due to its displacement because in the simulation it was modelled as a *rigid body* (ADAMS/View 12.0 Help, 2001). But in real practice, the Lever arm will absorb some portion of input energy because of its bending.

3.3.3.1. Virtual Modelling Parameters. Simulations were run for 2.5 seconds with a total of approximately 3400 frames in order to simulate like a very precise high speed camera with approximately 1400 frames/sec. The strongest spring ( $\kappa = 124.717~N/mm$ ) with a compression amplitude of 95.80  $\approx$  96.00 mm was modelled for all the simulation runs in order to simulate the toughest testing conditions.

The figure 3.6 shows compression amplitude of the spring calculated by the *ADAMS PostProcessor*. Effects of weights of moving components and friction on the speed at the impact were determined for the aforementioned testing conditions.

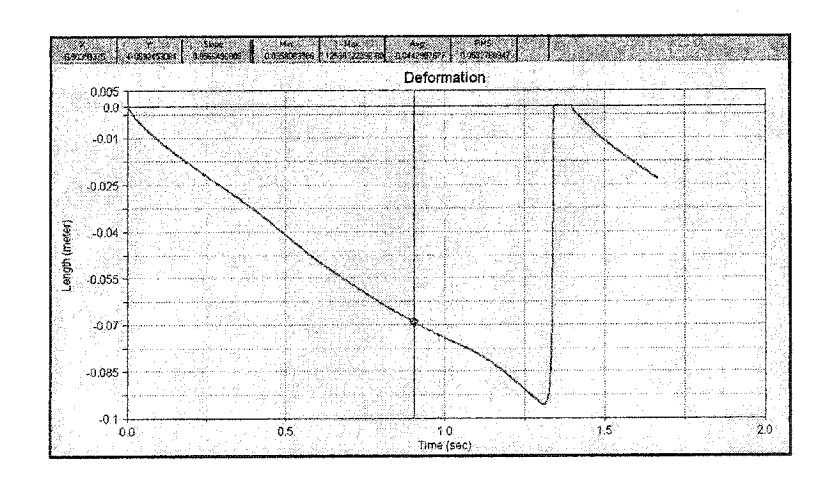


Figure 3.6: Spring deformation from ADAMS simulation.

3.3.3.2. The First Simulation Run. In the first simulation run, full weight of all the moving components and a value of 0.35 (ADAMS/View 12.0 Help, 2001) as a friction coefficient for the Lever arm pivot as well as for the reciprocating components were simulated. From the simulation, maximum speed at the impact was found to be equal to 4.5 m/sec.

The table 3.1 shows weight of all the moving components measured from version II of the impact tester.

S. No.	Component Name	Weight (kgs)
1	Caret Holder with Caret	1.9
2	Double Threaded Cylinder	2.9
3	Spring Shaft Assembly	4.0
4	Vertical Arm Assembly	12.3

Table 3.1: Weight of all the moving components from version II of the impact tester.

3.3.3.3. The Second Simulation Run. In the second simulation run, weight of all the moving components and friction coefficient (by assuming proper lubrication and improvement in the design) were halved. The following figure shows speed at the impact in m/sec.

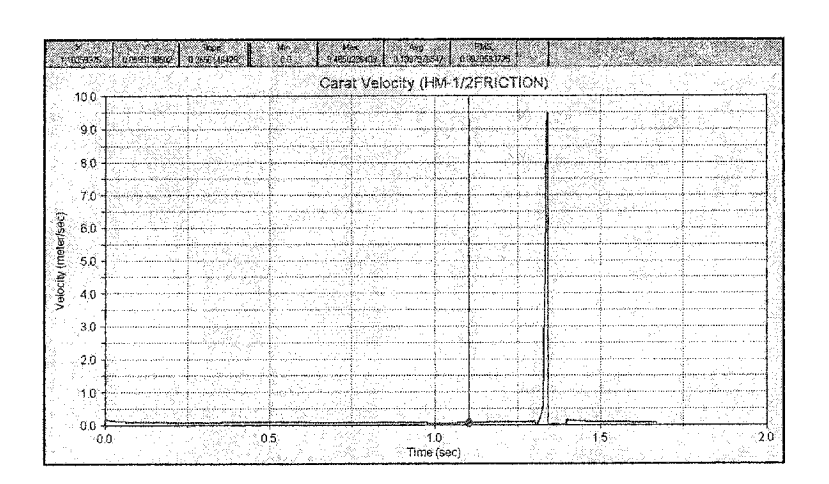


Figure 3.7: Speed at the impact: second simulation run.

As it can be seen from the figure 3.7, maximum speed at the impact was found to be equal to 9.48 m/sec from the simulation.

3.3.3.4. The Third Simulation Run. In the third simulation run, friction coefficient and weight of all the moving components except weight of Lever arm assembly were kept the same as the second simulation run. In this simulation run weight of the Lever arm assembly was reduced to one forth of its original value in order to determine its effect on the speed at the impact precisely. Figure 3.8 shows speed at the impact in m/sec.

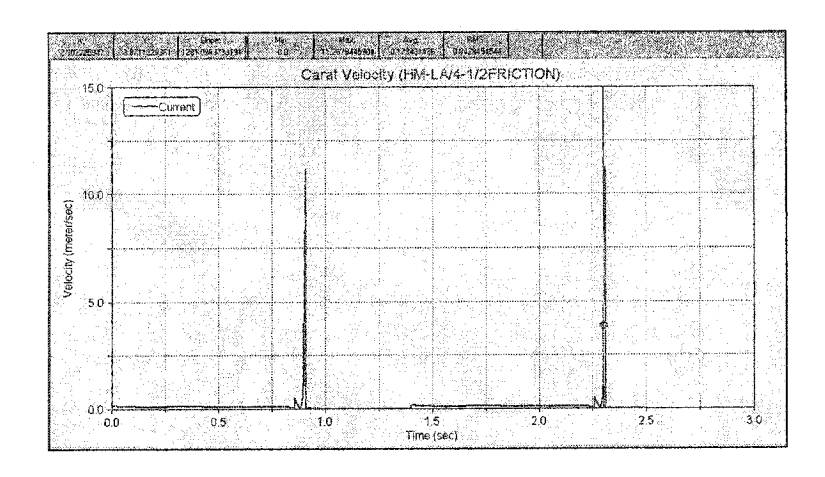


Figure 3.8: Speed at the impact: third simulation run.

As it can be seen from the figure 3.8, maximum speed at the impact was found to be equal to 11.26 m/sec from the simulation.

In all the conditions listed above, maximum speed at the impact was found when the target ball was placed near the tip of the caret for an uncompressed spring state as shown in the figure 3.9 for better visualization in the rendered mode. As it can be seen from the figure 3.9, virtual prototype is a mirror image of the physical prototype as shown in the figure 2.6.

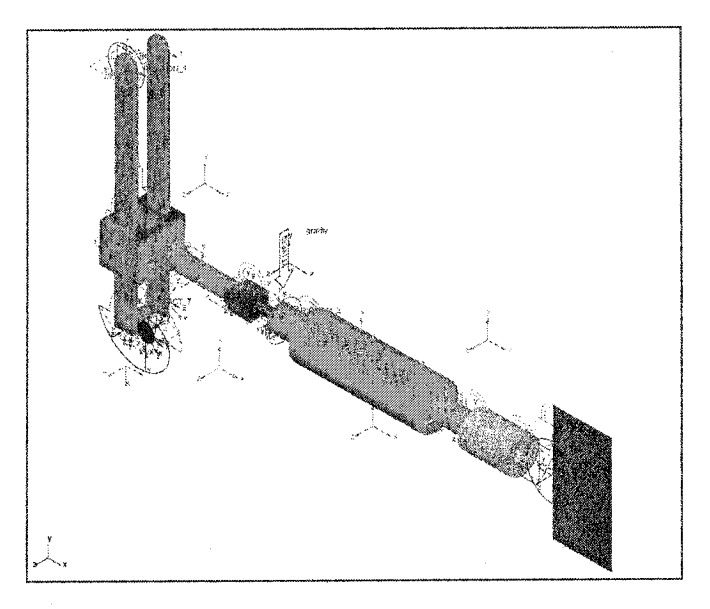


Figure 3.9: Posture for maximum speed at the impact: rendered mode.

- 3.3.3.5. Verification of the Virtual Model. The virtual model was compared with the theoretical analysis. Magnitude of the torque needed to compress the spring with a spring constant  $\kappa$  for a compression amplitude of x was set as a verification criteria because of the following reasons,
  - derivation for the torque calculation (eq. 4.14) involves force on the cam  $(F_c)$ , spring displacement (x), spring constant  $(\kappa)$ , ratio  $(\frac{r_1}{r})$  and a pre know parameter; radius of the cam  $(R_{cam})$ , which makes it a quite reasonable choice for the verification purposes,
  - a prim mover for coupling with the cam could be designed after knowing precisely the power needed to compress the strongest spring for the maximum compression amplitude, and
  - a computationally easy parameter to compare.

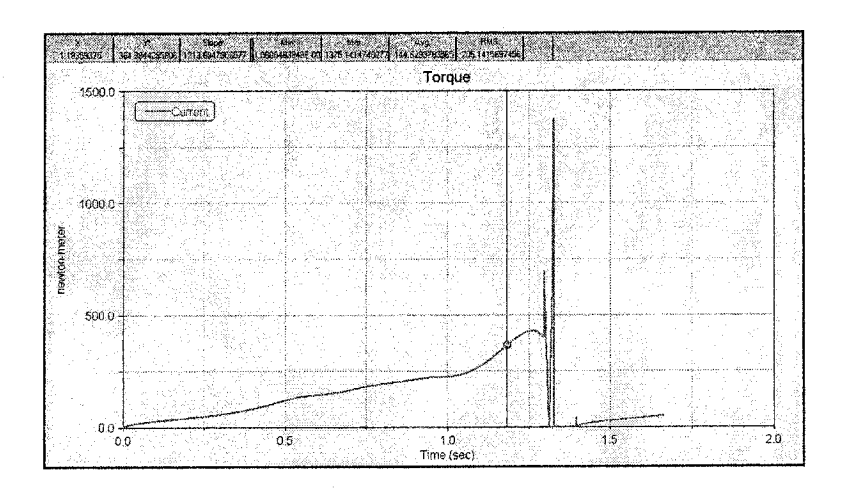


Figure 3.10: Torque requirement for compressing the spring.

From equation 3.14, the value of the torque needed to compress a spring with a spring constant equal to 124.717 N/mm compressed to 96.00 mm of amplitude can be calculated for  $r_1/r = 0.7185$  (from simulation) as,

$$T = \frac{r_1}{r}(\kappa x) \times R_{cam} = 0.7185 \times (124.717)(96) \times (152.4) = 1311.01 \ Nm$$
 (3.25)

As it can be seen from the figure 3.10, the maximum value of torque is  $1375.14 \ Nm$  from the simulation and  $1311.01 \ Nm$  from the theoretical calculations (equation 3.25).

Therefore, an error percentage in the virtual model can be calculated as,

$$\% \ error = \frac{T_{simulation} - T_{theoretical}}{T_{theoretical}} = \frac{1375.14 - 1311.01}{1311.01} = 4.89 \%$$
 (3.26)

An error of 4.89 % in the virtual model is quite reasonable after considering the fact that errors are almost inevitable during the building of virtual prototype model from a physical prototype.

**3.3.4.** Discussions. Virtual prototyping helped to know which variables are critical for the optimization. To define variables, we need to know which variables have an effect on the variable to be minimized. The objective was to minimize the volume of the moving components which is directly related to weight of the components.

Further, results from ADAMS simulations were used for determining variables for optimizing designs while using ANSYS for the finite element analysis purposes. These variables are:

Design Variables (DVs). Independent variables that directly effect the design objective. For the impact tester prototype, the width and height of the Lever arm and diameter of the other moving components are the DVs.

State Variables (SVs). Dependent variables that change as a result of changing the DVs. These variables are necessary to constrain the design. In this design problem, the SV is the maximum allowable stress in the components.

Objective Variable (OV). The objective variable is the one variable in the optimization that needs to be minimized. In this design problem, the volume of the moving components will be minimized in order to achieve maximum possible speed at the impact.

## CHAPTER 4

# Lever Arm Assembly Design Stages

The Lever arm assembly was designed in a logical design sequence in order to overcome the design problems faced during working with the previous Lever arm assembly of version II of the impact wear tester.

As mentioned earlier the basic objective behind designing the new Lever arm assembly was to reduce its weight, which has profound effect on speed at the impact.

The following sections and subsections explain the design stages involved in designing the Lever arm assembly for the *version III* (latest version) of the impact wear tester.

#### 4.1. Design of the Lever Arm Assembly

The following problems were encountered during working with the previous Lever arm assembly of version II of the impact wear tester, as shown in the figure 4.1,

- The assembly was very bulky (12.30 kgs).
- It had 18 parts, which is a very large number.
- It was hung at two pivot points. This kind of design increases friction.
- It was very difficult to adjust the spring compression amplitude by lowering and raising the coupling on the Lever arm.

New designs of the *Lever arm assembly* were proposed in order to remove aforementioned problems.

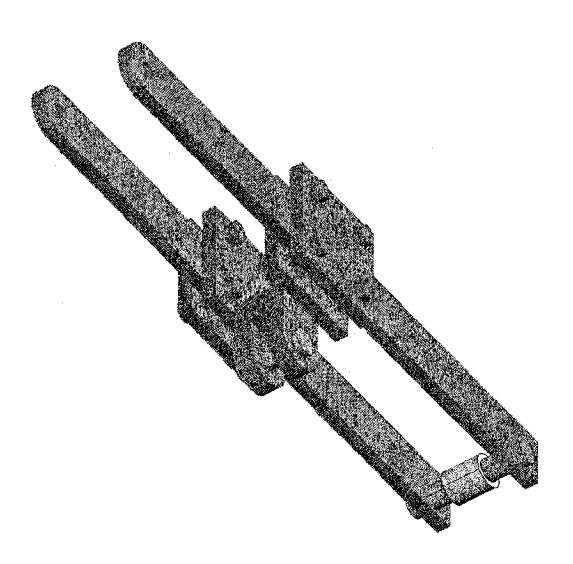


Figure 4.1: Previous Lever arm assembly.

#### 4.1.1. Design Stages.

- (i) In the first stage, different Lever arm assembly design concepts (figures 4.2(a) to 4.3), according to the requirements were proposed.
- (ii) In the second stage, material was selected and the maximum allowable design stress was calculated according to the design requirements.
- (iii) In the third stage, comprehensive theoretical analysis of the Lever arm was performed.
- (iv) In the fourth stage, the Lever arm was analyzed using ANSYS.
- (v) In the fifth stage, coupling assembly was analyzed using ANSYS, which includes design of two side brackets, which mirror each other in the geometry and a front part.
- (vi) Follower assembly was analyzed in the final stage of the Lever arm assembly design using ANSYS, which consists of designs of a follower cylindrical roller, a support cylinder or pin, and a support structure (main body).

### 4.2. First Design Stage: Evolutionary Design Ideas

The following figures show how the final design of the Lever arm assembly was reached after proposing successive improvements in the previous assembly designs.

#### 4.4.2 FIRST DESIGN STAGE: EVOLUTIONARY DESIGN IDEAS

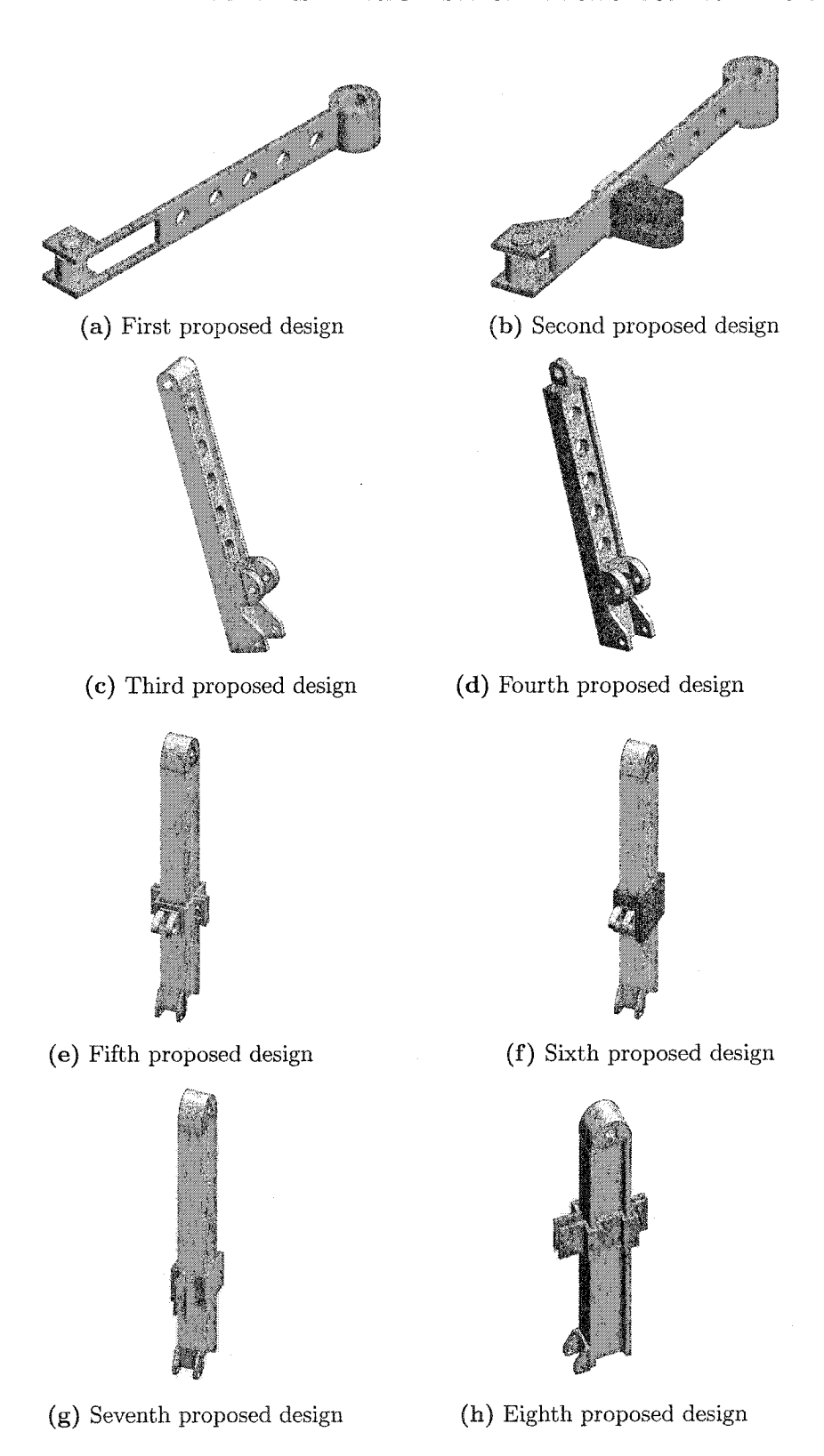


Figure 4.2: Evolutionary Lever arm assembly designs.

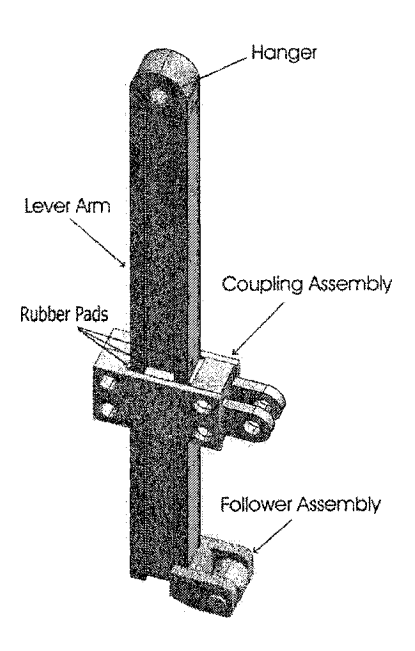


Figure 4.3: Lever arm assembly: final design.

As shown in the figure 4.3, the final design of the Lever arm assembly has the following advantages over the previous Lever arm assembly (figure 4.1),

- It has only 10 parts versus 18 parts in the previous version (figure 4.1).
- It hangs at only one pivot point, which offers less friction than the previous design (figure 4.1) during any movement.
- Very easy to change the position of coupling on the Lever arm for altering spring compression amplitude.
- Overall weight, if the same material is used, would be about 3.10 kg lighter than the previous Lever arm assembly design (figure 4.1).

# 4.3. Second Design Stage: Material Selection and Design Stress

It can be noted from the previous chapter, weight is a major consideration in improving the impactor mechanism. Due to this reason Titanium was chosen as a material for manufacturing Lever arm assembly components. Titanium alloys are very well known to have the highest strength to weight ratio among all the structural materials.

#### 4.4.3 SECOND DESIGN STAGE: MATERIAL SELECTION AND DESIGN STRESS

- **4.3.1. Material Selection.** Titanium ASTM Grade 5, Ti 6Al 4V (alpha-beta alloy) was chosen as the material to manufacture the Lever arm assembly because of the following reasons (Henry et al., 1995),
  - The most easily available and the most widely used titanium alloy.
  - It has very high strength and excellent *fatigue* properties.
  - The alloy is weldable.
  - It has very good mechanical properties up to 550°C.
  - Its intrinsic resistance to corrosion practically eliminates maintenance in most environments.

The tables 4.1, 4.2 and 4.3 show some properties of Ti - 6Al - 4V (ASTM Grade 5) used for improving knowledge and designing the components.

0	N	C	H	Fe	Al	$\mathbf{V}$	Residuals
0.20	0.05	0.08	0.015	0.40	5.5-6.75	3.5 - 4.5	0.4

Table 4.1: Chemical composition (weight %) (Henry et al., 1995).

Mechanical properties	Minimum values	Typical values
Yield Strength	825 MPa	910 MPa
Ultimate Strength	895 MPa	1000 MPa
Reduction in Area	20 %	
Hardness		330-390 HV
Modulus of elasticity		105 GPa

Table 4.2: Mechanical properties at room temperature (Henry et al., 1995).

Ti-6Al-4V (ASTM Grade 5) has a fatigue strength of 490 MPa for a smooth specimen  $(K_t=1)$  under rotating bending condition for stress that cause failure in  $10^7$  cycles (Henry et al., 1995). The table 4.3 shows some of the physical properties of Ti-6Al-4V (ASTM Grade 5).

Physical properties	Typical values
Melting point, $\pm 15^{\circ}$ C	$1650^{o}\mathrm{C}$
Density	$4.43 \; {\rm g/cm^3}$
Thermal conductivity	$6.6~\mathrm{W/mK}$
Specific heat	$0.57~\mathrm{J/gK}$
Poisson's ratio	0.30-0.33

Table 4.3: Physical properties at room temperature (Henry et al., 1995).

4.3.2. Design Stress. If a machine part is safe to transmit loads acting upon it, a permissible maximum stress must be established and used in the design. This is the allowable stress, the working, or preferably, the *design stress* (Baumeister et al., 1988). The design stress should not waste material, yet should be large enough to prevent failure in case loads exceed expected values, or other uncertainties react unfavorably.

The load on a member in the structure is based on the external loads applied to the whole structure, the reactions supporting the structure, and the geometry of the structure. Variations in external loads, reactions, and/or *geometry* result in variations of calculated load. Thus load, and therefore stress, is also a random variable with an expected mean value and a standard deviation (Anderson, 2001).

Cyclic loading of a material can lead to a fatigue failure over time. Impact (shock) loading produces very high transient stresses which can precipitate failure.

Modern engineering is based on predicting the performance of structures and machines before they are actually built. The transition from engineering model to reality is usually facilitated by including a factor of safety in the design to accommodate uncertainty in material properties and the design process, the consequences of failure, risk to people, and degree of characterization of and control over the service environment.

The design stress is determined by dividing the applicable material property—yield strength, ultimate strength, fatigue strength—by a factor of safety. The factor should be selected only after all *uncertainties* have been thoroughly considered (Anderson, 2001).

The safety factor for structural systems, proposed Philon of Byzantium (3rd century BC) (Shigley and Mischke, 2001), is defined as follows

$$N = \frac{capacity}{load} = \frac{strength}{stress} > 1 \tag{4.1}$$

Safety factor is a simple ratio that is intended to be greater than one. That is, capacity must be greater than load and strength must be greater than stress. A large safety factor usually means a safer design; however, more material is used in the design with a corresponding increase in cost and weight. Therein lies one of the fundamental trade-offs in engineering design—cost vs. safety.

4.3.2.1. Reliability. Equation 4.1 is called the central safety factor because it is based on mean values of capacity, strength, load, and stress. Suppose the loading on the system were actually greater than anticipated in the design and the strength of the system were less than expected, then the probability of failure of that system would be greater than expected. Figure 4.4 depicts normal probability distributions of both stress and strength which overlap. The region of overlap is also the region of greatest probability of system failure.

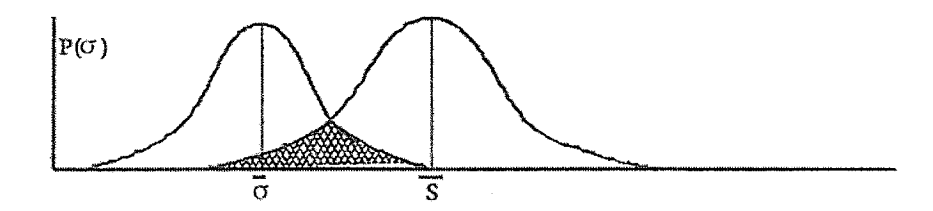


Figure 4.4: The probability distributions of stress and strength showing substantial overlap (Juvinall and Marshek, 1991).

Based on the figure 4.4, we may modify the safety factor equation (4.1) to account for this overlap between stress and strength (Shigley and Mischke, 1989), (Shigley, 1972) as follows

$$N_R = N\left(\frac{1 - a\gamma_S}{1 + a\gamma_\sigma}\right) > 1 \tag{4.2}$$

where,

 $N_R$  = safety factor based on reliability,

N = central safety factor based on mean or expected values (eq. 4.1),

a=number of standard deviations to produce the desired confidence level,

 $\gamma_S$ = coefficient of variation of the strength value (published)= 5% approx (Henry et al., 1995),

 $\gamma_{\sigma}$  = coefficient of variation of the stress value (estimated) = 10% approx.

a:	0	1.65	2.33	3	3.08	3.62	4.42	4.89
Reliability %:	50	95	99	99.87	99.9	99.99	99.999	99.9999
Failure Rate %:	50	5	1	0.13	$1/10^{3}$	$1/10^4$	$1/10^{5}$	$1/10^{6}$

Table 4.4: Standard deviation and reliability.

 $N_R$  can be calculated as (with a reliability of 99.87%):

$$N_R = 3\left(\frac{1 - 3.0 \times 0.05}{1 + 3.0 \times 0.1}\right) = 1.96 \approx 2.0$$
 (4.3)

Notice that eq. 4.2 is a relatively simple modification of the definition of central safety factor (eq. 4.1) that compares the highest expected stress against the lowest expected strength based on the specified level of reliability.

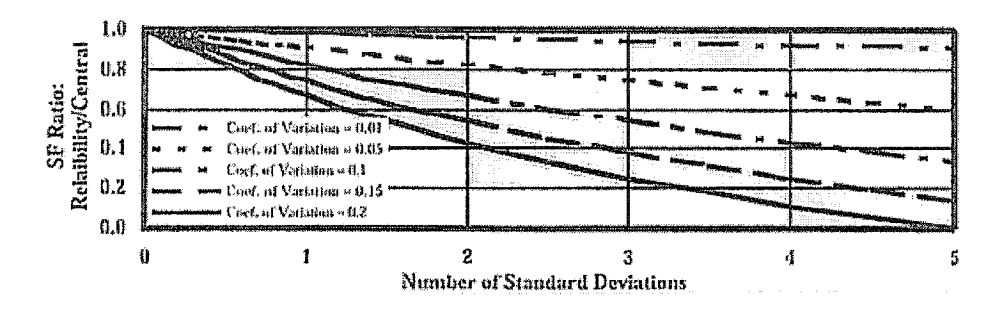


Figure 4.5: Ratio of the reliability safety factor to the central safety factor (Anderson, 2001).

4.3.2.2. The Visodic Safety Factor Model. Joseph P. Visodic developed and published recommendations for minimum central safety factor values in 1948 which were based on cumulative experience (Shigley and Mischke, 2001; Burr and Cheatham, 1995; Juvinall and Marshek, 1991; Juvinall, 1983). These are presented in the table 4.5. Safety factors for ductile materials are based on yield strength. Safety factors for brittle materials are based on ultimate strength and are twice the recommended values for ductile materials. Safety factors for primarily cyclic loading are based on endurance limit. Impact loads require a safety factor of at least 2 multiplied by an impact factor, usually in the range of 1.1 to 2 (Shigley and Mischke, 2001).

Safety	Knowledge	Knowledge	Knowledge	Knowledge
Factor	of Loads	of Stress	of Material	of Environment
1.2 - 1.5	Accurate	Accurate	Well Known	Controllable
1.5 - 2.0	Good	$\operatorname{Good}$	Well Known	Constant
2.0-2.5	Good	Good	Average	Ordinary
2.5 - 3.0	Average	Average	Less Tried	Ordinary
3.0-4.0	Average	Average	Untried	Ordinary
3.0-4.0	Uncertain	Uncertain	Better Known	Uncertain

Table 4.5: Recommended central FOS for ductile materials based on yield strength (Shigley and Mischke, 2001).

As it can be seen from the table 4.5, the central safety factor for a ductile material based on yield strength with average knowledge of load and stress with well known knowledge of material properties and ordinary environment condition is between 2.5 and 3.0. Which is why the chosen value of FOS as 3.0 is a reasonable approximation of it.

4.3.2.3. The Norton Safety Model. Norton (1996) stated "Clearly, where human safety is involved, high values of (safety factor) are justified." His overall safety factor value is a combination of a safety factor based on material properties, one based on engineering model accuracy, and one based on expected service environment, as follows,

$$N_{ductile} \ge max(N_1, N_2, N_3);$$
 based on the yield strength (4.4)

$$N_{brittle} \ge 2[max(N_1, N_2, N_3)];$$
 based on ultimate strength (4.5)

where,  $N_1, N_2$ , and  $N_3$  are selected from the table 4.6.

Safety factors for ductile materials are based on yield strength, while those for brittle materials are based on ultimate strength. Table 4.6 shows recommended values of  $N_1, N_2$ , and  $N_3$ .

The chosen values of  $N_1$ ,  $N_2$ , and  $N_3$  are as followed,

 $N_1 = 2.0$  for good approximation of the material properties.

 $N_2 = 3.0$  for fair approximation of the stress/load model accuracy.

 $N_3 = 2.0$  for controlled, room-temperature of service environment.

Safety	$\mathbf{N}_1$	$\mathbf{N}_2$	$N_3$	
Factor	Material Properties	Stress/Load	Service	
Value	(from tests)	Model Accuracy	Environment	
1.3	Well known/	Confirmed	Same as material	
	characterized	by testing	test conditions	
2	Good approximation	Good approximation	Controlled	
3	Fair approximation	Fair approximation	Moderate	
5+	Crude approximation	Crude approximation	Extreme	

Table 4.6: Recommended central FOS for ductile materials based on yield strength (Norton, 1996).

From the equation 4.4 the value of  $N_{ductile}$  can be chosen as,

 $N_{ductile} \ge max(2.0, 3.0, 2.0);$  based on yield strength

 $N_{ductile} \ge 3.0$ 

4.3.2.4. The Pugsley Safety Factor Model. Pugsley (1966) recommended that safety factors be determined as the product of two factors

$$N = N_1 N_2 \tag{4.6}$$

where,

 $N_1 = f(A, B, C)$ —from the table 4.7,

 $N_2 = f(D, E)$ —from the table 4.8,

A- is the quality of materials, workmanship, maintenance, and inspection,

B- is control over applied loads,

C- is accuracy of stress analysis, experimental data, or experience with similar parts

D- is danger to people, and

E- is economic impact.

The value of  $N_1$  as a function of A, B, and C can be chosen as 2.30 for A=G, B=F and C=F from the table 4.7.

And in the similar fashion the value of  $N_2$  as a function of D and E can be chosen as 1.30 for D=S and E=S from the Table 4.8.

Therefore, the value of FOS can be calculated as,

$$N = 2.30 \times 1.30 = 2.99 \approx 3.0 \tag{4.7}$$

Characteristic			B =			
		$\prod$	VG	G	F	P
A = VG	C = VG		1.10	1.30	1.50	1.70
	C = G		1.20	1.45	1.70	1.95
	C = F		1.30	1.60	1.90	2.20
	C = P		1.40	1.75	2.10	2.45
A = G	C = VG		1.30	1.55	1.80	2.05
	C = G		1.45	1.75	2.05	2.35
	C = F		1.60	1.95	2.30	2.65
	C = P		1.75	2.15	2.55	2.95
A = F	C = VG		1.50	1.70	1.90	2.10
	C = G		1.80	2.05	2.30	2.55
	C = F		2.10	2.40	2.70	3.00
	C = P		2.40	2.75	3.10	3.45
A = P	C = VG		1.70	1.95	2.20	2.45
	C = G		2.15	2.35	2.65	2.95
	C = F		2.40	2.75	3.10	3.45
	C = P		2.75	3.15	3.55	3.95

**Table 4.7:** Values for safety factor characteristics (VG = Very Good, G = Good, F = Fair, P = Poor).

Characteristic	E =			
	NS	S	VS	
D = NS	1.0	1.0	1.2	
D = S	1.2	1.3	1.4	
D = VS	1.4	1.5	1.6	

Table 4.8: Values for safety factor characteristics (VS = Very Serious, S = Serious, NS = Not Serious).

4.3.2.5. Discussions. The value of a central safety factor (equation 4.1) should not be less than two (2) for most structural applications and should routinely be set at three (3). Uncertainty in loading, uncertainty in material properties, foreseeable abuse, and challenging service environments demand higher values of the safety factor. A long service life also requires a larger value of safety factor. High reliability applications require systems with a larger central safety factor value.

The reliability safety factor (equation 4.2) accommodates lower values than the central safety factor (equation 4.1) for the same probability of failure. Shigley (1972) feels that

given well known values and a reasonable reliability level (95% or higher) safety factor values between 1.3 and 2.0 are adequate. Again, lower safety factor values require physical testing, a predictable service environment, and periodic inspection and maintenance.

Service loads due to expected normal use and foreseeable abuse are usually difficult to establish. Well characterized loads justify a lower minimum safety factor value, while uncertain loads require a larger value.

Cyclic loading induces fatigue failure in structural components. The safety factor for primarily cyclic loading should be based on the *endurance limit* rather than on yield or tensile strength. Well characterized cyclic loads justify a lower minimum safety factor value, while uncertain loads should have a larger value (Rice et al., 1988).

The consequences of system failure must also be considered in the selection of a minimum safety factor value. If human life and health are at risk and/or potential property damage caused by system failure is substantial, then a higher minimum safety factor value is required. These are the situations in which failure precipitates liability litigation and therefore a higher safety factor should be viewed as relatively cheap liability insurance.

Case	Reliability	Visodic	Norton	Pugsley
Design of the Lever arm assembly	2.0	2.5-3.0	3.0	3.0

Table 4.9: A comparison of safety factor models.

After taking consideration of uncertainties and assumptions associated with the overall reliability of the design; a value of three (3) as a FOS can reasonably be assumed. From equation 4.1, the maximum allowable design stress can be calculated as,

$$Design Stress = \frac{490}{3} = 163.33 MPa \tag{4.8}$$

where fatigue or endurance strength of the Titanium Grade 5, Ti - 6Al - 4V (alpha-beta alloy) is 490.0 MPa (Henry et al., 1995).

As on results, the use of Titanium ASTM Grade 5 further lightens the weight of Lever arm assembly to approximately 5.0 kg.

# Third Design Stage: Theoretical Analysis of the Lever Arm

As mentioned earlier, the design shown in the figure 4.3 was selected as the final design of the Lever arm assembly. In this figure, the Lever arm is an I cross section beam, loaded perpendicular to its side flanges. Primarily in this chapter *theoretical* analysis of the I cross section beams is explained, which is crucial for the design of Lever arm.

As shown in the figure 4.3, the Lever arm assembly incorporates designs of four components, namely Lever arm, which is basically an I beam, hanger (brass bushing), coupling assembly and follower assembly. The hanger (brass bushing) was designed along with the Lever arm, because ANSYS (FEA) simulates beams with any number of degrees of freedom (DOFs) at any point on the beam.

The hole diameter of the hanger was constrained by the diameter of hanger hole previously drilled in the green stationery structure (figure 2.6), which was 15.88m or 5/8", which is why the Lever arm's hanger hole diameter has been chosen to be equal to 15.88mm or 5/8".

#### 5.1. Plastic Design

Early effort in stress analysis as based on limit loads, that is, a load which stresses a member "wholly" to the yield strength. Euler's famous column paper ("Sur la Force des Colonnes," Academie des Science de Berlin, 1757) deals with the column problem this way

(Baumeister et al., 1988). More recently, the concept of limit loads, referred to as *limit*, or plastic design has found strong application in the design of certain structures (Baumeister et al., 1988). The theory presupposes a ductile material, absence os stress raisers, and fabrication free of embrittlement. Local load overstress is allowed, provided the structure does not deform appreciably.

To visualize the limit-load approach, consider a simple beam of uniform section subjected to a concentrated load of midspan, as depicted in the figure 5.1. According to elastic theory, the outermost fiber on each side and at midspan, the section of maximum bending moment, will first reach the yield-strength value. Across the depth of the beam, the stress distribution will follow the triangular shape, becoming zero at the neutral axis. If the material is ductile, the stress in the outermost fiber will remain at the yield value until every other fiber reaches the same value as the load increases. Thus the stress distribution assumes the rectangular pattern before the plastic hinge forms and failure ensues.

The problem is that of finding the final limit load. Elastic-flexure theory gives the final limit load—triangular distribution as,

$$F_y = \frac{2S_y bh^2}{3l} \tag{5.1}$$

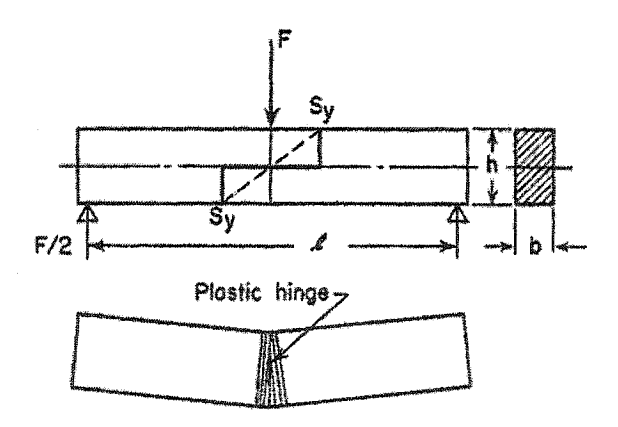


Figure 5.1: A centrally loaded beam of uniform section (Baumeister et al., 1988).

For the rectangular stress distribution, the limit load becomes

$$F_L = \frac{S_y bh^2}{l} \tag{5.2}$$

The ratio  $F_L/F_y = 1.50$ —an increase of 50 percent in load capability. The ratio  $F_L/F_y$  has been named shape factor. Figure 5.2 shows shape factors for a typical I-section. The shape factor may also be determined by dividing the first moment of area about the neutral axis by the section modulus.

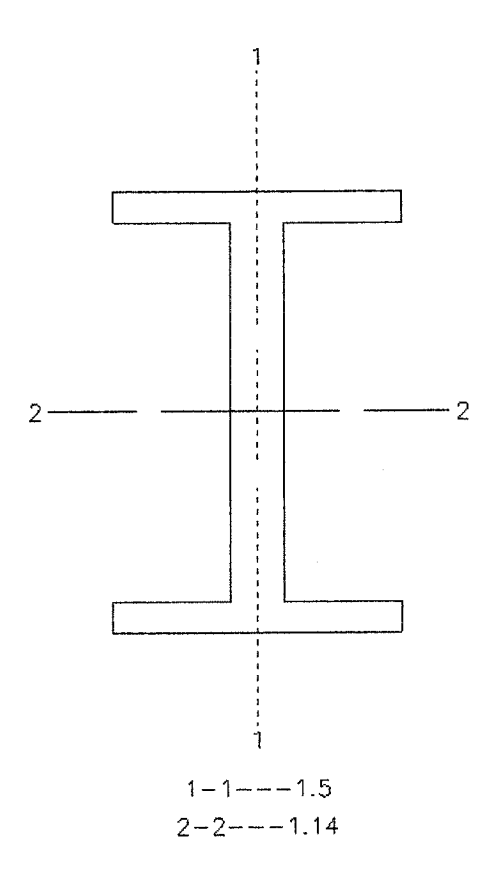


Figure 5.2: Shape factors for I-section under different loading conditions.

#### 5.2. Analysis of Beams

A simple beam rests on supports at its ends, which permit rotation. When computing reactions and moments, distributed loads may be replaced by their resultant acting at the center of gravity of the distribution-load area.

In order to understand behavior of the structural beams under various loading conditions, a thorough analysis of the beams was performed under the following subsection headings.

5.2.1. Theory of Flexure. A bent beam is shown in the figure 5.3. The concave side is in compression and the convex side in tension. These are divided by the *neutral plane* of zero stress A'B'BA. The intersection of the neutral plane with the face of the beam is in the *neutral line or elastic curve* AB. The intersection of the neutral plane with the cross section is the *neutral axis* NN'.

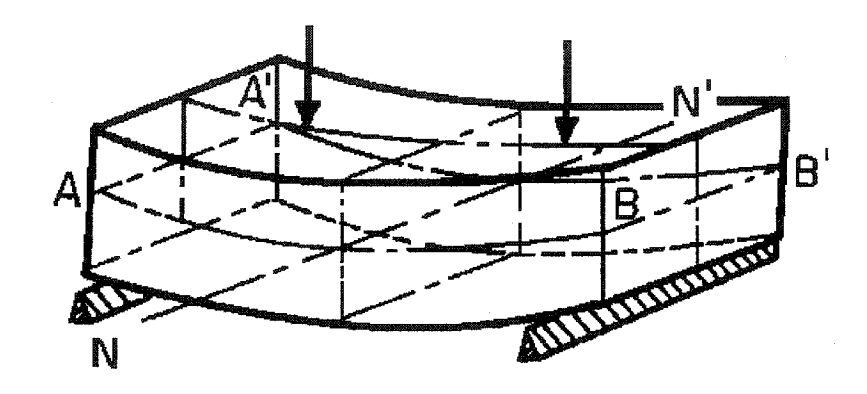


Figure 5.3: A beam under bending stress (Baumeister et al., 1988).

It is assumed that a beam is *prismatic*, of a length at least 10 times the depth, and that the external forces are all at right angle to the axis of the beam and in a plane of symmetry, and that flexure is slight. Other assumptions are: (1) That the material is homogenous, and obeys Hook's law. (2) That the *stresses are in elastic limit*. (3) That every layer of material is free to expand and contract longitudinally and laterally under stress as if separate from other layers. (4) That the tensile and compressive moduli of elasticity are equal. (5) That the cross section remain a plane surface.

It follows then that, (1) The internal forces are in horizontal balance. (2) The neutral axis contains the center of gravity of the cross section, when there is no resultant axis stress. (3) The stress intensity varies directly with the distance from the neutral axis.

The moment of the elastic forces about the neutral axis, i.e., the *stress moment* or *moment of resistance*, is

$$M_b = SI/c (5.3)$$

where S is an elastic unit stress at outer fiber whose distance from the neutral axis is c; and I is the rectangular moment of inertia about the neutral axis. This formula is for the strength of beams.

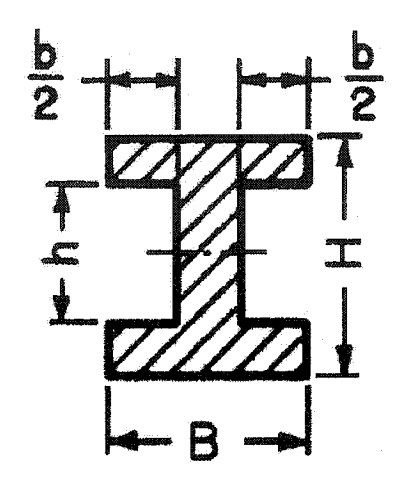


Figure 5.4: Cross sectional dimensions of a typical I beam.

For an I-shaped cross section (figure 5.4) beams,

$$I = \frac{BH^3 - bh^3}{12} \tag{5.4}$$

$$c = \frac{H}{2} \tag{5.5}$$

and the  $radius\ of\ gyration$ 

$$k = \sqrt{I/A} = \sqrt{\frac{BH^3 - bh^3}{12(BH - bh)}}$$
 (5.6)

The elastic strength of beam section varies as follows, (1) for equal cross section, directly as the strength of material; (2) if span varies, then for equal cross-section, and material, inversely as the span.

The term section modulus is given to the value of I/c, where c is the distance to the fiber carrying greatest stress. Therefore, section modulus can be expressed as,

$$\frac{I}{c} = \frac{BH^3 - bh^3}{6H} \tag{5.7}$$

5.2.2. Internal Moment beyond the Elastic Limit. If, the expression  $M_b = SI/c$  is used for stresses above the elastic limit, in which case S becomes an experimental coefficient  $S_R$ , the *modulus of rupture*, and the formula is empirical. The true relation is obtained by applying to the cross section a stress-strain diagram from a tension and compression test, as in the figure 5.5.

Figure 5.5 shows the side of a beam of depth d under flexure beyond its elastic limit; line 1-1 shows the distorted cross section; line 3-3, the usual rectilinear relation of stress to strain; and line 2-2, an actual stress-strain diagram, applied to the cross section of the beam, compression above and tension belove. The neutral axis is then below the gravity axis.

The outer material may be expected to develop greater ultimate strength than in simple stress, on account of the reinforcing action of material nearer the neutral axis that is not yet overstrained. This leads to an equalization of stress over the cross section.

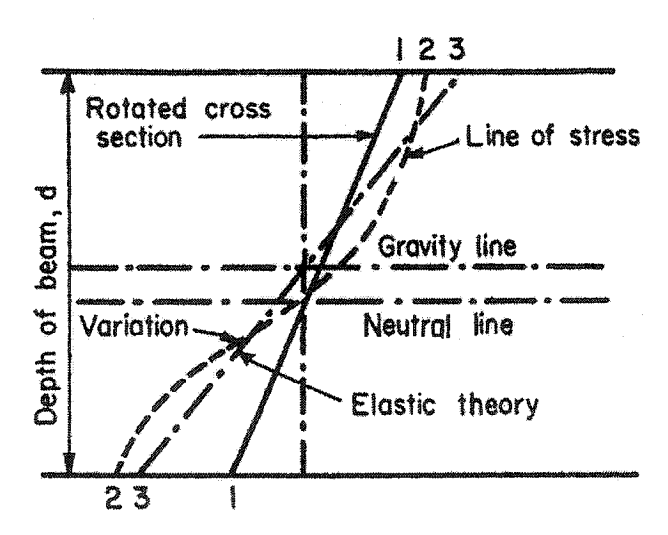


Figure 5.5: A flexure beyond its elastic limit (Baumeister et al., 1988).

In the case of Titanium I beams, failure begins practically when the elastic limit in the compression flange is reached.

Wide plates will not expand and contract freely, and the value of E will be increased on account of side constraint. As a consequence of lateral contraction of the fiber at the tension side of a beam and lateral swelling of fiber at the compression side, the cross section becomes distorted to a trapezoidal shape, and the neutral axis is at the center of the gravity of the trapezoid. Strictly, this shape is one with a curved perimeter, the radius being  $r/\mu_p$ , where r is the radius of the neutral line of the beam, and  $\mu_p$  is the Poisson's ratio.

**5.2.3. Deflection of Beams.** When a beam is subjected to bending, the fibers on one side elongate, while the fibers on the other side shortens (figure 5.6). These changes in length cause the beam to deflect. All points in the beam except those directly over the support fall below their original position, as shown in the figures 5.3 and 5.6.

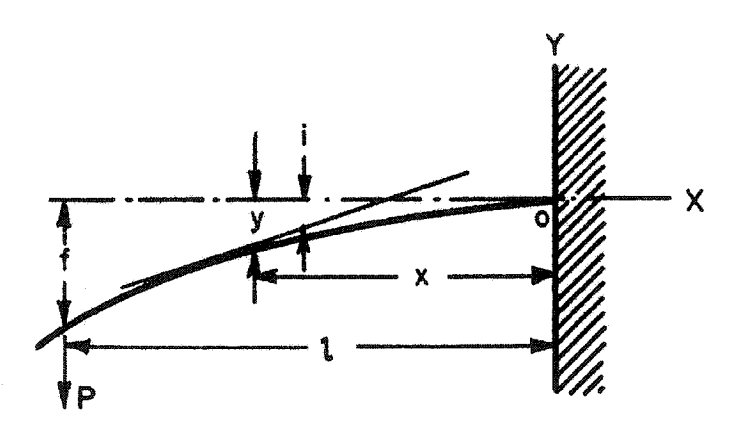


Figure 5.6: A beam under bending (Baumeister et al., 1988).

The *elastic curve* is the curve taken by the neutral axis. The radius of curvature at any point is

$$r = E_y I/M_b \tag{5.8}$$

A beam bent to a circular curve of constant radius has a constant bending moment.

Replacing r in the equation by its approximate geometrical value,  $1/r = d^2y/dx^2$ , the fundamental equation from which the elastic curve of a bent beam can be developed and the deflection of any beam obtained is,

$$M_b = E_y I d^2 y / dx^2 \qquad \text{approx} \tag{5.9}$$

Substituting the value of  $M_b$ , in terms of x, and integrating once, gives the slope of the tangent to the elastic curve of the beam at point x;

$$\tan i = dy/dx = \int_0^x M_b \ dx/E_y I \tag{5.10}$$

Since i is usually small, therefore we can write,  $\tan i = i$ , expressed in radians. A second integration gives the vertical deflection of any point of the elastic curve from its original position.

Deflection in general, f, may be expressed by the equation

$$f = PL^3/m_c E_v I (5.11)$$

where  $m_c$  is a coefficient. For an I shaped section, supported at both the ends and loaded in the middle of the span, the value of f (in mm) is,

$$f = \frac{PL^3}{48E_y I} (5.12)$$

where,

L = distance between supports, mm

P = total working load, N.

Since I varies as the cube of the depth, the *stiffness*, or inverse deflection, of various beams varies, other factors remaining constant, inversely as the load, inversely as the cube of span, and directly as the cube of the depth. This deflection is due to bending moment only.

When the bending beams involves transverse shearing stresses which cause *shearing* strains and thus add to the total deflection. These strains may affect substantially the strength as well as the deflection of beams. When deflection due to transverse shear is to be accounted for, the differential equation of the elastic curve takes the form (Baumeister et al., 1988),

$$E_y I \frac{d^2 y}{dx^2} = E_y I \left( \frac{d^2 y_b}{dx^2} + \frac{d^2 y_s}{dx^2} \right) = M_b - \frac{\mathbf{k} E_y I}{AG} \times \frac{d^2 M_b}{dx^2}$$
 (5.13)

where  $\mathbf{k}$  is a factor dependent upon the beam cross section. Sergius Sergev, in "The Effect of Shearing Forces on the Deflection and Strength of Beams" (*Univ. Wash. Eng. Exp. Stn. Bull.* 114) gives  $\mathbf{k} = 2.4$  for I beams (Baumeister et al., 1988).

5.2.4. Relation between Deflection and Stress. Combine the formula  $M_b = SI/c = PL/n$ , where n is constant, P=load, and L=span, with formula  $f = PL^3/m_cE_yI$ , where  $m_c$  is a constant. Then

$$f_{max} = C'' S_{max} L^2 / E_u c \tag{5.14}$$

where C'' is a new constant  $=n/m_c$ . Other factors remaining the same, the deflection varies directly as the stress and inversely as  $E_y$ . If the span is constant, a shallow beam will submit to greater deformation than a deeper beam without exceeding a safe stress. If depth is constant, a beam of double span will attain a given deflection with only one-quarter the stress (Baumeister et al., 1988).

5.2.4.1. Graphical Relations. Referring to the figure 5.7, the shear V acting at any section is equal to the total load on the right of the section, or

$$V = \int w \, dx \tag{5.15}$$

Since w dx is the product of w, a loading intensity (which is expressed as a vertical height in the load diagram), by dx, an elementary length along the horizontal, evidently w dx is the area of a small vertical strip of the load diagram (Baumeister et al., 1988). In order to obtain the shear in any section mn, find the area of the load diagram up to the section, and draw a second diagram called the shear diagram, any ordinate of which is proportional to the shear, or to the area in the load diagram to the right of mn. Since  $V = dM_b/dx$ ,

$$\int V \, dx = M_b \tag{5.16}$$

By similar reasoning, a moment diagram may be drawn, such that the ordinate at any point is proportional to the area of the shear diagram to the right of that point. Since  $M_b = E_y I \ d^2 f/dx^2$ ,

$$\int M_b \, dx = E_y I[df/dx + C] = E_y I(i+C) \tag{5.17}$$

if I is constant. Here C is a constant of integration. Thus i, the slope or grade of the elastic curve at any point, is proportional to the area of the moment diagram  $\int M_b dx$  up to that point.

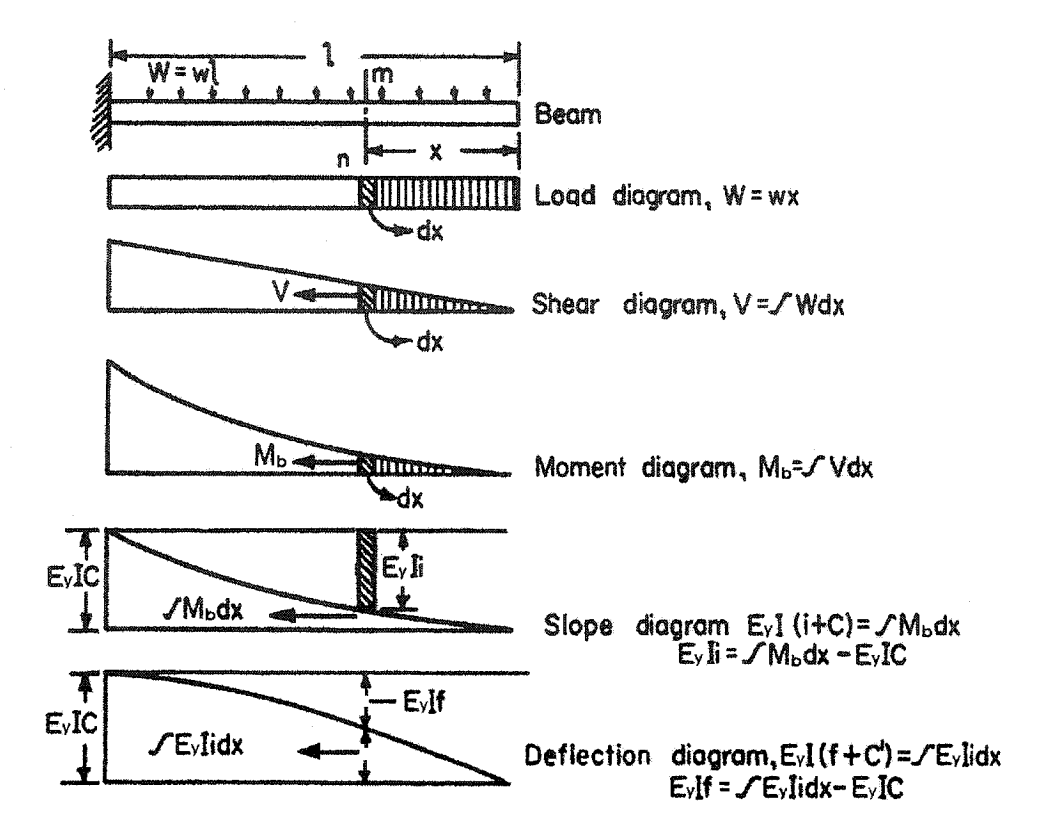


Figure 5.7: Characteristic diagrams of a beam under loading (Baumeister et al., 1988).

Thus, the five curves of load, shear, moment, slope, and deflection are so related that each curve is derived from the previous one by a process of *graphical integration*, and with proper regard to scales the deflection is thereby obtained.

The vertical distance from any point A (figure 5.8) on the elastic curve of a beam to the tangent at any other point equals the moment of the area of the  $M_b/E_yI$  diagram from A to B about A.

From the figure 5.8, the deflections of points B and D are

$$y_B = -t_{AB} = \text{moment area } \frac{M_b}{E_y I} \Big|_A^B A = -\frac{1}{E_y I} \times \frac{PL}{4} \times \frac{L}{4} \times L3 = -\frac{PL^3}{48E_y I}$$
 (5.18)

$$\theta_C = \text{area} \frac{M_b}{E_u I} \bigg|_E^C = \frac{1}{E_u I} \times \frac{PL}{4} \times \frac{L}{4} = \frac{PL^2}{16E_u I}$$
 (5.19)

$$y_D = -(\theta_C \times \frac{L}{4} - t_{DC}) = -\frac{PL^2}{16E_yI} \times \frac{L}{4} + \frac{1}{E_yI} \times \frac{PL}{8} \times \frac{L}{8} \times \frac{L}{12} = -\frac{11PL^3}{768E_yI}$$
 (5.20)

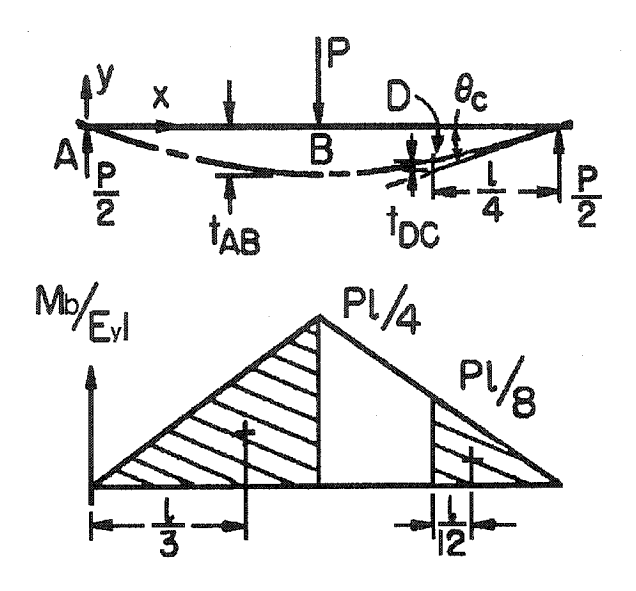


Figure 5.8: The elastic curve of a beam.

**5.2.5.** Resilience of Beams. The external work of a load gradually applied to a beam, and which increase from zero to P, is 1/2Pf and equals the resilience U (Baumeister et al., 1988). But, from the formulas P = nSI/cl and  $f = nSl^2/cm_cE_y$ , where n and  $m_c$  are constant that depend upon loading and supports, S= fiber stress, c= distance from neutral axis to outer fiber, and l= length of span. Substitute for P and f, and,

$$U = \frac{n^2}{m_c} \left(\frac{k}{c}\right)^2 \frac{S^2 V}{2E_y} \tag{5.21}$$

The resilience of beams of similar cross section at a given stress is proportional to their volume. The *internal resilience*, or the elastic deformation energy in the material of a beam in a length x is dU, and,

$$U = 1/2 \left( \int M_b^2 dx \right) / E_y I = 1/2 \int M_b di$$
 (5.22)

where, di is the angle between the tangents to the elastic curve at the ends of dx.

# Design of the Lever Arm Assembly Components by FEA

In order to design the Lever arm assembly components precisely, in the later stages of this assembly design, computational finite element analyses (FEA) were used. ANSYS 7.0 (2002) was used comprehensively for this purpose.

#### 6.1. Finite Element Analysis

ANSYS is a finite element modelling and analysis tool. It can be used to analyze complex problems in mechanical structures, thermal processes, computational fluid dynamics, magnetics, electrical fields, just to mention some of its applications. ANSYS provides a rich graphics capability that can be used to display results of analysis on a high-resolution graphics workstation (ANSYS 7.0 Help, 2002).

- **6.1.1.** Structural Analysis. Structural analysis is probably the most common application of the finite element method. The term structural (or structure) implies not only civil engineering structures such as bridges and buildings, but also naval, aeronautical, and mechanical structures such as ship hulls, aircraft bodies, and machine housings, as well as mechanical components such as pistons, machine parts, and tools.
- 6.1.1.1. Static Analysis. A static analysis calculates the effects of steady loading conditions on a structure, while ignoring inertia and damping effects, such as those caused by time-varying loads.

Static analysis is used to determine the displacements, stresses, strains, and forces in structures or components caused by loads that do not induce significant inertia and damping effects. Steady loading and response conditions are assumed; that is, the loads and the structure's response are assumed to vary slowly with respect to time (ANSYS 7.0 Help, 2002).

6.1.1.2. Nonlinear Static Analysis. Nonlinear structural behavior arises from a number of causes, which can be grouped into these principal categories: changing status, geometric nonlinearities, and material nonlinearities.

If a structure experiences large deformations, its changing geometric configuration can cause the structure to respond nonlinearly. Geometric nonlinearity is characterized by "large" displacements and/or rotations.

Nonlinear stress-strain relationships are a common cause of nonlinear structural behavior. Many factors can influence a material's stress-strain properties, including load history (as in elastoplastic response), environmental conditions (such as temperature), and the amount of time that a load is applied (as in creep response) (Moaveni, 1999). In the *Lever arm's* structural analysis geometric and material nonlinearities can be neglected because of small displacement and isotropic linear elastic material (Ti-6Al-4V, ASTM Grade 5).

ANSYS employs the "Newton-Raphson" approach to solve nonlinear problems. In this approach, the load is subdivided into a series of load increments. The load increments can be applied over several load steps. The Newton-Raphson Approach illustrates the use of Newton-Raphson equilibrium iterations in a single DOF nonlinear analysis (ANSYS 7.0 Help, 2002).

#### 6.2. Fourth Design Stage: Lever Arm Design

In the fourth stage of the Lever arm assembly design, the *Lever arm* was designed because design of the coupling and follower assemblies were dependent on its design. The *Lever arm* was designed using computational finite element analysis (FEA).

**6.2.1.** A Model of the Problem. In the figure 1.8, the Lever arm was suspended at one end point and driven by the cam at the other end point, while spring force acted on the beam span. A finite element analysis (FEA) model was built on the assumption that

the maximum force at the middle of the beam span would produce maximum deflection, which simulated the toughest physical condition scenario (figure 6.1).

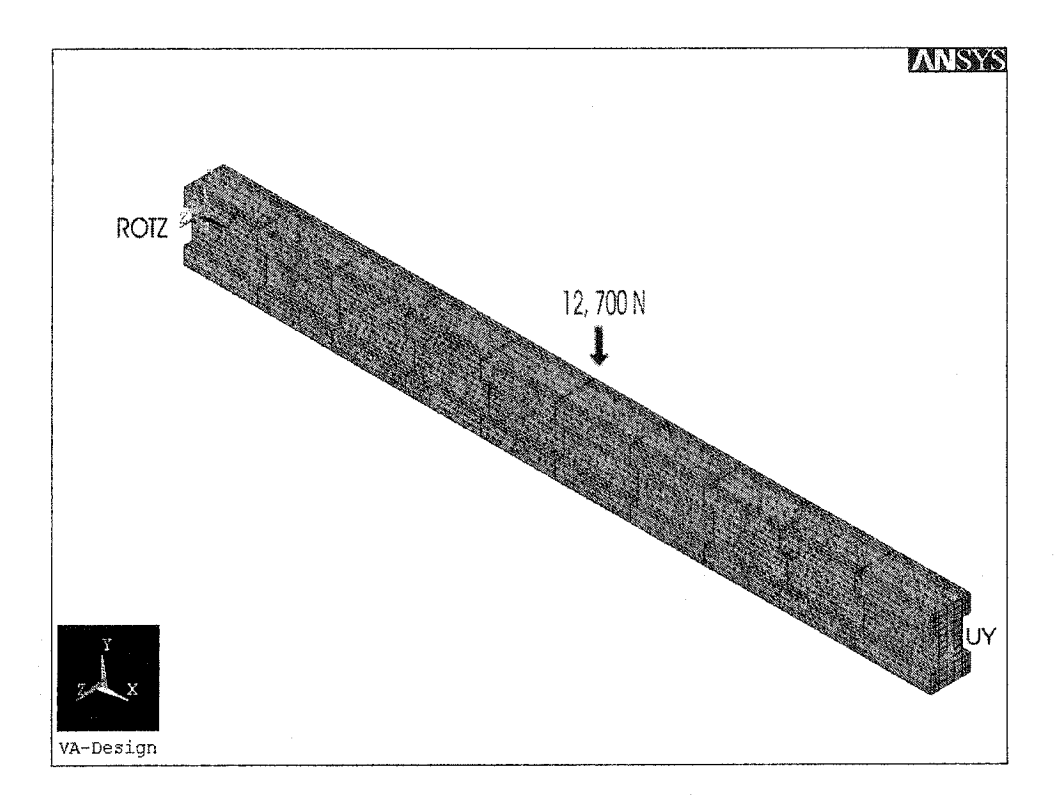


Figure 6.1: A centrally loaded I beam.

In the ADAMS simulations, the strongest spring was compressed to 96.00 mm (figure 3.6) of amplitude but for the finite element analysis, spring force was calculated for the 101.50 mm of compression amplitude in order to generate more confidence in the design because it is always advisable for a new designer to either use a fraction (90%-95%) of a material's fatigue strength or use a greater value of the pressures or forces applied on the components (Adams and Askenazi, 1999).

As shown in the figure 6.1, a force of 12, 700 N is acting at the middle of the I beam span in the -Y-axis direction, which represents a spring force exerted by the strongest spring with  $\kappa$ =124.717 N/mm (Producto, 1996), when compressed to 101.50 mm of the compression amplitude. In the figure 6.1, **ROTZ** is the rotation about Z-axis and **UY** is the reaction force in the +Y-axis direction at their respective beam ends.

**6.2.2.** Design Optimization: Lever Arm. Design optimization is a technique that seeks to determine an optimum design. "Optimum design" means one that meets all specified requirements but with a minimum expense of certain factors such as weight, surface area, volume, stress, cost, etc. In other words, the optimum design is usually one that is as effective as possible.

As mentioned earlier, the Lever arm basically is an I beam, which suspends about the pivot point  $O_0$  (figure 3.2) at one end and attached to the follower at the other remaining end (figure 4.3). The vertical distance between these two point is 563.00 mm, which is constrained by the green painted structure (figure 2.6). Therefore, the cross sectional dimensions were determined using ANSYS's built-in optimization tool. Like ADAMS virtual modelling, geometries for FEA were also created using ANSYS's built-in CAD package.

6.2.2.1. First Simulation Run. In order to determine a rough estimate of the I beam's cross sectional dimensions before using ANSYS's optimization tool, a model of the beam was created in ANSYS with the following characteristics.

Cross Sectional Dimensions: First Estimate. The figure (6.2) shows the first estimate of the I beam cross section drawn from a simple analysis by using the equation of stress concentration induced in a centrally loaded I beam (eq. 5.3 or eq. 5.14).

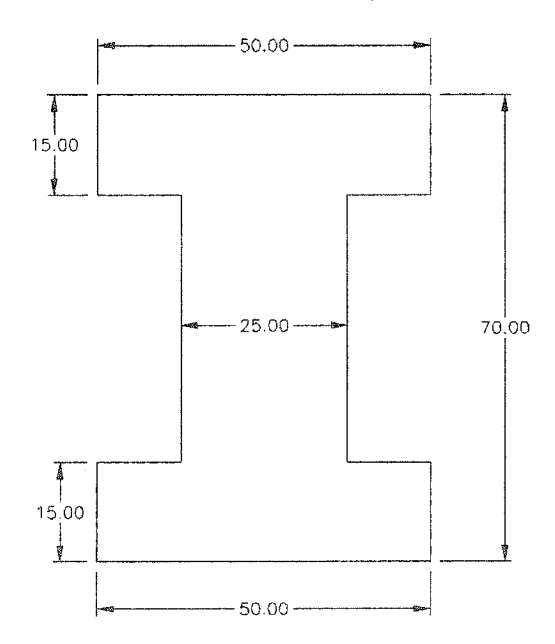


Figure 6.2: First estimate of the I beam section (all dimension are in mm).

Material Properties. Form the tables 4.2 and 4.3, values of modulus of elasticity and Poisson't ratio were chosen as 105 GPa and 0.31 respectively for the finite element analysis of all the Lever arm assembly components.

Beam Element Select. BEAM189 3-D Quadratic Finite Strain Beam was chosen as a beam element from the ANSYS's element library for designing the Lever arm because of the following reasons (ANSYS 7.0 Help, 2002),

- BEAM189 is an element suitable for analyzing slender to moderately stubby/thick beam structures. This element is based on Timoshenko beam theory. Shear deformation effects are included.
- BEAM189 is a quadratic (3-node) beam element in 3-D. BEAM189 has six or seven degrees of freedom at each node. This element is well-suited for linear, large rotation, and/or large strain nonlinear applications.
- BEAM189 includes stress stiffness terms, by default. The provided stress stiffness terms enable the elements to analyze flexural, lateral, and torsional stability problems (using eigenvalue buckling or collapse studies).
- In this beam element elasticity, creep, and plasticity models are supported (irrespective of cross-section subtype).

Solution Type. Nonlinear study state with large displacement static as an analysis option was chosen for defining the solution criteria in ANSYS. A load of 12, 700N (figure 6.1) with *ramped* loading option in 5 substeps for 1 second was applied on the middle of the I beam span for simulating the actual loading conditions. Ramped loading in 5 substeps for 1 second was used to design all the Lever arm components in ANSYS.

Simulation Results: First Run. The following figure shows results from the first FEA of an initial estimate of the I beam cross section, which provides a basis for running the design optimization tool.

In the figure 6.3, SMX, SMN and, DMAX are the maximum stress, minimum stress and the displacement induced in the beam due to loading, respectively.

As we can see from figure 6.3, the maximum stress induced in the I beam due to loading is 47.86 MPa. This result from the first FEA was verified with theoretical analysis (eq. 5.3

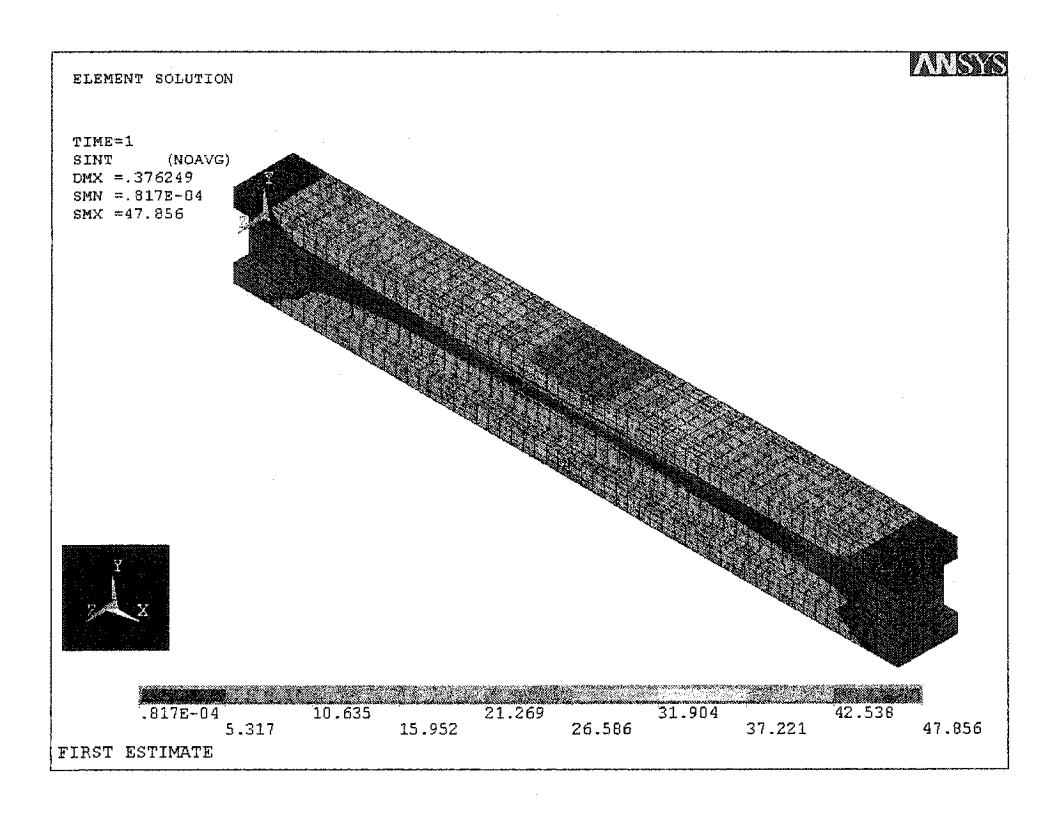


Figure 6.3: First FEA of the I beam cross section.

or eq. 5.14) as,

$$S_{max} = \frac{12700 \times 563/4}{(50 \times 70^3 - 25 \times 40^3)/(6 \times 70)} = 48.20 \ MPa$$
 (6.1)

The ANSYS FEA has an error of 0.71% (eq 6.1), which is a very small error.

6.2.2.2. Parameters for Design Optimization. As stated in the discussions section of the chapter 3, the following parameters were set in order to run the design optimization tool in ANSYS for designing the Lever arm through computational finite element analysis.

Design Variables (DVs). Initial approximation of the I beam cross section (figure 6.2) were set as the DVs for optimizing the design.

State Variable (SV). Maximum allowable stress in the beam was set as the SV, which was calculated as 163.33 MPa (eq 4.8).

Objective Variable (OV). Volume of the I beam was set as the OV due to the fact that primary objective of the FEA is to design a lighter weight Lever arm than the previous

Lever arm (figure 4.1), which has direct impact on the speed at the impact (figures 3.7 and 3.8).

6.2.2.3. Optimization Method. Optimization methods are traditional techniques that strive for minimization of a single function (the objective function) subject to constraints. The objective function is referred to as OV in the aforementioned paragraph. First-Order method was chosen as the optimization method. This method uses derivative information, that is, gradients of the dependent variables with respect to the design variables. It is highly accurate and works well for problems having dependent variables that vary widely over a large range of design space (ANSYS 7.0 Help, 2002; Moaveni, 1999).

6.2.2.4. Design Optimization Results. After running the design optimization tool, the following results (figure 6.5) were obtained for the I beam cross section shown in the figure 6.4 (dimensions are rounded off to the nearest whole numbers),

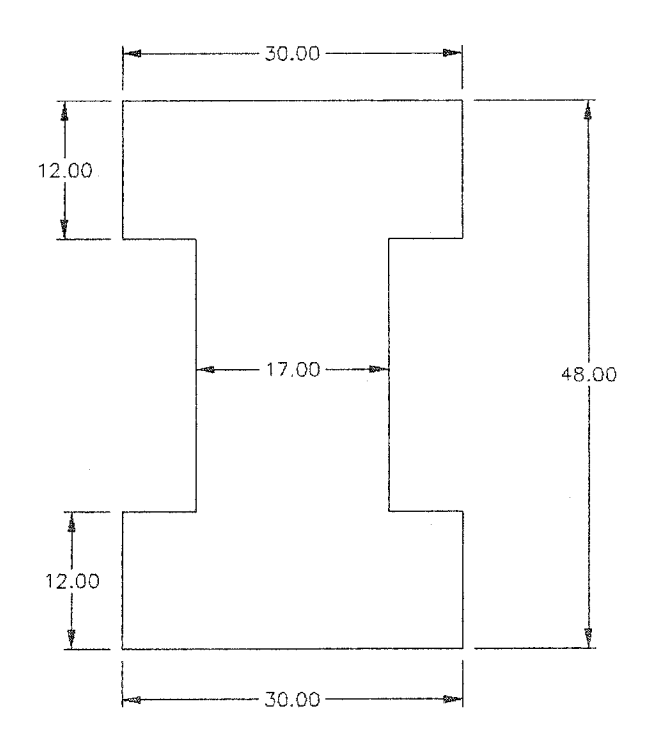


Figure 6.4: I cross section in mm from design optimization tool.

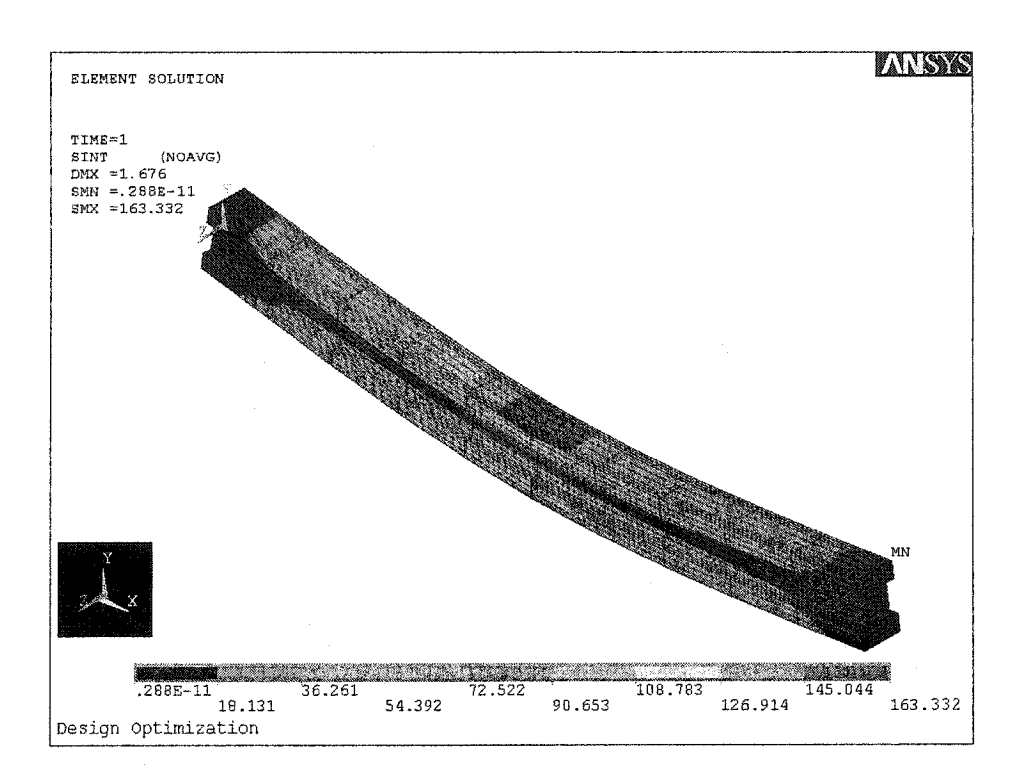


Figure 6.5: Results from design optimization tool.

6.2.3. Final I Cross Section. The I beam cross section shown in the figure 6.4 was expensive to manufacture because Titanium's manufacturing cost is higher than the material cost itself. This is why after consulting with a material supplier from *Titanium Industries* (Titanium Industries, 2003), a new I beam cross section was adapted according to the available Titanium sheets dimensions for reducing the manufacturing cost.

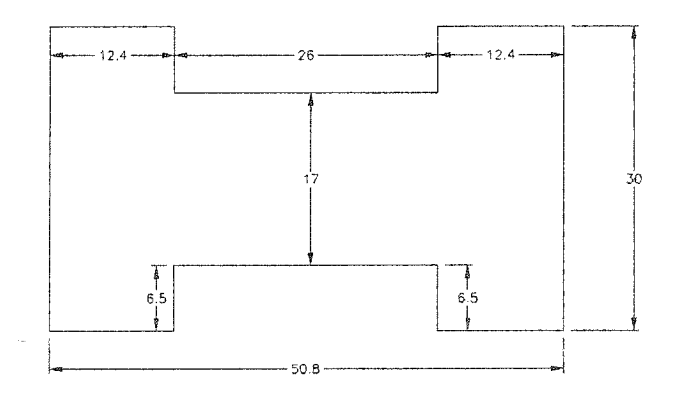


Figure 6.6: Final adapted I beam section in mm.

Figure 6.6 shows the finally adapted cross section of the I beam for reducing the manufacturing cost. In order to determine behavior of the newer design of the I beam, one more FEA was performed.

Figure 6.7 shows results obtained from the final FEA for the I section showed in the figure 6.6 in the process of designing the *Lever arm*.

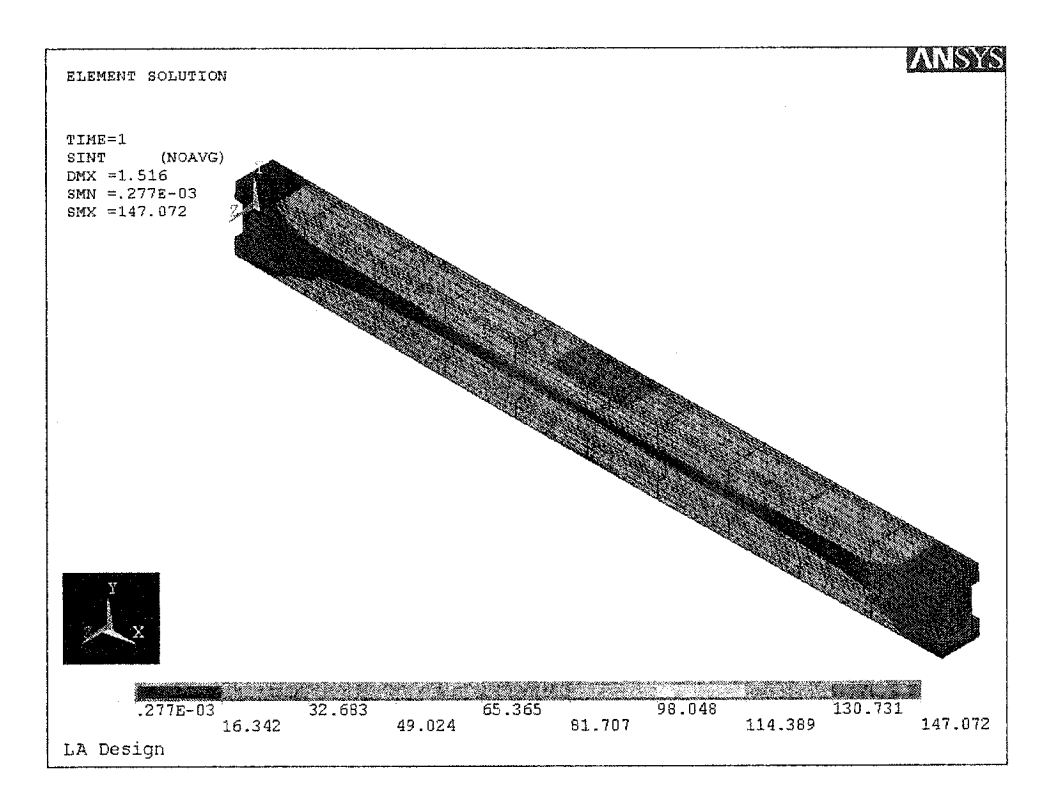


Figure 6.7: The last computational FEA run for the final adapted I beam section.

#### 6.2.4. Validation of Simulation Results with the Theoretical Analysis.

Simulation results from the ANSYS were verified with the theoretical analyses in order to figure out error in the ANSYS simulations. Only *Lever arm* design was used for ANSYS simulation validation purposes due to the fact that only the beam analysis was carried out comprehensively at the theoretical level because of its regular structural geometry. And FEA was use to analyze designs of all the Lever arm assembly components comprehensively.

I beam properties were calculated for the I cross section shown in the figure 6.6. The following calculations show I beam properties like moment of inertia, radius of gyration,

etc. calculated using equations 5.4, 5.5, 5.6 and 6.5.

$$I = \frac{BH^3 - bh^3}{12} = \frac{30 \times (50.8)^3 - 13 \times (26)^3}{12} = 308700.613 \ mm^4$$
 (6.2)

$$c = \frac{H}{2} = 50.8/2 = 25.4 \ mm \tag{6.3}$$

the radius of gyration,

$$k = \sqrt{I/A} = \sqrt{\frac{BH^3 - bh^3}{12(BH - bh)}} = \sqrt{\frac{308700.613}{1186}} = 260.287 \ mm$$
 (6.4)

and the section modulus,

$$\frac{I}{c} = \frac{BH^3 - bh^3}{6H} = 12153.567 \ mm^3 \tag{6.5}$$

Design of beams may be based on *strength* (stress) or on *stiffness* if deflection must be limited. For the loading specification shown in the figure 6.1, the maximum deflection (eq 5.12) and the maximum stress (eq 5.3 or 5.14) of an I beam can be calculated as,

$$f_{max} = \frac{PL^3}{48E_yI} = \frac{12700 \times (563)^3}{48 \times 105000 \times 308700.613} = 1.456 \ mm \tag{6.6}$$

$$S_{max} = \frac{M_{b_{max}}}{I/c} = \frac{PL/4}{I/c} = \frac{12700 \times 563/4}{308700.613/25.4} = 147.078 MPa$$
 (6.7)

The value of the deflection (eq. 6.6) under above mentioned loading condition differs from the value calculated by ANSYS programm (see the figure 6.7) due to the fact that load increases uniformly to the center in the ANSYS simulation as well as in the actual physical condition. On the other hand eq. 5.12 assumes that the load is concentrated at the center of span.

As it can be seen from the figure 6.7, maximum stress in the beam calculated using ANSYS is 147.072 MPa, which is very close to the value of maximum stress calculated theoretically (eq 6.7).

#### 6.3. Fifth Design Stage: Coupling Assembly Design

In the fourth stage of the Lever arm assembly design, the coupling assembly was designed, which consists of two *side brackets* and a *front part* (figure 4.3). Following figure shows 3-D solid model of the *coupling assembly* (exploded view).

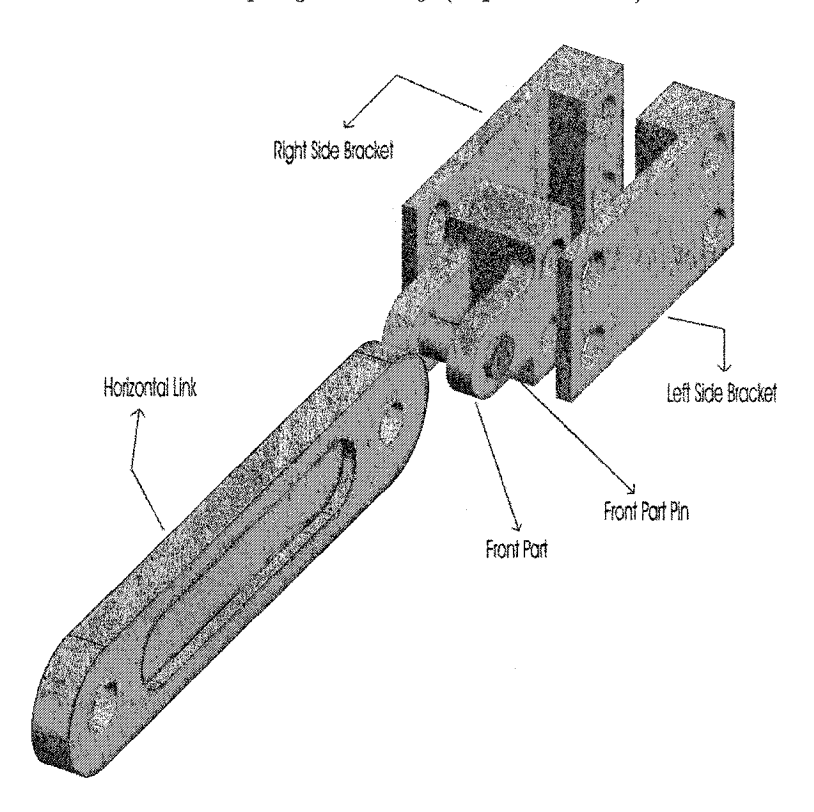


Figure 6.8: An exploded view of the coupling assembly with the horizontal link.

ANSYS FEA package was used for designing components shown in the figure 6.8. Since all the components can be easily termed as rigid bodies, it was assumed that the two side brackets and the front part are in tension under the influence of a spring force, which is equal to 12, 700 N. The coupling assembly components; two identical side brackets and the front part were designed separately.

**6.3.1.** Design of the Front Part. After finalizing the design of the coupling assembly (figures 4.3 and 6.8), boundary conditions for the front part were determined by assuming that the spring force is transmitted to the part assembled in series (figure 3.9). This means that the two front flanges of the front part are under the influence of a force,

tensile in nature and 12, 700 N in magnitude. This is why according to the *Newton's third* law of motion, the two cylindrical holes at the back side of the front part are also under the influence of a tensile force of 12, 700 N, but opposite in direction.

6.3.1.1. A Model of the Problem. Figure 6.9(a) shows a distribution of the pressure exerted by compression of the strongest spring with  $\kappa = 124.717 \ N/mm$  (Producto, 1996) in the inner areas (A9-A10 and A20-A21) of front flanges of the front part.

Following calculations show how the value of pressure applied to the above mentioned areas was calculated for the finite element analysis in ANSYS.

As it can be seen from the figure 6.9(a) force exerted on the two front flanges as a result of spring compression will be shared equally between the two inner half cylindrical surfaces A9-A10 and A20-A21. This is why the value of pressure applied to these cylindrical surfaces can be calculated as,

$$P_a = \frac{F_s/2}{\pi r_h l_h} \text{ MPa} \tag{6.8}$$

where  $P_a$  is the applied pressure in MPa,  $F_s$  is the force exerted by the spring due to its displacement in N,  $r_h$  is the radius and  $l_h$  is the length of the cylindrical holes in mm.

In figure 6.9(b), DOFs (degrees of freedoms) in the X and Y axis directions (UX and UY) were removed or set to zero displacement in order to simulate the actual physical loading conditions, which were determined on the basis of Newton's third law of motion.

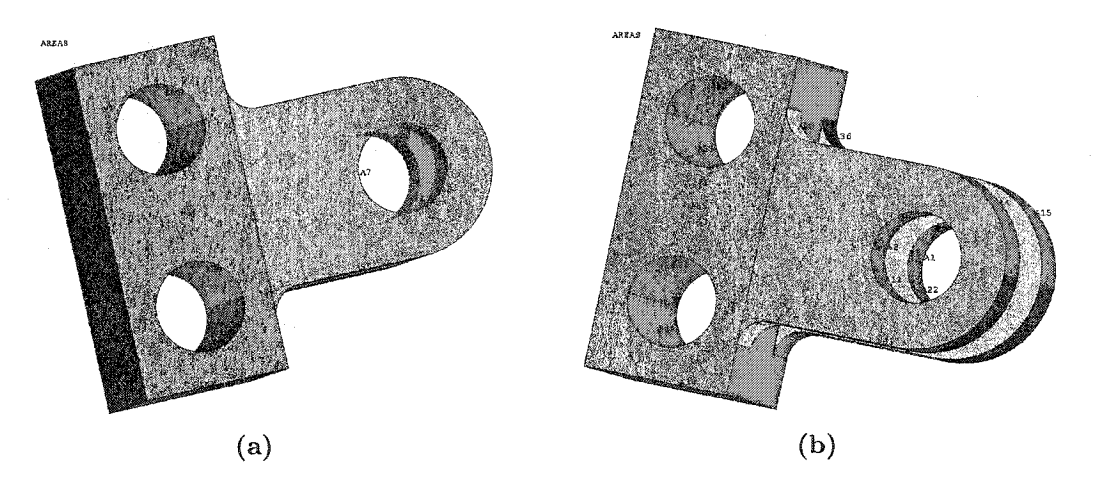


Figure 6.9: Front part in ANSYS modelling: (a) pressure applied; (b) DOF constraints applied.

- 6.3.1.2. Solid Element Select. SOLID187: 3-D 10-Node Tetrahedral Structural Solid was chosen as a solid element from the ANSYS's element library for designing all the Lever arm assembly components except the Lever arm because of the following reasons,
  - SOLID187 element is a higher order 3-D, 10-node element. SOLID187 has a quadratic displacement behavior and is well suited to modelling irregular meshes (such as those produced from various CAD/CAM systems).
  - The element is defined by ten nodes having three degrees of freedom at each node: translations in the nodal x, y, and z directions.
  - The element has plasticity, hyperelasticity, creep, stress stiffening, large deflection, and large strain capabilities. It also has mixed formulation capability for simulating deformations of nearly incompressible elastoplastic materials, and fully incompressible hyperelastic materials.
- 6.3.1.3. Determination of the Front Part Dimensions by Space Planning. Dimensions of the front part were determined mostly based on the space available to assemble it with the Lever arm, a horizontal link, which connects it to the spring shaft and the side brackets (figures 4.3 and 6.8).

A simple FEA was performed for determining thickness of the horizontal link. In order to reduce the manufacturing and the material cost associated with Titanium (Ti-6Al-4V), high quality regular structural steel with fatigue strength=500 MPa ( $10^7$  cycles) (MetWeb, 2003) was used to manufacture the horizontal link (figure 6.8). It was found that a thickness of 13.00 mm would be sufficient to ensure no failure (FOS = 3.0) under the influence of 12, 700 N of tensile force.

Several materials were considered for manufacturing the *front part pin* and the *bolts*, which could be used in assembling the front part with the side brackets and the horizontal link (figure 6.8). After discussing this design problem with an experienced manufacturer from *ELIMETAL*, *Inc.* (Fernandes, 2003), it was found that *hex socket head shoulder screws* of 5/8" or 15.88 mm diameter made from *grounded and heat treated stainless steel* have a minimum single shear strength of 28, 785 lbs (128, 070 N) at its shoulder part (Smith Fasteners, 2003).

Socket shoulder screws are ideal for precision assembly work with close tolerances and applications needing a well tooled appearance. This supplies greater tensile strength than

equivalent sizes of Grade-5 or Grade-8 hex head cap screws while requiring less surface area or counter bore since the fastener is internally wrenched (Smith Fasteners, 2003).

After finalizing the diameter of *cylindrical holes* and the separation between two *front flanges* in the front part at 15.88 mm and 16.00 mm respectively, the remaining dimensions were determined using ANSYS.

A few thorough finite element analyses were performed in order to determine remaining dimensions of the *front part*. The following figure shows an FEA result from ANSYS for the finally designed front part.

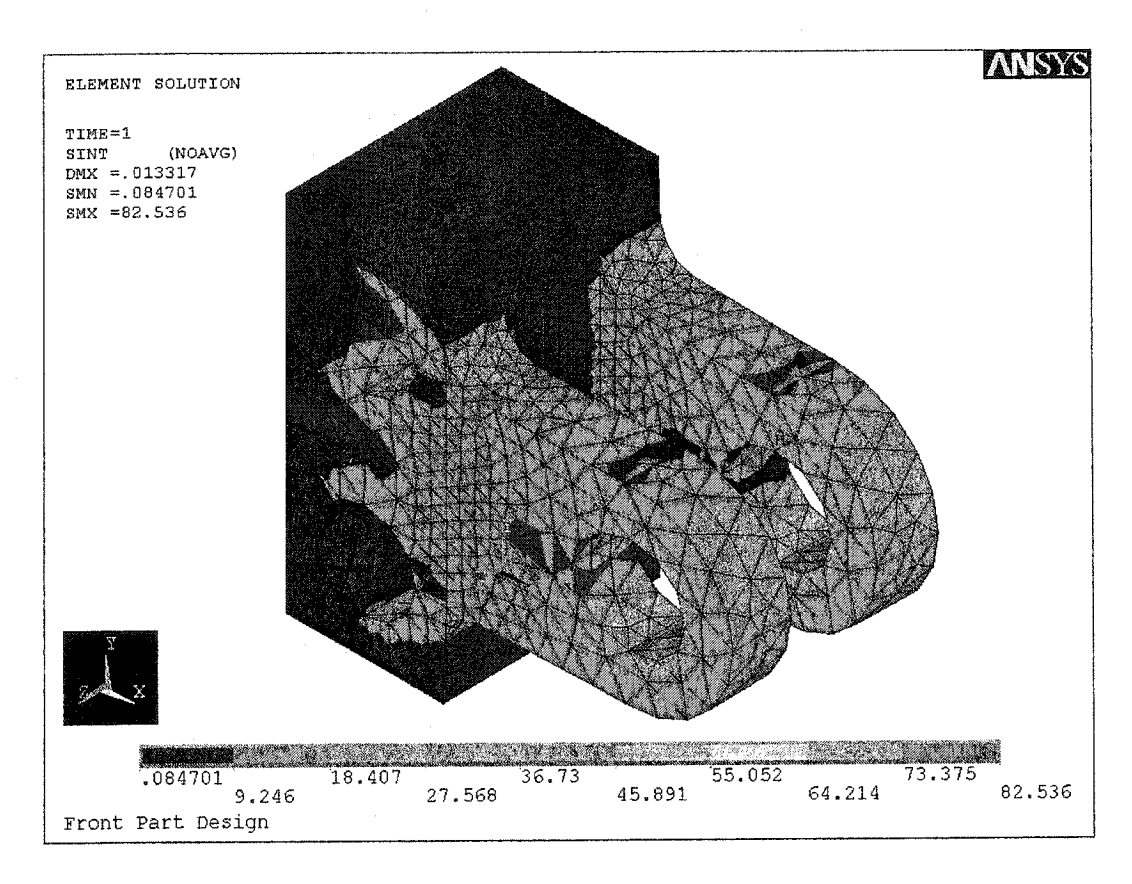


Figure 6.10: Simulation results obtained from the final computational FEA.

It can be seen from figure 6.10 that the maximum stress in the front part is 82.536 MPa, which is far less than the allowable design stress (163.33 MPa). The dimensions of the front part could not be reduced further due to fact that any kind of play should be avoided during the actual physical loading conditions by insuring *precision assembly* of the

front part with the other coupling assembly components and the Lever arm (figures 4.3 and 6.8).

6.3.2. Design of the Side Brackets. It can be seen from figure 6.8 that the coupling assembly requires two identical side brackets in order to assemble them to the front part and the Lever arm (figure 4.3). As mentioned earlier diameters of cylindrical holes in the front part were finalized at 15.88 mm, for insuring proper assembly of side brackets with the front part. The diameter of the side bracket's cylindrical holes was also finalized at 15.88 mm. Space planning was also considered in determining the side bracket's dimensions but primarily ANSYS was used to reach the final design of it.

Assuming the symmetrical distribution of the force exerted on the left and right side brackets due to the displacement of the spring, it can be stated that the force is equally distributed between them. This is why while designing the side brackets, equation 6.8 was slightly modified for simulating the actual loading conditions in the ANSYS simulation (eq 6.9).

$$P_a = \frac{F_s/4}{\pi r_h l_h} \text{ MPa} \tag{6.9}$$

The following figures show pressure applied on the front cylindrical holes and DOF constraints applied on the back cylindrical holes while designing the side brackets in ANSYS,

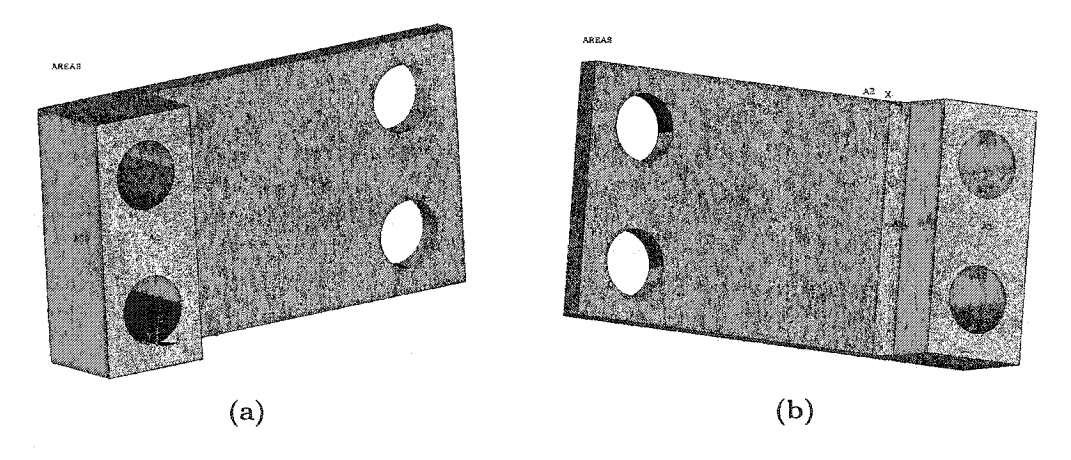


Figure 6.11: Side brackets in ANSYS modelling: (a) pressure applied; (b) DOF constraints applied.

It can be seen from figures 6.11(a) and 6.11(b) that pressure was applied on the areas A12-A15 and A8-A11 and DOF constraints were applied on the areas A33, A23, A24, A27, and A28. UX for the area A33 and UY for the areas A23, A24, A27, and A28 were removed or set to zero displacement in order to simulate the actual loading conditions.

A few thorough finite element analyses were performed in order to determine the remaining dimensions of the *side brackets*. Following figure shows an FEA result from ANSYS for the finally designed side bracket.

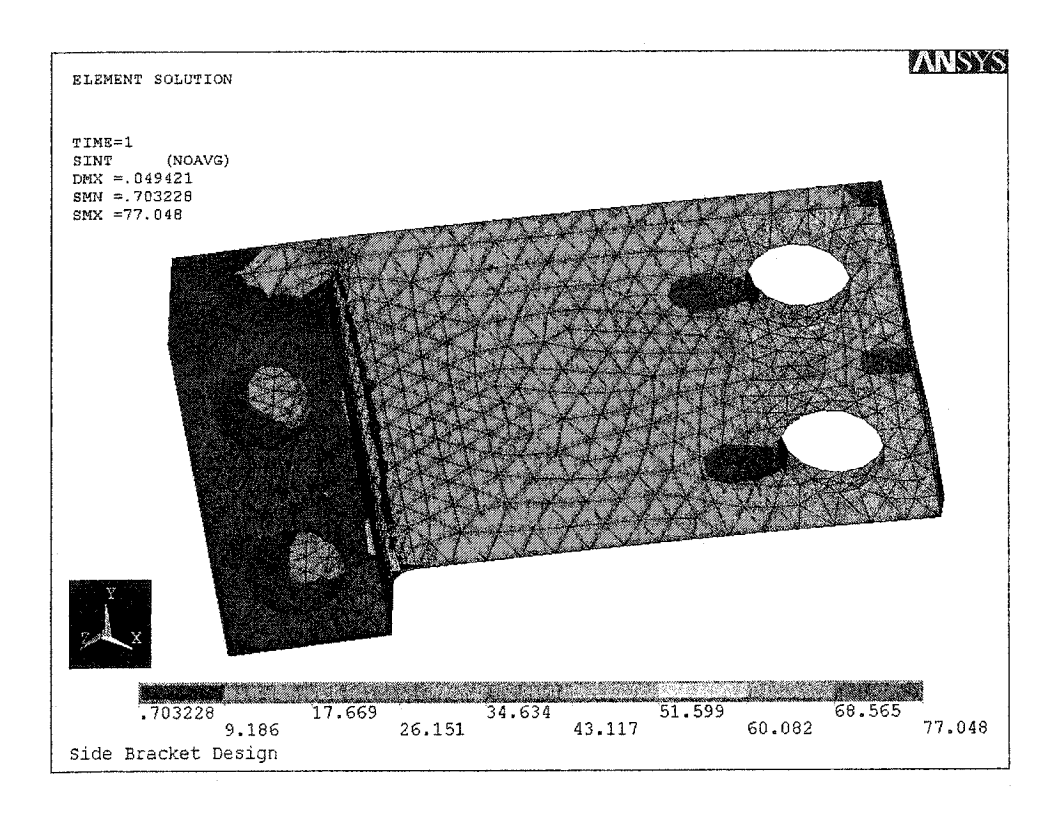


Figure 6.12: Simulation results obtained from the final computational FEA.

It can be seen from the figure 6.12 that the maximum stress in the front part is 77.048 MPa, which is far less than the allowable design stress (163.33 MPa). The dimensions of the side brackets could not be reduced further because of the same reasons, which were mentioned in the *front part* design section, that any kind of play should be avoided during the actual physical loading conditions by insuring *precision assembly* of side brackets with the other coupling assembly components and the Lever arm (figures 4.3 and 6.8).

#### 6.4. Final Design Stage: Follower Assembly Design

In the last design stage, the *follower assembly* was designed in order to complete the Lever arm assembly. The follower assembly consists of three components: main body, follower pin and follower roller. Except for the main body, the follower pin and the follower roller were designed solely within the space available to assemble them and the *cam* thickness (figures 1.8, 3.9 and 4.3). Stainless steel was chosen as a material to manufacture the follower roller because stainless steel is a standard material for manufacturing followers (Fernandes, 2003).

6.4.1. Determination of the Dimensions by Space Planning. As stated earlier, hex socket head shoulder screws have excellent shear strength at their shoulders, which is why a shoulder screw with 15.88 mm diameter was chosen as the *follower pin*. This decision helped to finalize the diameter of holes in the *main body* and internal diameter of the *follower roller* or *cylinder* at 15.88 mm.

The cam was 22.00 mm in thickness, which is why, in order to insure efficient use of the space available, the width of the follower roller was finalized at 22.00 mm.

Several options were considered for assembling the follower assembly to the Lever arm before determining main body's dimensions like using bolts, clamps, welded structure etc. Since Ti-6Al-4V has excellent welding properties (Titanium Industries, 2003; Henry et al., 1995) so it was decide that the follower assembly would be *welded* to the Lever arm. Figure 6.13 shows an exploded view of the follower assembly.

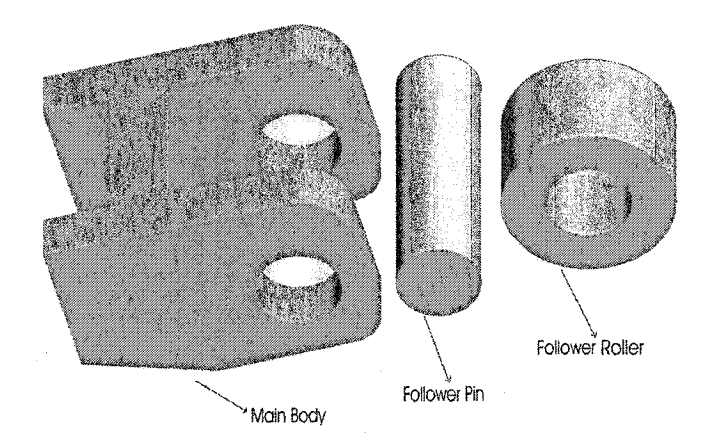


Figure 6.13: An exploded view of the follower assembly.

While determining dimensions of the main body, a few interrelated parameters like outer diameter of the follower roller, its position on the main body and the main body's position on the Lever arm were determined in order to insure no contact between the tip of the cam and the bottom part of the Lever arm, when the cam leaves the follower roller.

A few trigonometrical geometry drawings were sketched for determining the path traced by the cam-follower roller contact point. Later ADAMS simulation software in conjunction with ANSYS was used to simulate various positions of the main body on the Lever arm in order to reduce stress concentration at the Lever arm-main body interface.

Various combinations of the follower roller's position on the main body and main body's position on the Lever arm were evaluated *simultaneously*, and it was found out that an outer diameter of 32.00 mm for the follower roller would help to insure no contact between the cam and the bottom part of the Lever arm. The following trigonometrical geometry shows the path traced by the cam-follower roller contact point, drawn after finalizing the outer diameter of the follower roller at 32.00 mm.

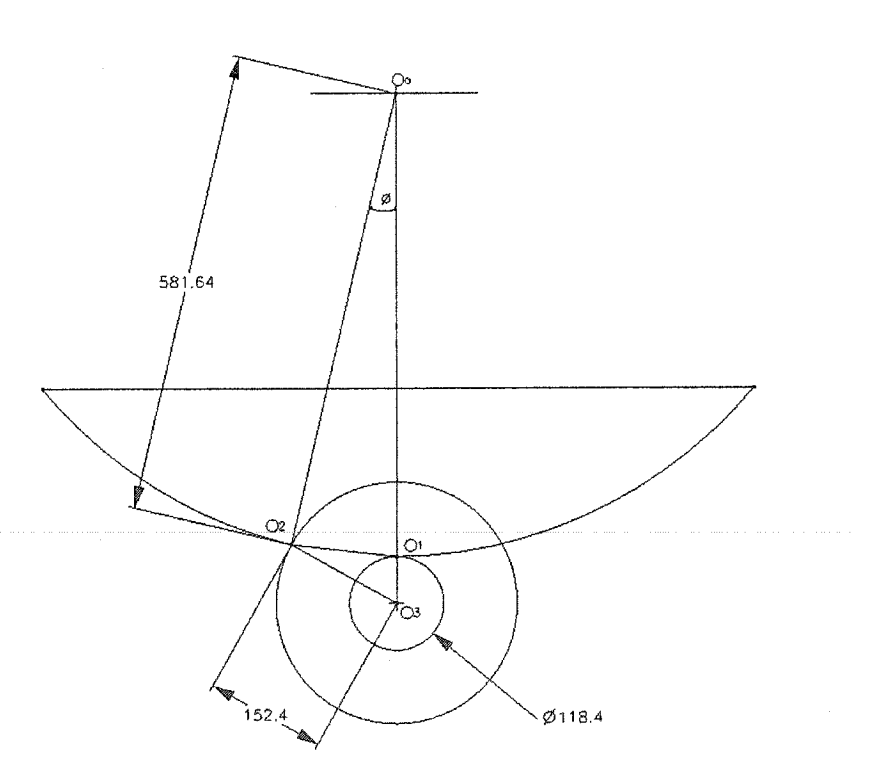


Figure 6.14: Path traced by the cam-follower roller contact point.

As it can be seen from figure 6.14, the contact point moves from the point  $O_1$  to  $O_2$  in a circular path at a distance of 581.64 mm from the pivot point O, which was calculated from a simple trigonometrical relation. Since the Lever arm is 563.00 mm in length and the contact point moves at a distance of 581.64 mm from the point O, so it can be easily said that the cam will not come in contact with bottom part of the Lever arm. It was also verified with ADAMS simulation.

Equation 6.8 was used for calculating the applied pressure on the inner half cylindrical surfaces of the two cylindrical hole as shown in the following figure.

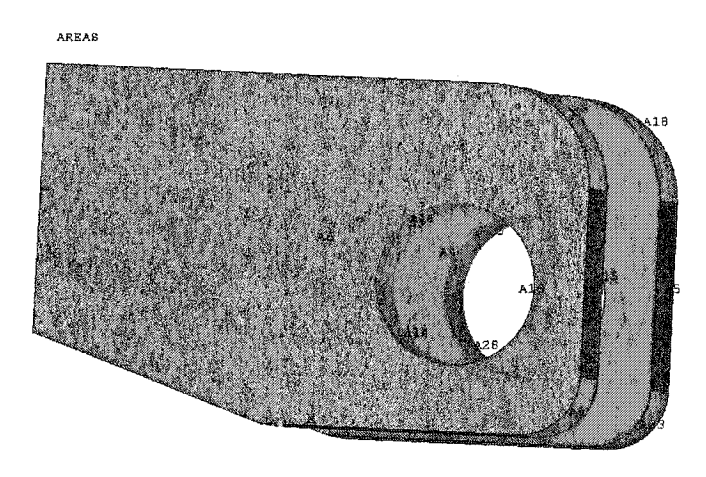


Figure 6.15: Pressure applied on the main body in ANSYS modelling.

Since the follower-Lever arm assembly was crucial for the success of the whole Lever arm assembly design, therefore in order to generate more confidence in the follower assembly design, full value of the spring force (12, 700N) was used to calculate the value of pressure applied to A11-A14 and A25-A28 half cylindrical surfaces (figure 6.15) instead the value of the force calculated after applying the Lever's principle.

Figure 6.16 shows the applied DOF constraints on the main body. In order to simulate actual loading conditions on it, lines L75, L85, L115, L124, L127, L131, L133, and L134 were constrained in the UY direction, areas A64 and A68 were constrained in the UZ direction and area A72 was constrained in the UX direction.

A few thorough finite element analyses were performed in order to determine remaining dimension of the *main body*. The figure 6.17 shows an FEA result from ANSYS for the finally designed main body.

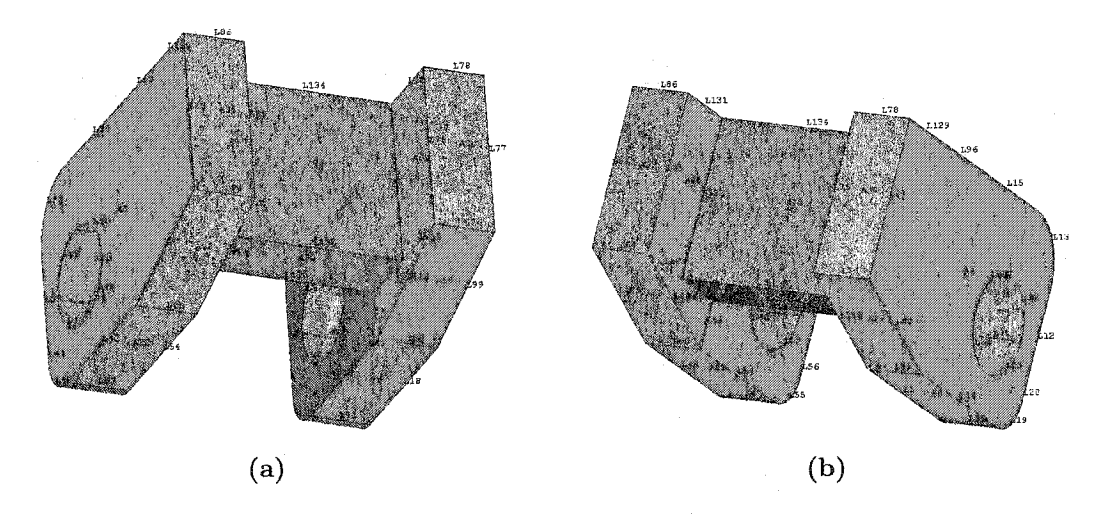


Figure 6.16: DOF constraints applied on the main body in ANSYS modelling.

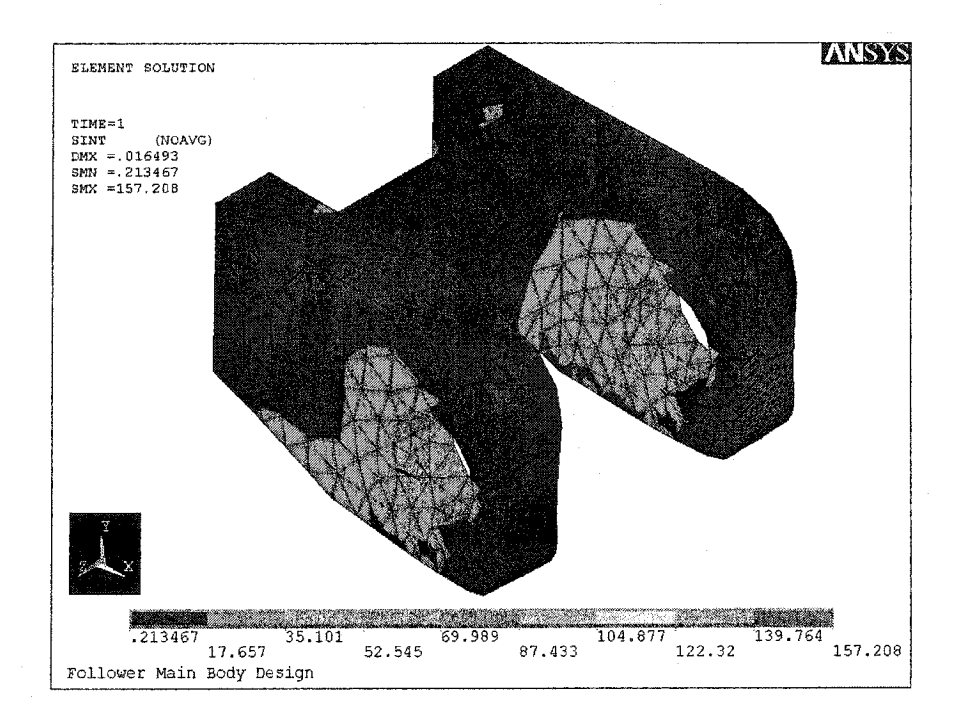


Figure 6.17: Simulation results obtained from the final computational FEA.

It can be seen from figure 6.17 that the maximum stress in the front part is 157.208 MPa, which is less than the allowable design stress (163.33 MPa). The dimensions of the main body could not be reduced further because of the same reasons, which were mentioned in the *front part* and *side brackets* design sections that any kind of play should be avoided

during the actual physical loading conditions by insuring *precision assembly* of the main body with the other follower assembly components and the Lever arm (figures 4.3 and 6.13).

The following figure shows a sketch of the follower assembly assembled to the Lever arm. This figure supports the established trigonometrical relations mentioned in the aforementioned paragraphs (figure 6.14). In order to reduce stress concentration at the main body-Lever arm interface, larger area was provided for welding by increasing the length of Lever arm by 6.60 mm.

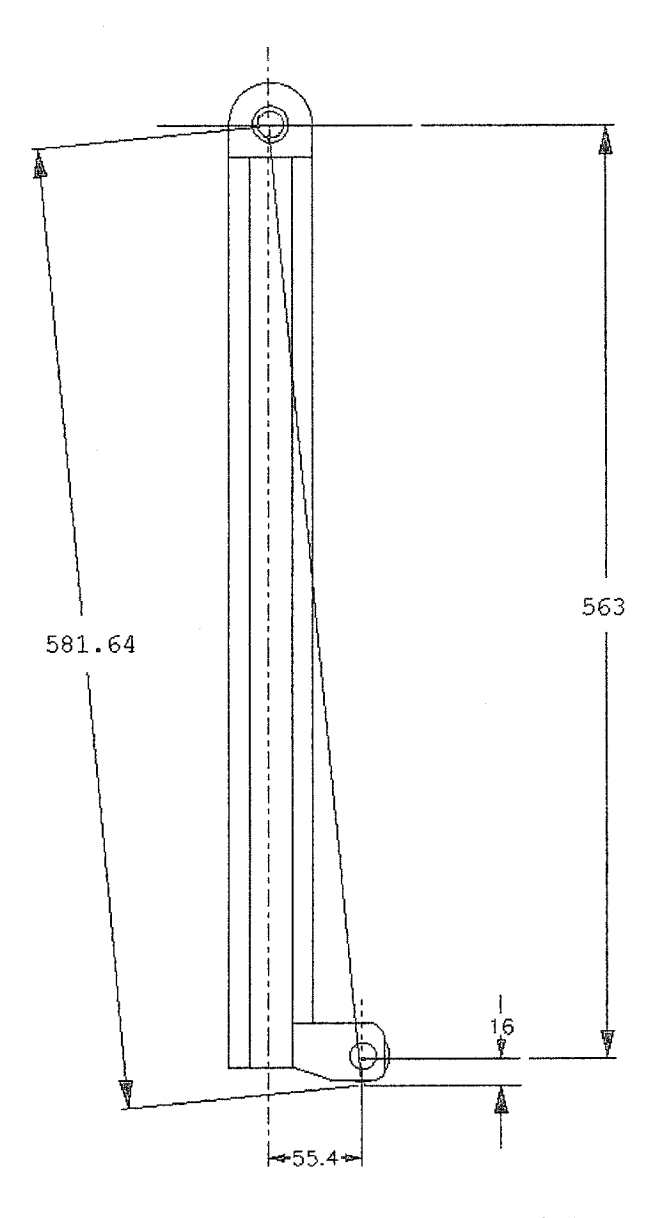


Figure 6.18: Trigonometrical relations: Lever arm-follower sub assembly.

## Development and Setup of Version III of the Impact Wear Tester Prototype

After subsequently improving designs and performances of the version I and version II of the impact wear tester, the newest impact wear tester; version III of the impact wear tester was designed and developed. The following sections explain development and test setup of version III of the impact wear tester along with theoretical calculations for measuring speed at the impact.

#### 7.1. Development of the Impact Tester Prototype

After having designed all the Lever arm assembly components, their engineering drawings were sent to *Elimetal Inc.* (a local manufacturer) to be manufactured by *wire EDM* method after consulting a manufacturing specialist (Fernandes, 2003). Engineering drawing of the Lever arm assembly components can be found in the Appendix A.

Wire EDM (Electrical Discharge Machining) uses a wire electrode as thin as a hair that generates heat due to electrical discharge phenomena, like lightning, to melt the metal workpiece to cut it. The wire does not make contact with the workpiece during cutting. This manufacturing method was chosen over other methods due to the fact that this method has quite remarkable efficiency and surface finishing when used to manufacture difficult-to-machine materials and to create intricate profiles and tapers as the wire follows its programmed path (Sommer et al., 2000).

Following figure shows a 3-D model of the version II of the impact tester prototype. As mentioned in the chapter 2, the caret holder is assembled to the double threaded cylinder and this cylinder is assemble to the spring shaft assembly while this spring shaft assembly is connected to the Lever arm assembly. The spring is inside the stationary spring housing with one end sitting against the stationary plate and the other end in contact with the reciprocating double threaded cylinder.

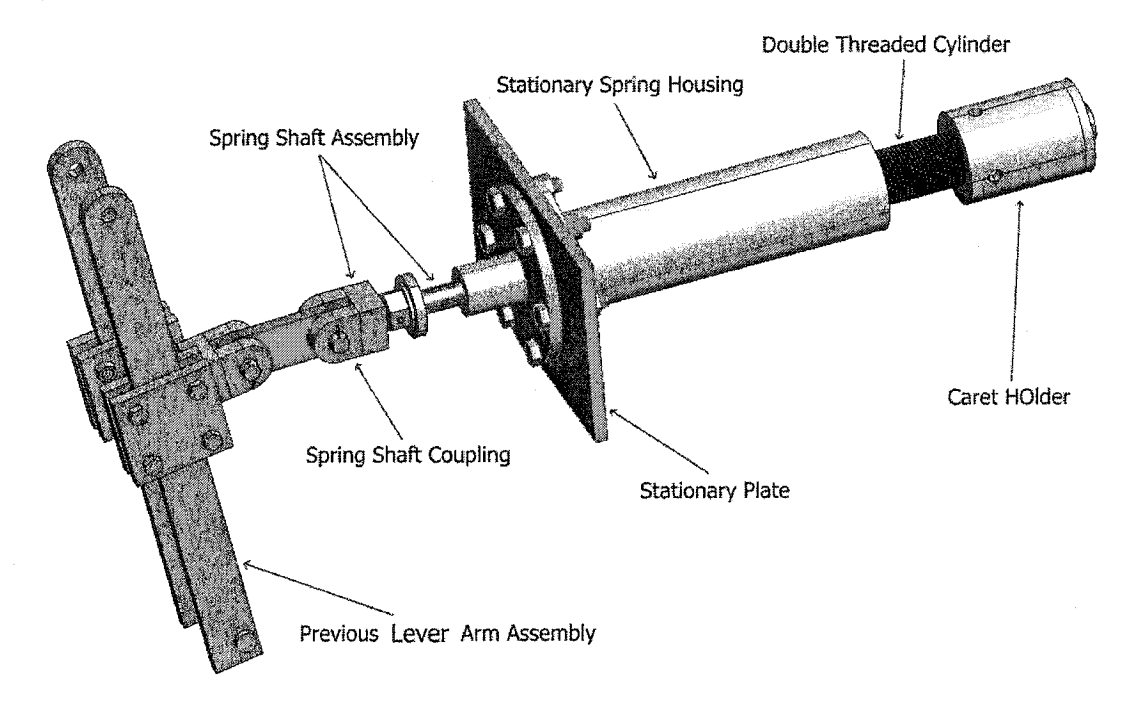


Figure 7.1: A 3-D model of version II of the impact tester assembly.

In order to reduce weight of the reciprocating assembly further, which has a profound impact on speed at impact, material of the spring shaft assembly and the double threaded cylinder was changed from regular structural steel to Al 7075-T6: a very high strength material used for highly stressed structural parts. Aluminum 7075-T6 is the strongest structural alloy of the aluminum's alloy family with density equal to 2.81 g/cc or 2810 kg/m<sup>3</sup>. Table 7.1 shows some mechanical properties of the Al 7075-T6.

Since dimensions of the the spring shaft assembly and the double threaded cylinder were constrained by the stationary plate, the stationary spring housing (figures 7.1 and 2.6) and the space available for spring displacement (figure 3.9), a few simple FEA were performed using ANSYS in order to find out the maximum stress concentration in these components

Mechanical properties	Value (SI)
Tensile Strength, Ultimate	570 MPa
Modulus of Elasticity	72 GPa
Poisson's Ratio	0.33
Fatigue Strength	$160 \text{ MPa } (5 \times 10^8 \text{ Cycles})$

Table 7.1: Mechanical properties of the Al 7075-T6 (Henry et al., 1995).

during loading conditions. It was found out that the maximum stress concentration would be less than the allowable design stress (53.33 MPa) for the FOS equal to 3.0 during the actual loading conditions based on *fatigue strength* of the material (table 7.1).

Table 7.2 shows a comparison between weights of mobile components of the old set (version II) and the new set (version III) of the impact wear tester. In this table, the spring shaft assembly also includes weight of the *horizontal link* (figure 6.8).

Components name		Weights in kgs after upgrade	
Double Threaded Cylinder	2.90	1.03	64.48
Spring Shaft Assembly	4.0	2.60	35.0
Lever Arm Assembly	12.30	5.12	58.37

Table 7.2: A comparison between weights before and after upgrading the impact tester prototype.

#### 7.2. Setup of the Impact Tester Prototype

After receiving all the impact tester's components from the manufacturer, the components were assembled and a mechanical counter was attached for counting the number of impacts.

Figure 7.2 shows an actual photograph taken after assembling the complete Lever arm assembly along with the horizontal link to the impact tester version III. As it can be seen from figures 4.3 and 7.2, all four sides of the coupling assembly are surrounded by rubber pads in order to avoid any direct metal to metal contact between coupling assembly components and the Lever arm. Rubber pads can also function as *dampers* and absorb some vibrations during impact tester operations.

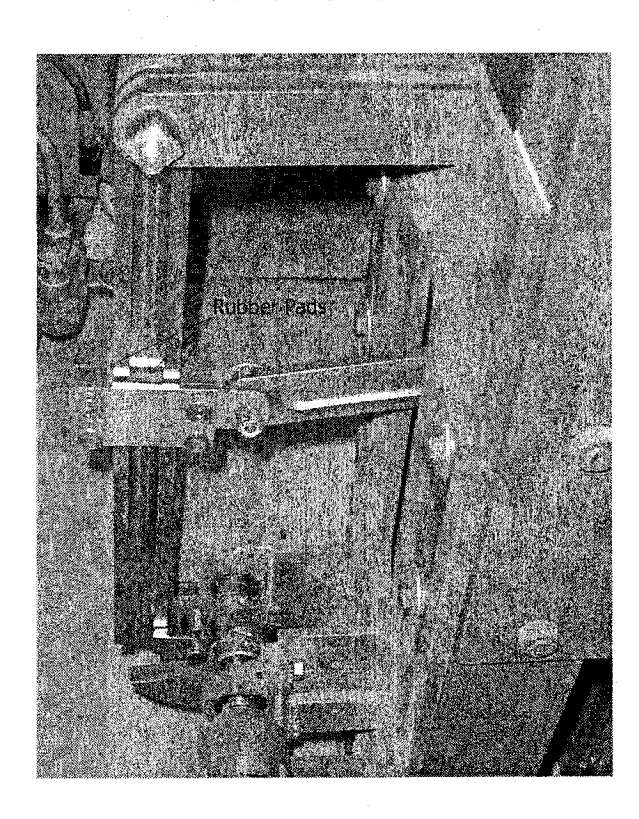


Figure 7.2: Lever arm assembly assembled to the horizontal link in the impact tester version III.

After having all the parameters related to the impact tester's dynamics, e.g., dimensions and weights of the all the reciprocating components, figure 3.2 was redrawn as shown in figure 7.3 and equation 3.5 from the chapter 3 for calculating spring displacement  $(D_i)$  was modified.

The value of angle  $\phi$  was calculated for the Lever arm posture shown in the figure 7.3 by using equation 3.3 as,

$$(152.4)^2 = (581.64)^2 + (640.84)^2 - 2(581.64)(640.84)\cos\phi \Longrightarrow \phi = 13.21^o$$
 (7.1)

Now the equation 3.5 can be modified as,

$$D_i = 2\sin(13.21/2)r_i = 0.23r_i \tag{7.2}$$

From equation 7.2, spring displacement  $(D_i)$  can be easily calculated for the different values of  $r_i$ .

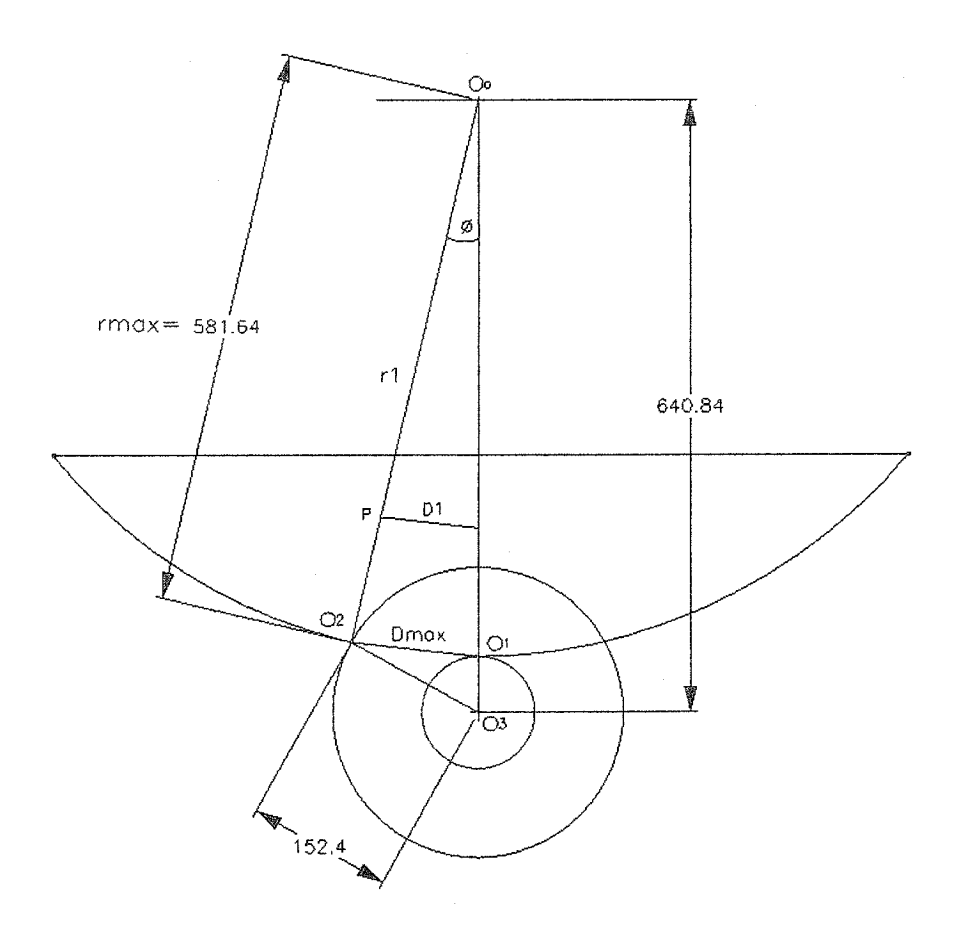


Figure 7.3: Trignometrical relation for the path traced by the cam-follower roller contact point (all dimensions are in mm).

### 7.3. Speed at Impact by Theoretical Analysis

In order to measure speed at impact theoretically and to compare it with the ADAMS simulations mentioned in the chapter 3, an extra high pressure die spring (color coded green) with a spring constant ( $\kappa$ ) = 124.717 N/mm (Producto, 1996) was used. The spring was compressed for 3.78" or 96.00 mm, which is 31.50% of its free length, which is equal to 12 or 304.80 mm.

Equation 3.24 was used to calculate speed at impact. The following parameters were entered in this equation for calculating speed at impact.

 $\kappa = 124.717 \text{ N/mm}.$ 

 $D_i = 3.78$ " or 96.00 mm.

 $\mu_{dr} = 0.1$  (ADAMS/View 12.0 Help, 2001).

 $\mu_{ds} = 0.35$  (ADAMS/View 12.0 Help, 2001).

 $W'_{la} = 5.12 \text{ kg}.$ 

 $W'_{rc} = 5.53 \text{ kg}.$ 

 $\angle \phi = 13.2^{\circ}$ 

 $r_p = 7.94 \text{ mm}.$ 

 $F = \kappa D_i = 11972.83 \text{ N}$ 

Since, the value of  $r_i$  calculated from equation 7.2 is 417.40 mm. Therefore, equation 5.12 needed to be modified in order to calculated the value of  $f_{max}$  as,

$$f_{max} = \frac{F(L - r_i)}{3E_y IL} \left[ \frac{r_i (L + L - r_i)}{3} \right]^{3/2}$$
 (7.3)

$$f_{max} = \frac{11972.83(563 - 417.40)}{3(105000)(308700.613)(563)} \left[ \frac{417.40(1126 - 417.40)}{3} \right]^{3/2} = 0.98 \ mm \tag{7.4}$$

Now, from the equation eq. 3.24, speed at the impact can be calculates as,

$$v_{imp} = \sqrt{\frac{1149391.87 - 2[53.66 \times \cos(13.2) + 185.80] - 11733.37}{1000[5.53 + 5.12 \times \cos(13.2) - 5.12 \times \sin(13.2)]}} = 11.03 \ m/sec$$
 (7.5)

The speed at the impact calculated from the eq. 7.5 is equivalent to 6.20 m or 620 cm of drop height. The speed at the impact calculated by the eq. 7.5 is very close to the speed at the impact obtained from the third ADAMS simulation run (figure 3.8) mentioned in chapter 3.

# Conclusions and Recommendations for Future Work

#### 8.1. Conclusions

Version III of the impact wear tester has been designed and developed in this research project work. In addition to this, two important impact wear tester components: caret and target ball holders for version II of the impact wear tester were also designed, which were also used in completing the version III of the tester assembly.

The literature survey and the study of previous semi-empirical approaches helped to understand inherent the importance of the impact wear for the total steel media wear. Tying data from DEM charge motion simulation with data obtain from version III of the impact wear tester can greatly improve the prediction of impact wear in an autogenous or semi-autogenous tumbling mill.

Theoretical and virtual (ADAMS) dynamic analyses helped to determine design, state and objective variables, which were used in optimizing the impact wear tester's mobile assembly components design while using computation finite element analysis (ANSYS). Final design of the Lever arm assembly was reached after proposing eight evolutionary designs of it. ANSYS was used comprehensively for designing and determining dimensions of the Lever arm assembly components because of its very powerful postprocessor and graphical capabilities. ANSYS is widely used for nonlinear structural analyses in the field of engineering.

The Lever arm assembly components were manufactured by Wire EDM. This manufacturing method is very well known for its very high precision manufacturing capabilities specially when used to manufacture components from hard to machine material like Titanium. Ti-6Al-4V, ASTM Grade 5 was chosen as material to manufacture Lever arm assembly components because of its very high strength to weight ratio.

Previous semi-empirical attempts; version I and version II of the impact wear tester could only achieve energies equivalent to 4 cm and 9.8 cm of drop height respectively. On the other hand version III of the impact wear tester can achieve impact energy equivalent to maximum 620 cm of drop height (eq. 7.5).

The version III of the impact wear tester has the following important features:

- (i) It is lighter in weight than the version II of the impact wear tester.
- (ii) It has fewer number of parts.
- (iii) It can allow easy alteration of spring compression amplitude.
- (iv) It insures no failure at high energy impact testing (FOS = 3.0).
- (v) It can allow the determination of the impact wear rate at a wide range of impact energies.
- (vi) It offers less dynamic rolling and sliding friction coefficients, which has some effect on speed at the impact.
- (vii) It needs little or no maintenance because of its robust design.
- (viii) It is well optimized for achieving maximum speed at the impact.
- (ix) It can be tested for energy levels up to equivalent of 620 cm of drop height.

Speed at the impact was calculated theoretically because maximizing speed at impact by implementing new design ideas was the prime objective of this thesis research project work.

#### 8.2. Recommendations for Future Work

In this thesis research work, an impact wear tester was designed and developed, which will allow the determination of the contribution of the impact wear for the total media wear over a wide range of impact energy levels. Future work could look into the prospect of fully utilizing the potential of version III of the impact wear tester.

An extension to the present work is recommended as follows:

- (i) A hydraulic drive should be used for driving the follower roller.
- (ii) Either a high-speed camera or an accelerometer should be used for measuring the speed at impact.
- (iii) Preparation of a commission test campaign to determine test repeatability as a function of impact specific energy is also recommended.

### **BIBLIOGRAPHY**

- Adams, V., and Askenazi, A., 1999, Building Better Products With Finite Element Analysis, OnWord Press, Santa Fe, NM.
- ADAMS/Solver, 2001, *Using ADAMS/Solver*, Automatic Dynamic Analysis of Mechanical Systems, MSC Software, Santa Ana, CA.
- ADAMS/View 12.0, 2001, Getting Started Using ADAMS/View 12.0, Automatic Dynamic Analysis of Mechanical Systems, MSC Software, Santa Ana, CA.
- ADAMS/View 12.0 Help, 2001, Intranet HTML Help On Using ADAMS/View 12.0, Automatic Dynamic Analysis of Mechanical Systems, MSC Software, Santa Ana, CA.
- Anderson, D. O., 2001, Safety Factor, Department of Mechanical Engineering Technical Report, Louisiana Tech University, Ruston, Louisiana, pp. 1–7.
- ANSYS 7.0 Help, 2002, Intranet HTML Documentation for ANSYS 7.0 Help, ANSYS, Inc., Canonsburg, PA.
- Baumeister, T., Avallone, E. A. and BaumeisterIII, T., 1988, Mark's Standard Handbook for Mechanical Engineers, Eighth Edition, McGraw-Hill Book Company, New York, pp. 5.2–5.37.

- Blickensderfer and Tylczak, 1989, "Evaluation of Commercial US Grinding Balls by Laboratory Impact and Abrasion Tests", *Miner. Metall. Process*, Vol. 6, pp. 60–66.
- Burr, A. H. and Cheatham, J. B., 1995, *Mechanical Analysis and Design*, Second Edition, Prentice Hall, Englewood Cliffs, New Jersey.
- Dorlot, Baïlon and Masounave, 1986, "Des Matériaux, Éd. l'École Polytechnique, Montréal, Quebec.
- Fernandes, J., 2003, Technical Service & Sales Representative, Private Consulting, Elimetal, Inc., St. Laurent, Quebec.
- Gangopadhyay, A. and Moore, J., 1987, "Effect of Impact on the Grinding Media and Mill Liner in a Large Semiautogenous Mill", Wear, Vol. 114, pp. 249–260.
- Girard, M., 2000, Simulateur D'Impact. Rapport De Conception, Université du Québec en Abitibi-Témiscamingue, Montréal, Quebec.
- Greenspan, H. P. and Benney, D. J., 1973, Calculus. An Introduction to Applied Mathematics, McGraw-Hill, Inc., New York.
- Gundewar, Natarajan, Nayak and Satyanarayana, 1990, "Laboratory Studies on Ball Wear in the Grinding of a Hematiti-Magnetite Ore", *The International J. of Mineral Processing*, Vol. 29, pp. 121–139.
- Henry, S. D., Davidson, G. M., Lampman, S. R., Reidenbach, F., Boring, R. L. and Scott, W.W., Jr., 1995, Fatigue Data Book: Light Structural Alloys, ASM International, OH, pp. 181–385 & pp. 1–110.
- Jennings, B. H. and Obert, E. F., 1950, Internal Combustion Engines, Analysis and Practice, International Textbook Co., Scranton, Pennsylvania, pp. 23–49.

- Juvinall, R. C., 1983, Fundamentals of Machine Component Design, John Wiley & Sons, New York, p. 176.
- Juvinall, R. C. and Marshek, K. M., 1991, Fundamentals of Machine Component Design, Second Edition, John Wiley & Sons, New York, pp. 224–225.
- MetWeb, 2003, Material Property Data, Automation Creations, Inc., Blacksburg, VA, URL http://www.matls.com/index.asp?ckck=1.
- Mishra and Finnie, 1980, "A Classification of Three-Body Abrasive Wear and Design of a New Tester", Wear, Vol. 60, pp. 111–121.
- Mishra, B. K. and Rajamani, R. K., 1994, "Simulation of Charge Motion in Ball Mills, Part 2: Numerical Simulations", *The International J. of Mineral Processing*, Vol. 40, pp. 187–197.
- Moaveni, S., 1999, Finite Element Analysis. Theory and Application With ANSYS, Prentic Hall, Upper Saddle River, NJ.
- Nass, D. E., 1974, Materials for the Mining Industries, Climax Molybdenum, Ann Arbor, MI, p. 173.
- Natarajan, K., 1992, "Ball Wear and its Control in the Grinding of a Lead-Zinc Sulphide Ore", *The International J. of Mineral Processing*, Vol. 34, pp. 161–176.
- Norton, R. L., 1996, Machine Design An Integrated Approach, Prentice-Hall, Upper Saddle River, New York, p. 21.
- Producto, 1996, The Complete Catalogue of Springs for All Your Needs, Producto Diemakers Suppliers Limited, Montreal, Quebec, pp. 1–6.

- Pugsley, A. G., 1966, The Safety of Structures, Edward Arnold, London.
- Radziszewski, P. and Tarasiewicz, S., 1993a, "Modelling and Simulation of Ball Mill Wear", Wear, Vol. 160, pp. 309–316.
- Radziszewski, P. and Tarasiewicz, S., 1993b, "Simulation of Ball Charge and Liner Mill", Wear, Vol. 169, pp. 77–85.
- Radziszewski, P., 1997a, Chapter 4: Ball Mill Media Wear and Prediction, JKMRC/AMIRA P9L Technical Project Report, Queensland, Australia, pp. 35–51.
- Radziszewski, P., 1997b, "Predictive Model For Ball Mill Wear", Canadian Metallurgical Quarterly, Vol. 36, No. 2, pp. 87–93.
- Radziszewski, P., 1997c, Part 2. Detailed Proposal on Predicting Steel Wear in Mills: Refinement and Validation, A Detailed Technical Proposal to AMIRA International, Australia, Vol. 2, pp. 1–3.
- Radziszewski, P., 1998, Chapter 5: Preliminary Results from Media Wear Tests, JKMRC/AMIRA P9L Technical Project Report, Queensland, Australia, pp. 75-86.
- Radziszewski, P. and Morrell, S., 1998, "Fundamental Discrete Element Charge Motion Model Validation", Minerals Engineering, Vol. 11, No. 12, pp. 1161–1178.
- Radziszewski, P., 1999a, "Comparing Three DEM Charge Motion Models", *Minerals Engineering*, Vol. 12, No. 12, pp. 809–826.
- Radziszewski, P., 1999b, Exploring Total Media Wear, JKMRC/AMIRA P9L Technical Project Report, Queensland, Australia.

- Radziszewski, P. and Valery, W., 1999, "Cadia SAG Mill Simulated Charge Behaviour, CMP, Ottawa, Ontario, pp. 267–283.
- Radziszewski, P., 2000, An Update on Mill Media Impact Test Improvement, JKMRC/AMIRA P9L Technical Project Report, Queensland, Australia.
- Radziszewski, P., 2001, Exploring Total Media Wear, Mechanical Engineering Department Technical Report, McGill University, Montreal, Quebec.
- Radziszewski, P., 2002, "Exploring Steel Media Wear", *Minerals Engineering*, Vol. 15, No. 12, pp. 1073–1087.
- Radziszewski, P. and Thakur, L., 2003, "Predicting the Contribution of Impact Wear to Total Steel Media Consumption", *The XXII International Mineral Processign Congress*, Cape Town, South Africa.
- Rajagopal and Iwasaki, 1992, "The Properties and Performance of Cast Iron Grinding Media", Min. Process. Extrac. Metall. Rev., Vol. 11, pp. 75–106.
- Rao, Y. and Nararajan, K., 1991, "Factors Influencing Ball Wear and Flotation with respect to Ore Grinding", Min. Process. Extrac. Metall. Rev., Vol. 7, pp. 137–173.
- Rice, R. C., Leis, B. N. and Nelson, D. V., 1988, Fatigue Design Handbook/prepared under the auspices of the Design Handbook Division of the SAE Fatigue Design and Evaluation Technical Committee, AE-10, Second Edition, Society of Automotive Engineers, Warrendale, PA.
- Scieszka and Dutkiewicz, 1991, "Testing Abrasive Wear in Mineral Comminution", The International J. of Mineral Processing, Vol. 32, pp. 81–110.

- Shigley, J. E., 1972, *Mechanical Engineering Design*, Second Edition, McGraw Hill, Inc., New York, p. 174.
- Shigley, J. E. and Mischke, C. R., 1989, *Mechanical Engineering Design*, Fifth Edition, McGraw Hill, Inc., New York, p. 259.
- Shigley, J. E. and Mischke, C. R., 2001, *Mechanical Engineering Design*, Sixth Edition, McGraw Hill, Inc., New York.
- Smith Fasteners, 2003, Socket Shoulder Screws Dimensions and Specifications, Smith Fastener Company, Bell, CA, URL <a href="http://www.smithfast.com/shoulderscrew.html">http://www.smithfast.com/shoulderscrew.html</a>.
- Sommer, C., Sommer, S. and Sommer, C., 2000, Wire EDM Handbook, Advance Publishing, Inc., Houston, TX, pp. 11-23.
- Titanium Industries, 2003, Data & Reference Manual, Titanium Industries, Inc., Montreal, QC.
- TRW, 1985, Optoelectronics Data Book, Optoelectronics Division, TRW Electronic Components Group, Carrollton, TX, pp. 244–245.
- Xu, Tan and Zhou, 1991, "Impact Wear Mechanisms of Medium Carbon Steel Under Various Dry and Wet Conditions", *The ASME J. of Wear of Materials*, pp. 33–40.

## APPENDIX A

## Engineering Drawings of the Lever Arm Assembly and its Components

As mentioned in chapter 7, after designing all the Lever arm assembly components, their engineering drawings were sent to a local manufacturer to be manufactured by wire EDM. This appendix contains engineering drawings of the Lever arm assembly and its components.

## A.1. Drawings of the Lever Arm Assembly and Components

The following table gives a summary of names, codes and figure numbers associated with the respective assembly/part.

Assembly/part name	Assembly/part code	Figure no.
General Lever Arm	CD02	A.1
Lever Arm	CD02/100	A.2
Lever Arm & Brass Bushing	CD02/110A-B	A.3-4
Follower	CD02/120	A.5
Follower Main Body	CD02/121	A.6
Follower Steel Roller	CD02/122	A.7
Coupling	CD02/200	A.8
Coupling Front Part	CD02/210	A.9
Coupling Side Bracket	CD02/220	A.10

Table A.1: Assembly/part names, codes, and figure numbers.

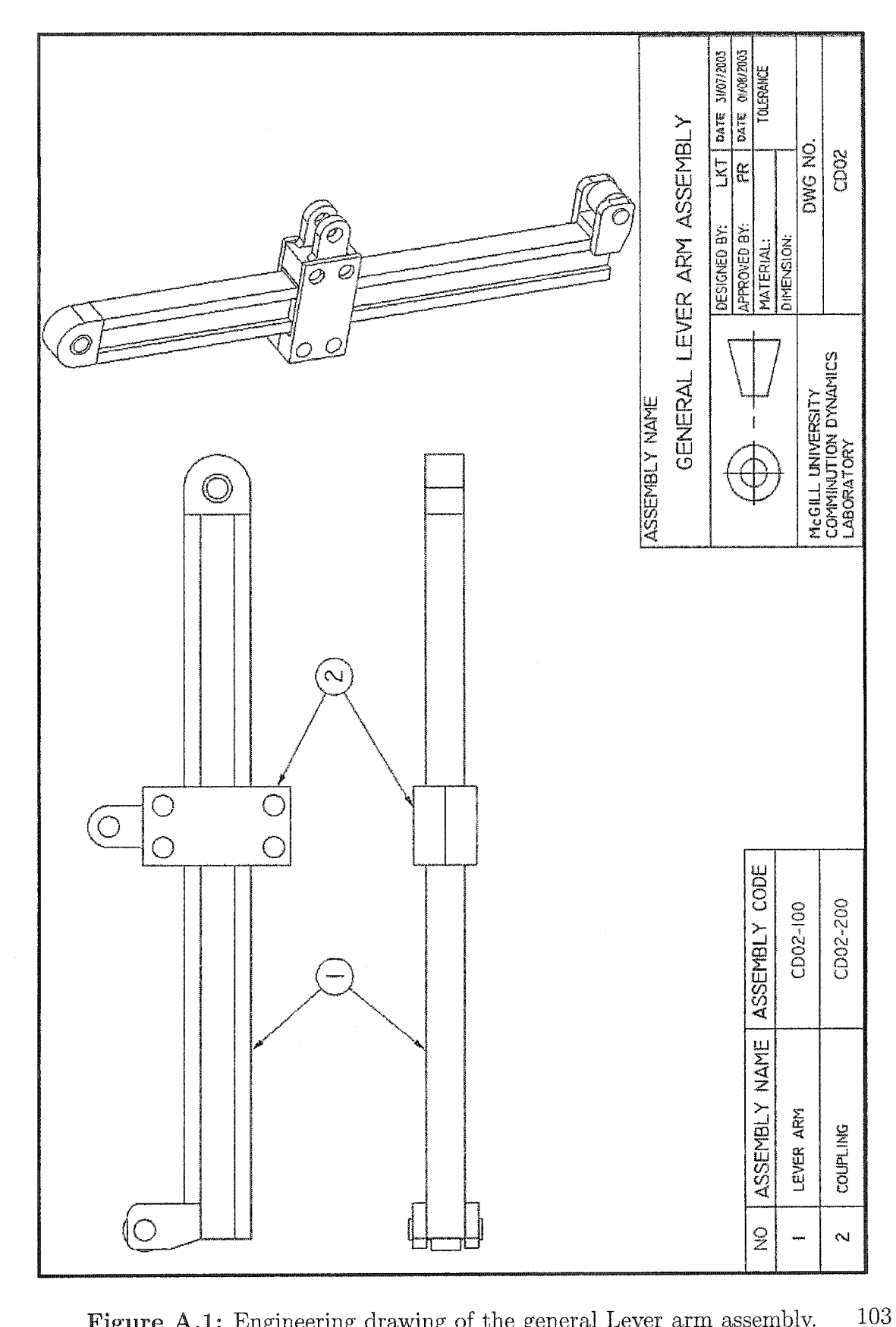


Figure A.1: Engineering drawing of the general Lever arm assembly.

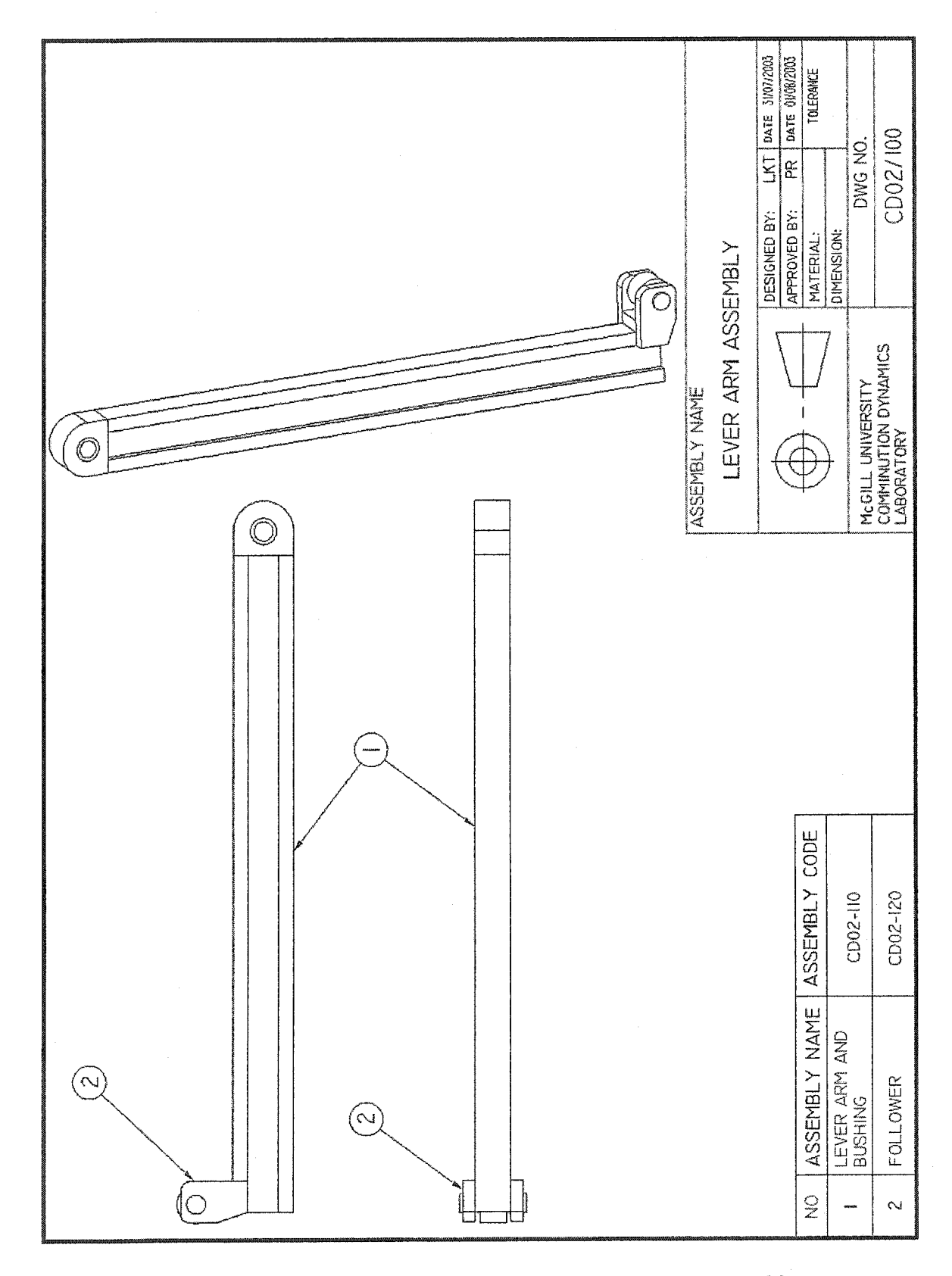


Figure A.2: Engineering drawing of the Lever arm assembly.

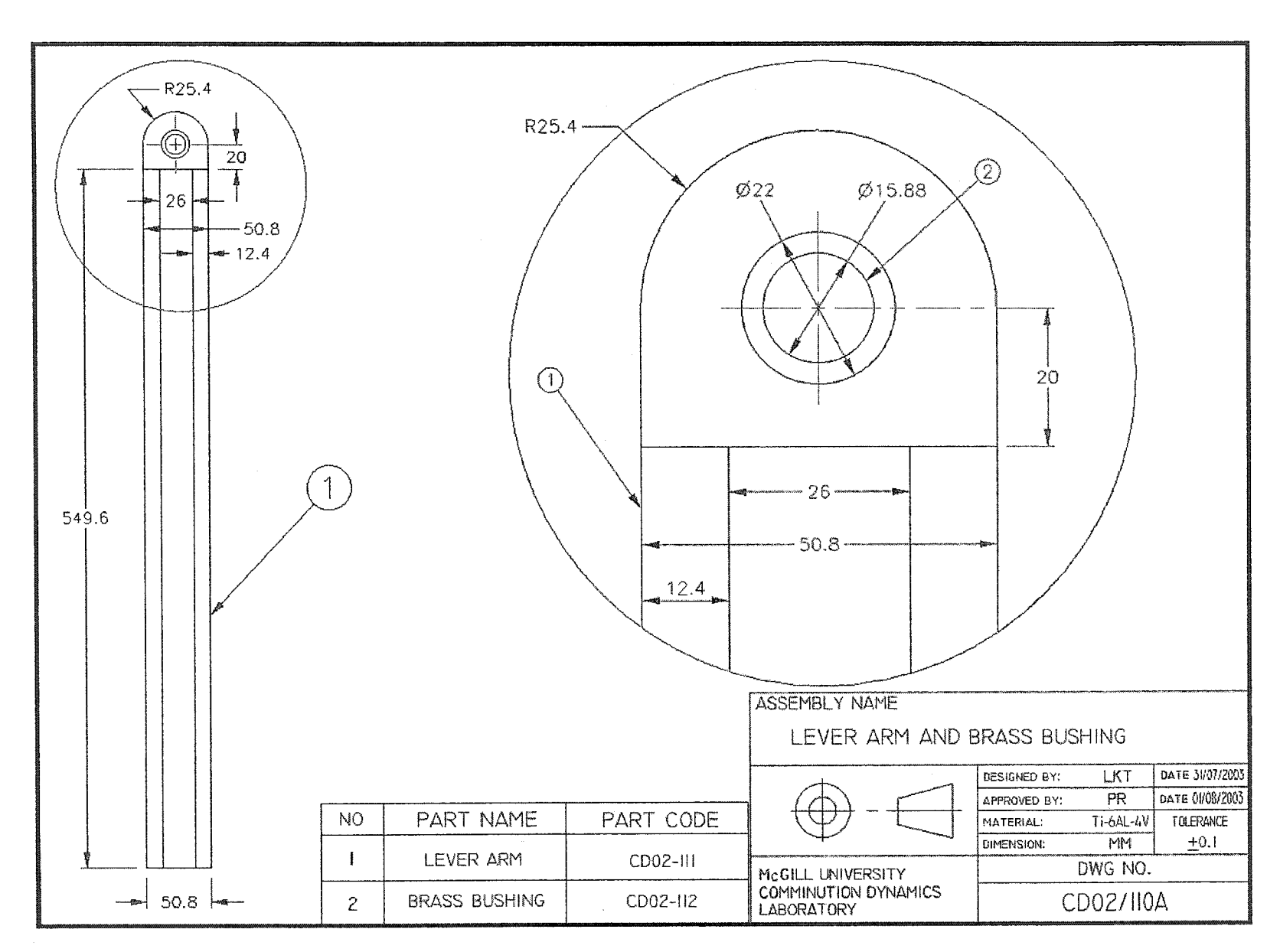


Figure A.3: Engineering drawing of Lever arm and brass bushing

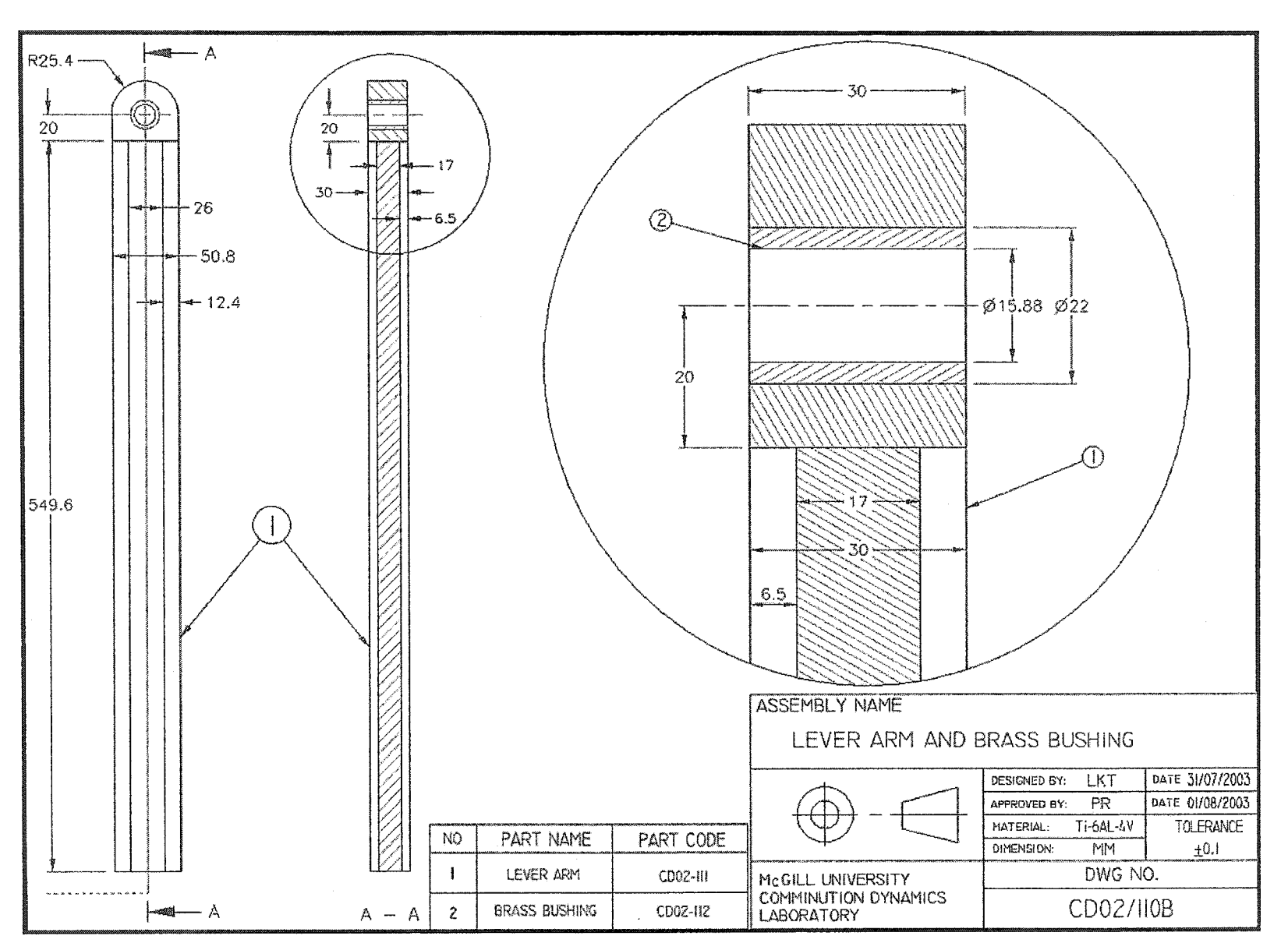


Figure A.4: Engineering drawing of Lever arm and brass bushing

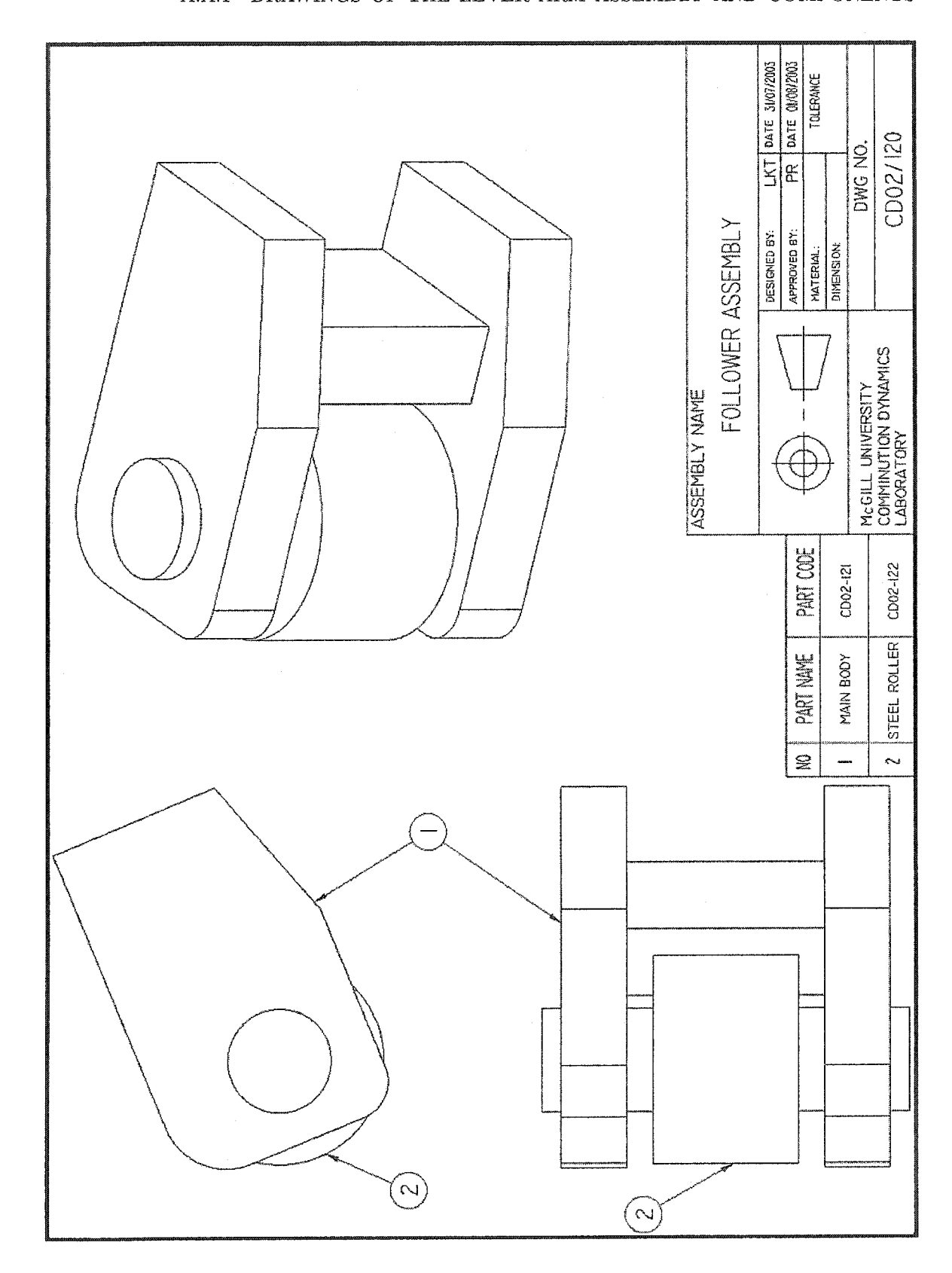


Figure A.5: Engineering drawing of the follower assembly.

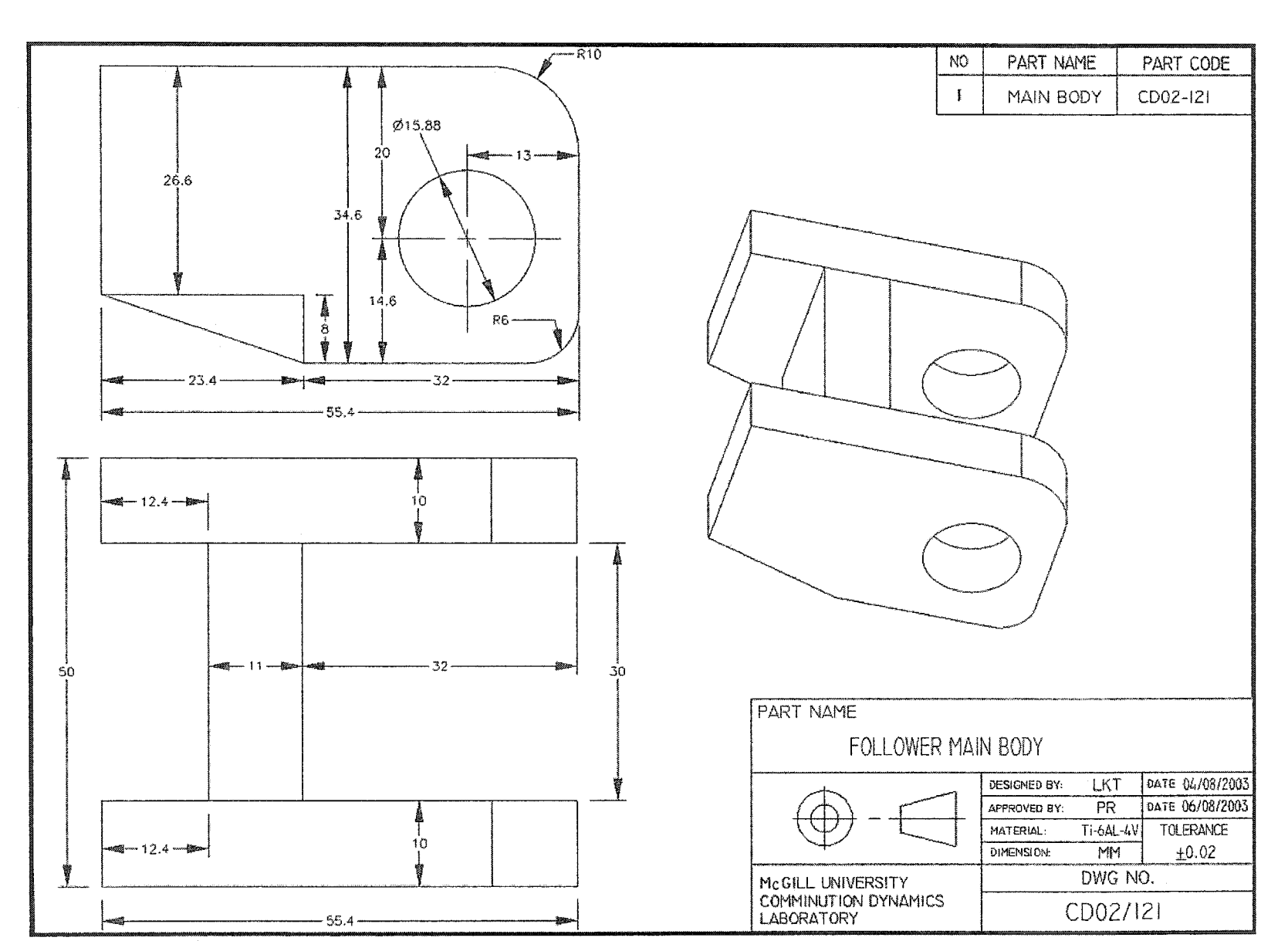


Figure A.6: Engineering drawing of the follower main body.

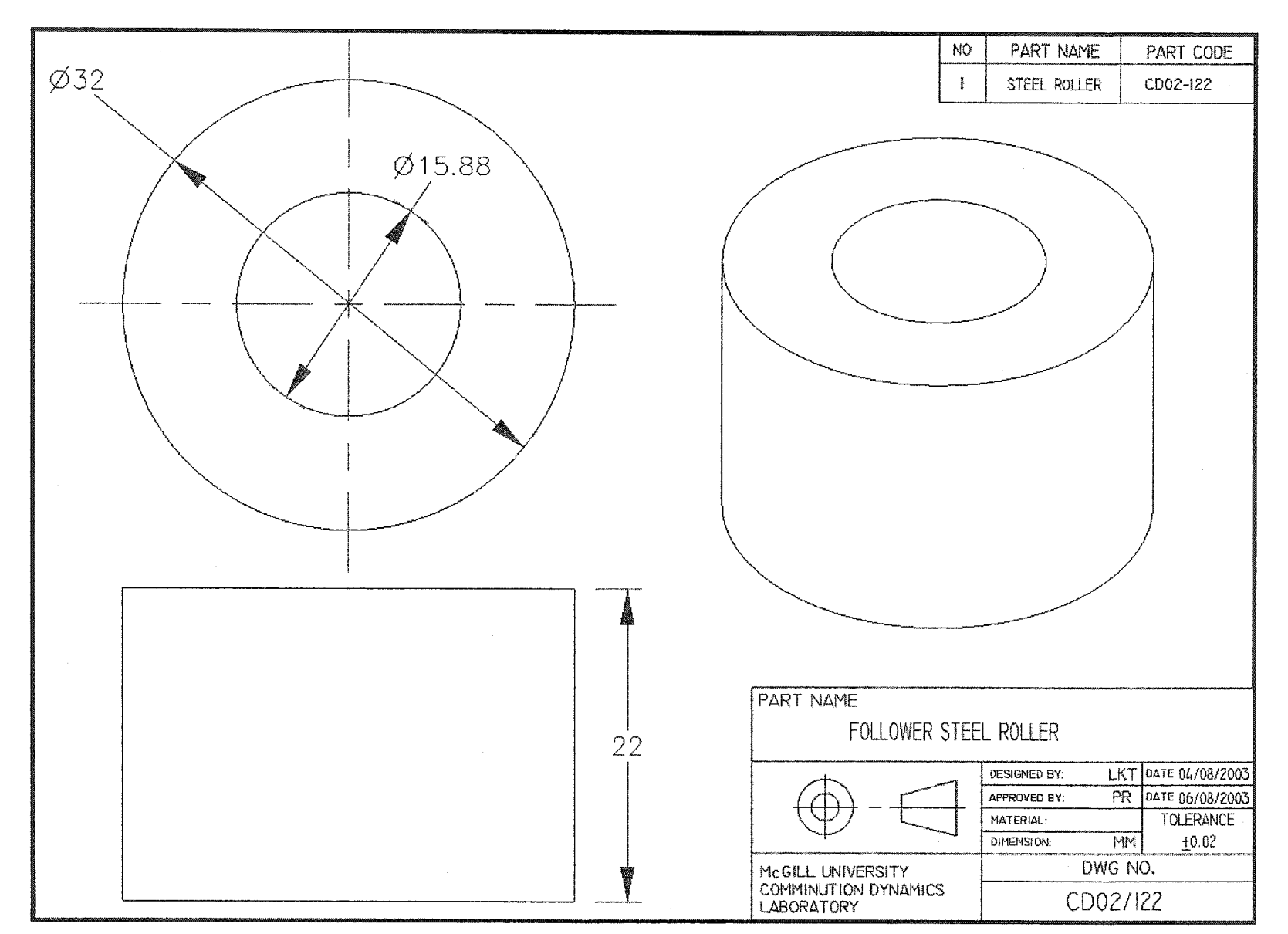


Figure A.7: Engineering drawing of the follower steel roller.

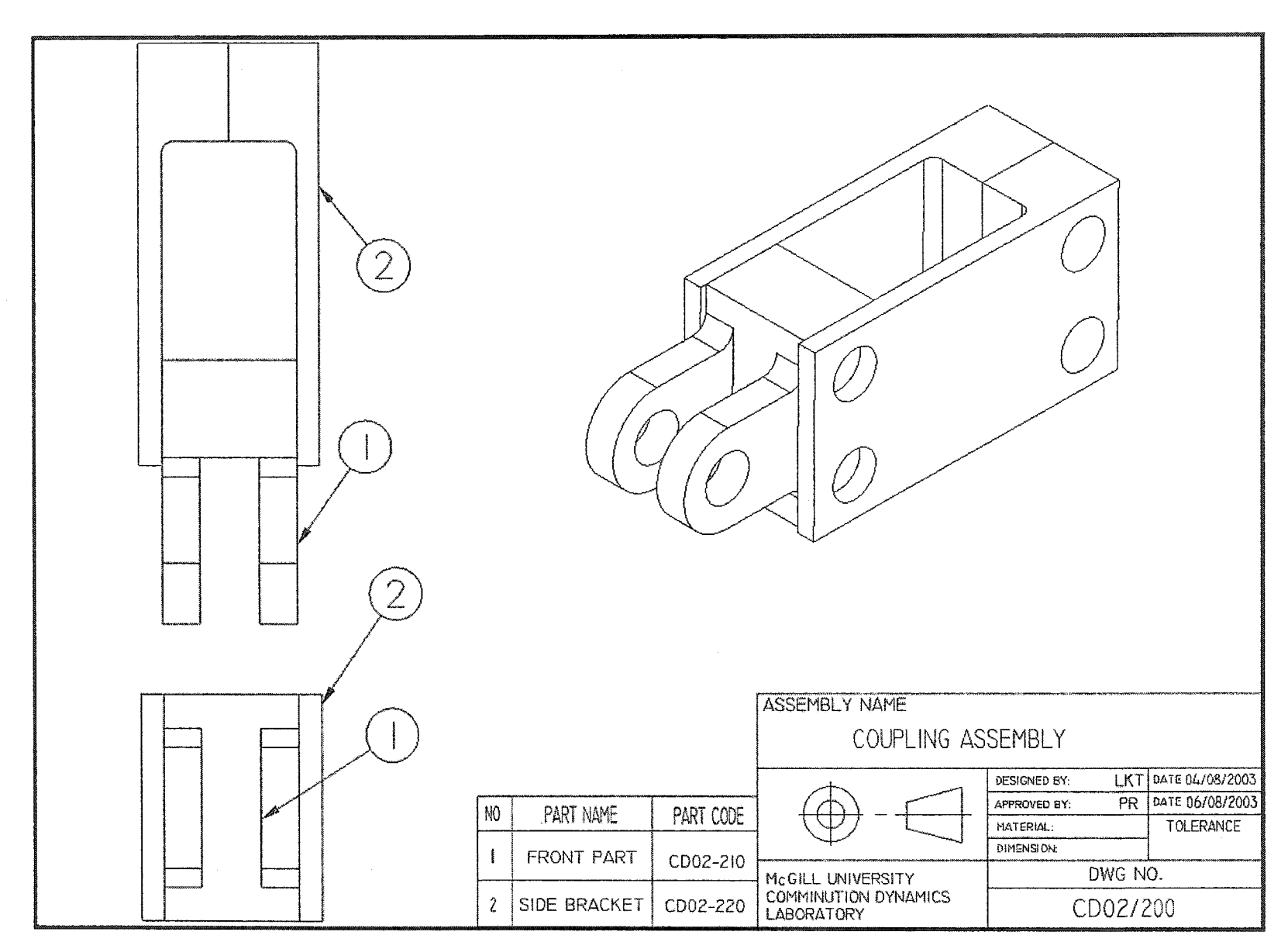


Figure A.8: Engineering drawing of the coupling assembly.

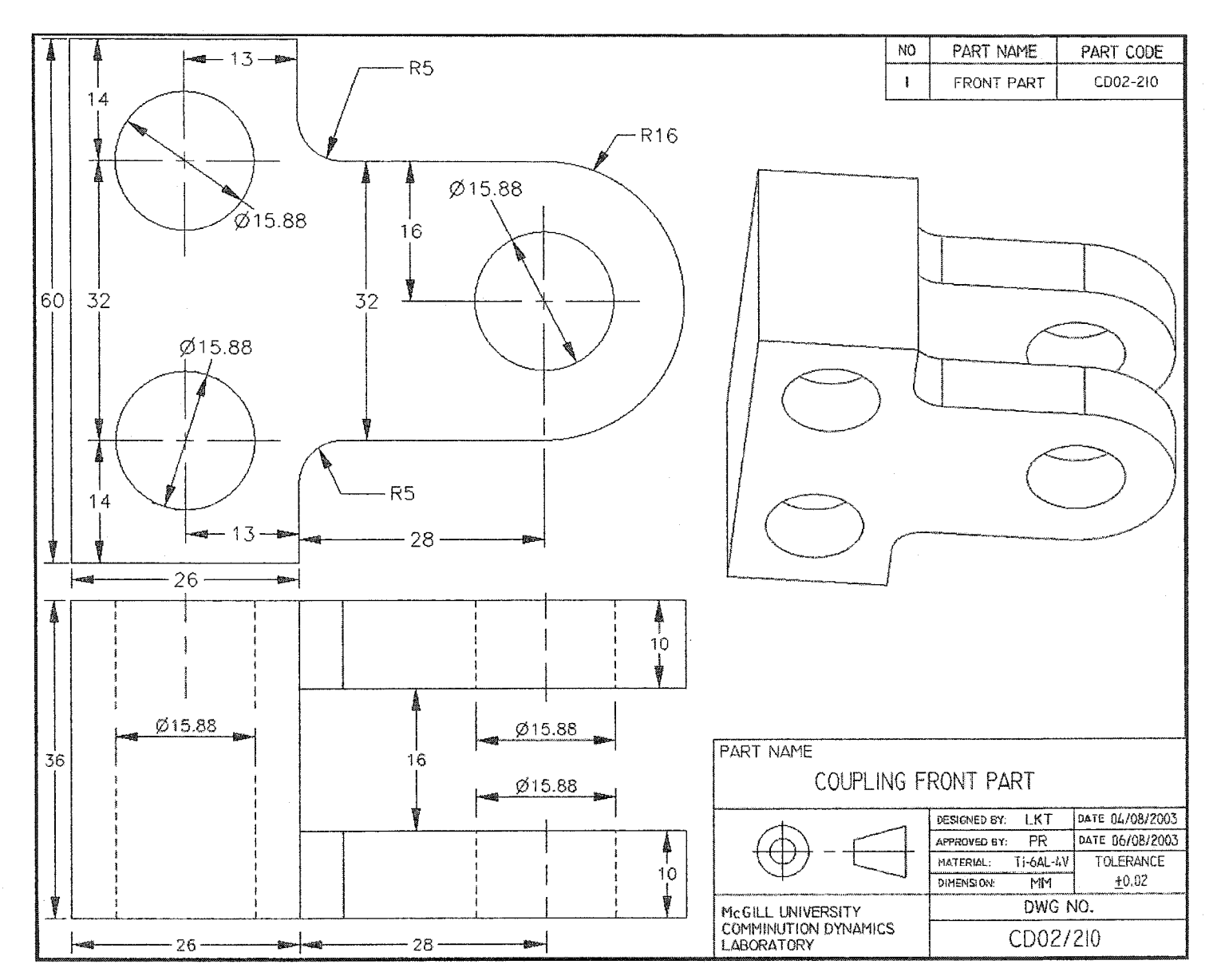


Figure A.9: Engineering drawing of the coupling front part.

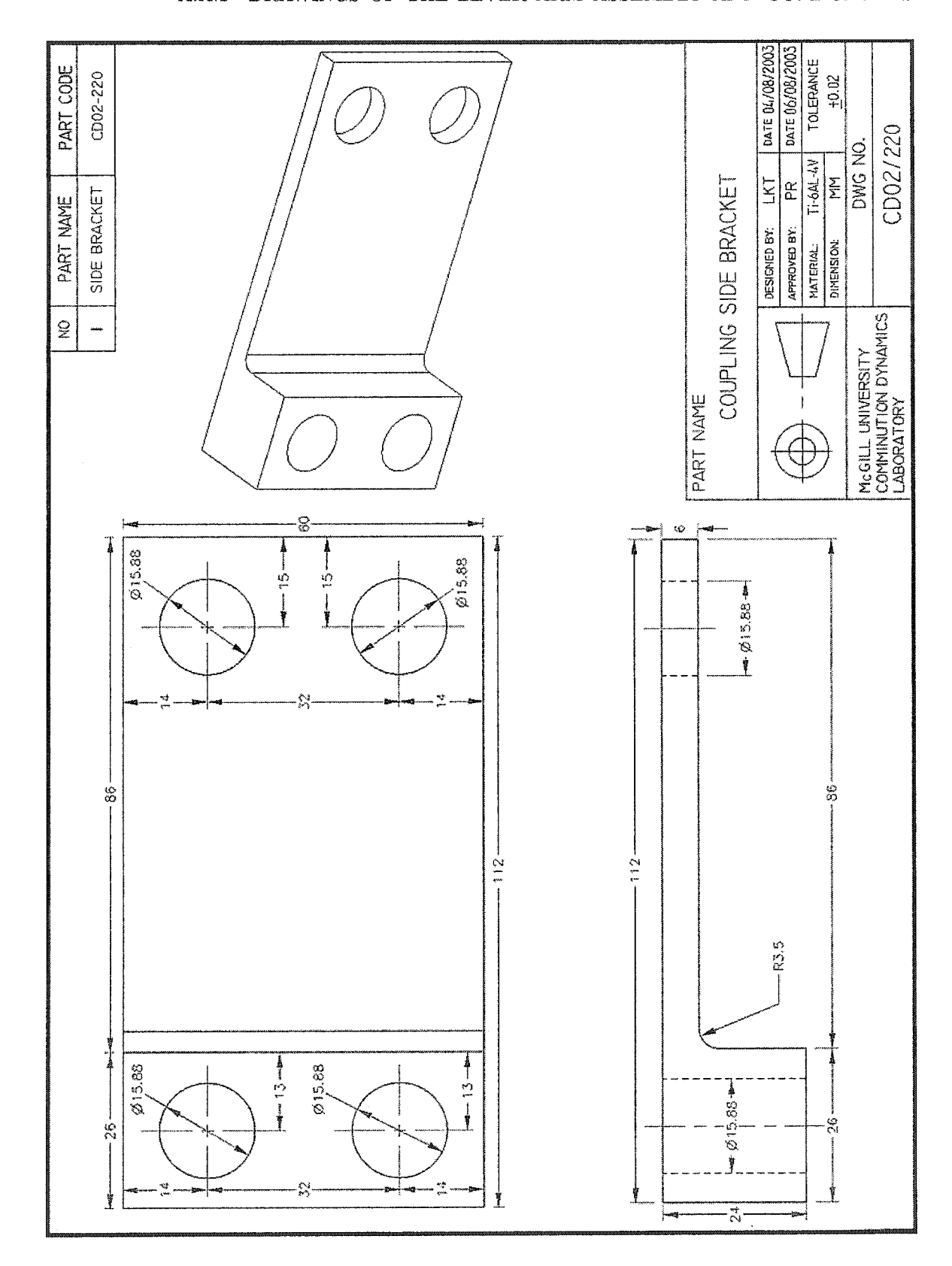


Figure A.10: Engineering drawing of the coupling side bracket.

## Document Log:

Manuscript Version 1 — October, 2003 Typeset by  $\mathcal{A}_{\mathcal{M}}\mathcal{S}$ -LATEX — 6 April 2004

LOKESH K. THAKUR

DEPARTMENT OF MECHANICAL ENGINEERING, McGILL UNIVERSITY, 817 SHERBROOKE STREET WEST, MONTRÉAL (QUÉBEC) H3A 2K6, CANADA, *Tel.* : (514) 398-6292

E-mail address: lokesh.thakur@mail.mcgill.ca

Typeset by  $\mathcal{A}_{\mathcal{M}}\mathcal{S}\text{-}\text{IAT}_{\mathcal{E}}X$